MRI-BASED CORRECTION FOR PET PHOTON ATTENUATION IN SIMULTANEOUS PET/MRI USING ULTRASHORT ECHO TIME METHODS


Meher Rohit Juttukonda



A dissertation submitted to the faculty at the University of North Carolina at Chapel Hill in partial fulfillment of the requirements for the degree of Doctor of Philosophy in the Department of Biomedical Engineering in the School of Medicine.




Chapel Hill
2015

Approved by:

Hongyu An

David S. Lalush

Paul A. Dayton

Weili Lin

Yueh  Z. Lee

**ABSTRACT**

Meher Juttukonda: MRI-based Correction for PET Photon Attenuation in Simultaneous
PET/MRI Using Ultrashort Echo Time Methods
(Under the direction of Hongyu An and David Lalush)


Positron emission tomography (PET) is a functional imaging modality that allows clinicians to visualize complex physiological processes such as metabolism, proliferation, perfusion, and receptor binding. Magnetic resonance imaging (MRI) is a versatile imaging modality that provides detailed anatomical images as well as functional information. Hybrid PET/MRI systems have been recently proposed as a means to combine the high-sensitivity functional information provided by PET with the high-resolution anatomical information provided by MRI. Furthermore, PET/MRI systems have the capability to provide complementary functional information acquired from both modalities. These systems have garnered significant clinical interest particularly in neurological imaging due to these capabilities.

A major drawback of PET/MRI systems is the lack of an accurate, clinically feasible MRI-based method for performing PET photon attenuation correction. The current vendor-provided methods lack accuracy, and more accurate methods proposed in literature are not clinically feasible due to long computation times. The inaccuracies of the vendor-provided methods result from misidentification of tissues, particularly bone, or the assumption of homogenous attenuation coefficients inside each tissue. Therefore, the goal of this work was

to develop an MR-based attenuation correction method that addresses both of these challenges in a clinically feasible framework.

To achieve this goal, we propose an ultrashort echo-time method that acquires all necessary data using one sequence and produces the necessary attenuation maps quickly. The proposed sequence utilizes a dual flip-angle, dual echo-time ultrashort echo time (UTE) acquisition to segment all tissues of interest to attenuation correction in the head and neck. Next, continuous-valued attenuation coefficients are assigned to all imaging voxels through a conversion from MR relaxation rate $R_1$. The capability of the method to generate accurate PET images was assessed by comparison to the gold standard CT-based method in a large number of subjects. The results show that the proposed method is significantly more accurate in the whole brain as well as in several smaller regions of interest when compared to the corresponding vendor-provided method. The proposed method has been fully automated and can be easily incorporated into the PET/MRI clinical work-flow.

To my wife, Lillian;

my father, Sudhakar; my mother, Geetha; and my brother, Virinchi

Last but not least, I would like to thank my family and friends for all of their support over the years. I am extremely thankful for my father Sudhakar and my mother Geetha who have made tremendous sacrifices in order to provide me with the best opportunities. Moreover, my father has been and continues to be the most important influence in my academic career. My brother Virinchi is my oldest friend and helped keep me sane over the past few years by engaging me in conversations about topics other than my research. Thanks also to my wife Lillian for her help on everything from proofreading papers and listening to my practice talks to her encouragement during the highs and lows of my research progress. I could not have done this without her support. My friend Michael Fagan, a graduate student in computer science at the University of Connecticut, was of great help during times when machines proved to be more of a hindrance than a help. I would also like to acknowledge my grandfather, Mallaiah Narala, who was an early and important influence on my academic career and ambitions. Finally, I would like to thank my family who reside all around the world, including my grandmothers Kusuma Juttukonda and Shakuntala Narala, for all of their well-wishes as I continue to pursue my academic ambitions.

# PREFACE

Most of the work presented henceforth was conducted in the Biomedical Research Imaging Center at the University of North Carolina at Chapel Hill. The clinical data referred to in Chapters 5-7 were collected either at Washington University in St. Louis or at University of North Carolina Hospitals using IRB-approved protocols. The research data referred to in Chapter 6 were collected at the Biomedical Research Imaging Center using an IRB-approved protocol. The processing of all data was conducted entirely at the Biomedical Research Imaging Center at the University of North Carolina at Chapel Hill.

The method discussed in detail in Section 4.4 has been published [Chen Y, Juttukonda M, Su Y, Benzinger T, Rubin BG, Lee YZ, Lin W, Shen D, Lalush D, An H. Probabilistic Air Segmentation and Sparse Regression Estimated Pseudo CT for PET/MR Attenuation Correction. Radiology]. Chen Y was responsible for major areas of concept formation, data analysis, and manuscript composition. I was responsible for portions of the data analysis and manuscript composition

A version of Chapter 5 has been published [Juttukonda MR, Mersereau BG, Chen Y, Su Y, Rubin BG, Benzinger TL, Lalush DS, An H. MR-based attenuation correction for PET/MRI neurological studies with continuous-valued attenuation coefficients for bone through a conversion from R2* to CT-Hounsfield units. Neuroimage 112: 160-168, 2015]. I was responsible for major areas of concept formation, data analysis, and manuscript composition. Mersereau BG was involved in data processing and in manuscript editing.

**TABLE OF CONTENTS**

# LIST OF TABLES

# LIST OF FIGURES

# LIST OF ABBREVIATIONS

AC       Attenuation correction

ADC       Apparent diffusion coefficient

bSSFP       Balanced steady-state free precession

CAR-RiDR       Continuous-valued attenuation coefficients from $R_2^*$-$R_2^*$ and iUTE-based segmentation with Dixon-based refinement

CSF       Cerebrospinal fluid

CT       Computed tomography

CTAC       Computed tomography-based attenuation correction

DCE       Dynamic contrast-enhanced

DUFA-UTE       Dual flip angle ultrashort echo time

DUTE       Dual-echo ultrashort echo time

DWI       Diffusion-weighted imaging

EEG       Electroencephalogram

EM       Expectation maximization

FA       Flip angle

FDG       Fluorodeoxyglucose

FOV       Field-of-view

GM       Gray matter

GRE       Gradient recalled echo

HU       Hounsfield units

IRB       Institutional review board

IR       Inversion recovery

| | |
|---|---|
| iUTE | inverse ultrashort echo time |
| IV | Intravenous |
| LAC | Linear attenuation coefficient |
| LOR | Line of response |
| MAPE | Mean absolute percent-error |
| MPE | Mean percent-error |
| MPRAGE | Magnetization-prepared rapid gradient-echo |
| MRAC | Magnetic resonance imaging-based attenuation correction |
| MRF | Markov random field |
| MRI | Magnetic resonance imaging |
| MRS | Magnetic resonance spectroscopy |
| OSEM | Ordered subset expectation maximization |
| PASSR | Probabilistic air segmentation and sparse regression |
| PET | Positron emission tomography |
| RF | Radiofrequency |
| ROI | Region of interest |
| SD | Standard deviation |
| SNR | Signal-to-noise ratio |
| SPECT | Single photon emission computed tomography |
| SUV | Standardized uptake value |
| T1-MR | $T_1$-weighted magnetic resonance |
| TESLA | $T_1$-enhanced segmentation and selection of linear attenuation coefficients |
| UTE | Ultrashort echo time |

| | |
|---|---|
| vDixon | Vendor-provided Dixon method |
| VFA | Variable flip angle |
| vUTE | Vendor-provided ultrashort echo time method |
| WASPI | Water- and fat-suppressed proton projection imaging |
| WIP | Work in progress |
| WM | White matter |
| ZTE | Zero echo time |

# LIST OF SYMBOLS

| | |
|---|---|
| ‖ ‖ | Two-norm |
| $\alpha$ | atlas patch weighting |
| $\beta$ | Positron |
| $B_o$ | Static magnetic field |
| $B_1$ | Radiofrequency magnetic field |
| e | Euler's number |
| $^{18}F$ | Fluorine-18 |
| $\Upsilon$ | Gyromagnetic ratio |
| $G_{PE}$ | Phase-encoding gradient |
| $G_{RO}$ | Read-out gradient |
| $G_x$ | Gradient in x-direction |
| $G_y$ | Gradient in y-direction |
| $G_z$ | Gradient in z-direction |
| $^1H$ | Hydrogen nucleus |
| J | Angular momentum |
| Kr | Radial lines |
| $\lambda_1$ | Sparse regression term |
| $\lambda_2$ | Ridge regression term |
| L | Thickness |
| $\mu$ | Linear attenuation coefficient |
| $\boldsymbol{\mu}$ | Magnetic moment |

| | |
|---|---|
| MBq | Megabecquerel |
| MHz | Megahertz |
| $\mathbf{M}$ | Magnetization vector |
| $\mathbf{M_0}$ | Equilibrium magnetization vector |
| $\mathbf{M_{xy}}$ | Equilibrium magnetization vector |
| $\mathbf{M_z}$ | Longitudinal magnetization vector |
| kev | Kilo electron volts |
| kVp | Peak kilo voltage |
| n | Neutron |
| v | Neutrino |
| p | Proton |
| $\rho$ | Proton density |
| $P_t$ | Template patch |
| $P_{MR}$ | Patient patch |
| $r^2$ | Coefficient of determination |
| $R_1$ | Longitudinal relaxation rate |
| $R_2$ | Irreversible transverse relaxation rate |
| $R_2'$ | Reversible transverse relaxation rate |
| $R_2^*$ | Transverse relaxation rate |
| t | Time |
| T | Tesla |
| $T_1$ | Longitudinal relaxation time |
| $T_2$ | Irreversible transverse relaxation time |

| | |
|---|---|
| $T_2$' | Reversible transverse relaxation time |
| $T_2$' | Irreversible transverse relaxation time |
| TE | Echo time |
| TI | Inversion time |
| TR | Repetition time |
| $\omega_0$ | Larmor frequency |

**CHAPTER 1: INTRODUCTION**

**1.1 Multimodality Imaging**

The fundamental goal of medical imaging is to provide physicians with diagnostically relevant images of the inside of a human body without the need for exploratory surgery. Medical imaging systems are often classified either as anatomical modalities, which provide structural information, or as functional modalities, which are used to study physiological functions. Since they serve different purposes, anatomical modalities, such as magnetic resonance imaging (MRI) and x-ray computed tomography (CT), have historically been separated from functional modalities, such as positron emission tomography (PET). This separation is evident in their placement in different clinical divisions (radiology and nuclear medicine), but the advantages of integrating anatomical and functional imaging have been recognized by clinicians for many decades. The primary benefit of combining these two types of modalities is the ability to use anatomical images to localize any regions of functional abnormalities. To this end, there are two general approaches which one can use to assimilate information from functional and anatomical images: software and hardware *(1)*.

**1.2 Software-based Image Fusion**

The first attempts at combining anatomical and functional images were made in the late 1980s and produced sophisticated image fusion software with the capability of aligning functional images with separately-acquired anatomical images. These algorithms go beyond simple image overlays or the use of external stereotactic frames either by identifying common landmarks that can be used to align the images or by optimizing a parameter based on the

intensities in the images. For either approach, the complexity of the transformation needed depends on the possible degrees of freedom between the two images. For anatomical regions such as the brain where a change in size or shape between scans is not anticipated, simple rigid body transformations are sufficient. More complicated nonlinear registration techniques are needed when there are no constraints on the possible deformations. One example of this is in the abdomen during non-rigid respiratory motion. Assessments of these methods have shown that a local registration accuracy of approximately 2 mm can be achieved for the brain while the performance is markedly worse for other regions of the body such as the lung and the pelvis, where the local registration accuracy can be as poor as 5-8 mm. Therefore, software-based solutions are limited to cases where image registration is trivial *(1)*.

**1.3 Hybrid PET/CT**

In contrast, hardware approaches provide a simple and convenient approach to combining images by integrating instrumentation from functional and anatomical modalities and acquiring both sets of images in a common reference frame. The first of these hardware approaches to be developed was the hybrid PET/CT scanner which acquires co-registered PET and CT images in a single study *(1)*. Hybrid PET/CT systems were commercially introduced in 2001 and gained widespread acceptance among clinicians shortly thereafter, particularly in oncology. PET is a functional imaging modality that allows clinicians to visualize complex physiological processes such as metabolism, proliferation, perfusion, and receptor binding *(2)*. CT is an anatomical imaging modality that derives its contrast from the absorption or scattering of the transmitted x-ray photons by tissues in the body, also known as photon attenuation. Therefore, in addition to providing anatomical images to serve as a context for the functional images (Figure 1.1) provided by PET, CT images also provide a straightforward means for

correcting for the phenomenon of gamma photon attenuation in PET. Details about the phenomenon of photon attenuation as well as about CT-based attenuation correction will be presented in Chapter 2.
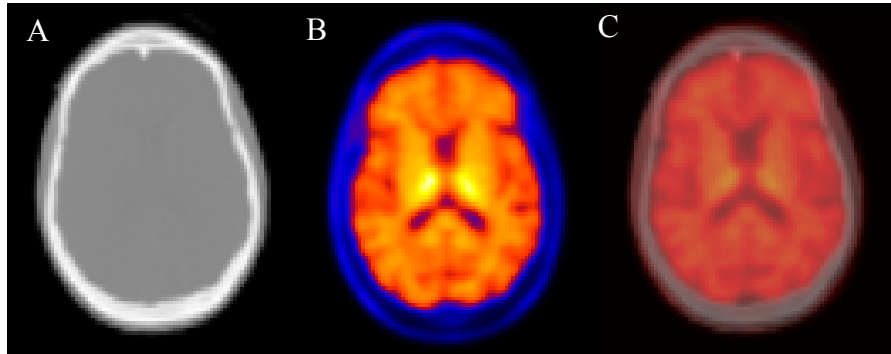


Figure 1.1: CT images (A) provide anatomical context for the functional images from PET (B) as shown in the PET/CT fusion image (C).

Hybrid PET/CT systems are not without considerable drawbacks. First, CT imaging employs the transmission of ionizing radiation in the form of x-rays through a patient's body. Although the doses associated with CT scans are low enough not to have any deterministic effects, stochastic effects that result in elevated risk for developing cancer have been demonstrated *(3)*. Second, CT is limited in the imaging capabilities it can offer. For example, simultaneous PET and CT acquisitions are not a realistic possibility nor are they desirable because simultaneous acquisition would not provide much additional information compared to sequential acquisition. Third, the contrast in CT imaging proves sufficient for some applications, but is particularly lacking for most soft tissue applications. Specifically, the CT images cannot be used to localize PET signals to gray matter or white matter regions of the brain. Therefore, while the anatomical context and the ability to easily perform attenuation correction are vast improvements over stand-alone PET systems, PET/CT systems leave much to be desired.

**1.4 Hybrid PET/MRI**

Recently, hybrid PET/MRI systems have been developed to fill the voids left by PET/CT scanners. While make-shift systems with MRI-compatible PET inserts are also in existence, truly hybrid PET/MRI systems currently exist in two forms: sequential (Ingenuity TF, Philips, Best, Netherlands) and simultaneous (SIGNA, General Electric, Buckinghamshire, United Kingdom; Biograph mMR, Siemens, Erlangen, Germany). While sequential systems address the concerns of ionizing radiation and lack of soft tissue contrast expressed with PET/CT, simultaneous PET/MRI systems are generally preferable due to the capability of acquiring information from both modalities simultaneously. References made to PET/MRI systems hereafter in this dissertation refer to the Biograph mMR simultaneous PET/MRI system manufactured by Siemens Healthcare (Erlangen, Germany) *(4)*. PET/MRI images presented in this work were acquired using a Biograph mMR system either at the Biomedical Research Imaging Center at the University of North Carolina at Chapel Hill or the Mallinckrodt Institute of Radiology at Washington University in St. Louis.

Developing a truly integrated system around the constraints imposed by the MRI component's strong magnetic field proved to be a difficult task. MRI instrumentation by necessity contains no ferromagnetic metal components that could interfere with imaging capabilities. However, existing PET detector technology is highly sensitive to the presence of magnetic fields. Therefore, novel PET detector technology which could operate well under the rigorous conditions imposed by the strong magnetic field utilized in MRI was developed. The PET detectors were designed to be able to function in between two MRI components of the system, as shown in Figure 1.2. These innovations were highly expensive, raising doubts about whether the benefits provided by PET/MRI systems justify the costs. Furthermore,

simultaneous PET/MRI systems have been referred to as "a solution looking for a problem" because they are a product of a technological advance rather than a solution for a pressing clinical need *(5)*.
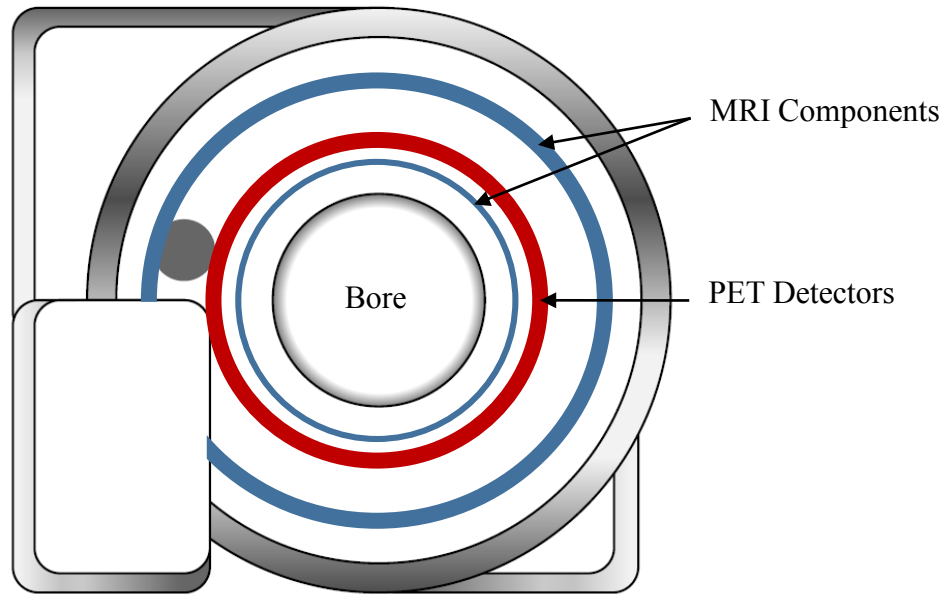


Figure 1.2: Schematic of the Siemens Biograph mMR simultaneous PET/MRI system.

The current consensus to the question of whether PET/MRI systems are worth the markedly increased cost over PET/CT systems seems to be "perhaps". However, simultaneous PET/MRI systems are gaining support from researchers and clinicians in various fields, especially for applications where anatomical images with excellent soft tissue contrast are needed (Figure 1.3); MRI can also be used to gather physiological information about oxygen metabolism, the structure of nerve and muscle fibers, and a plethora of other physiological parameters *(6)*, serving as an excellent complement to PET imaging.

In addition to potential clinical applications for PET/MRI systems that have already been identified in neurology *(7)*, cardiology *(8)*, and oncology *(9)*, there are also many technical advantages to utilizing PET/MRI systems in lieu of existing hybrid PET/computed tomography (CT) systems. As previously mentioned, there is no additional ionizing radiation incurred on

patients in order to obtain the anatomical information used to localize PET signals. In addition, the anatomical information provided by MRI is far superior to that of CT, especially in the realm of soft tissue contrast. Finally, MRI can be used to address existing technical issues in PET including motion correction *(10)* and partial volume correction *(11)* that could not be addressed using PET/CT systems.
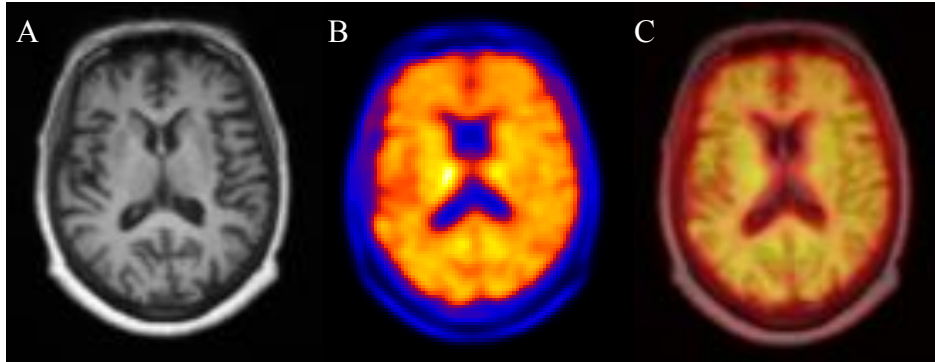


Figure 1.3: MR images (A) provide excellent soft tissue contrast for improved localization of PET images (B) as shown in the PET/MR fusion image (C).

Despite the many advantages, there is a major technical drawback with PET/MRI systems: PET photon attenuation correction. Attenuation correction (Chapter 2) is straight-forward in PET/CT due to the ease of utilizing the CT component of the system to derive the necessary information; there is no analogous way to gather this information in PET/MRI systems due to differences in the source of signal (Chapter 3). The focus of this dissertation is on the development of potential approaches to perform MRI-based correction for PET photon attenuation. Chapter 2 introduces the fundamentals of PET imaging and the physics of photon attenuation, while Chapter 3 addresses the basics of MRI as well as its limitations in providing the information necessary for PET attenuation correction. Chapter 4 explores existing methods along with their strengths and pitfalls with particular emphasis on the current methods utilized by the manufacturer. Chapter 5 presents an initial solution to the problem of MR-based attenuation correction, while Chapter 6 outlines a more refined solution. Chapter 7 discusses

certain clinical applications of PET/MRI systems and the relevance of the final attenuation correction method to those applications. Chapter 8 serves as a conclusion for this dissertation by outlining the contributions made by this dissertation to the field and by identifying areas where further work is needed.

# REFERENCES

1. Townsend DW. Multimodality imaging of structure and function. *Phys Med Biol*. 2008;53:R1-R39.

2. Bailey D, Townsend D, Valk P, Maisey M, eds. *Positron Emission Tomography: Basic Sciences.* London: Springer-Verlag London; 2005.

3. U.S. Food and Drug Administration. What are the risks of radiation from CT? 2015. Available from: http://www.fda.gov/RadiationEmittingProducts/RadiationEmittingProducts andProcedures/MedicalImaging/MedicalX-Rays/ucm115329.htm. Accessed June 10, 2015.

4. Delso G, Furst S, Jakoby B, et al. Performance measurements of the siemens mMR integrated whole-body PET/MR scanner. *J Nucl Med*. 2011;52:1914-1922.

5. Yankeelov TE, Peterson TE, Abramson RG, et al. Simultaneous PET-MRI in oncology: A solution looking for a problem? *Magn Reson Imaging*. 2012;30:1342-1356.

6. Haacke E, Brown R, Thompson M, Venkatesan R. *Magnetic Resonance Imaging: Physical Principles and Sequence Design.* 1st ed. New York: Wiley-Liss; 1999.

7. Barthel H, Schroeter ML, Hoffmann KT, Sabri O. PET/MR in dementia and other neurodegenerative diseases. *Semin Nucl Med*. 2015;45:224-233.

8. Rischpler C, Nekolla SG, Kunze KP, Schwaiger M. PET/MRI of the heart. *Semin Nucl Med*. 2015;45:234-247.

9. Bagade S, Fowler KJ, Schwarz JK, Grigsby PW, Dehdashti F. PET/MRI evaluation of gynecologic malignancies and prostate cancer. *Semin Nucl Med*. 2015;45:293-303.

10. Catana C. Motion correction options in PET/MRI. *Semin Nucl Med*. 2015;45:212-223.

11. Yan J, Lim JC, Townsend DW. MRI-guided brain PET image filtering and partial volume correction. *Phys Med Biol*. 2015;60:961-976.

# CHAPTER 2: PHOTON ATTENUATION

## 2.1 Positron Emission Tomography

Positron emission tomography (PET) is a molecular imaging modality that allows clinicians to visualize complex physiological processes such as metabolism, proliferation, perfusion, and receptor binding. Due to this capability, PET has had a tremendous impact in a number of fields including cardiology, neurology, psychiatry, and, most significantly, in oncology where PET is routinely used for everything from the diagnosis of malignancies to assessing treatment response of anti-cancer therapies *(1)*.

The contrast in PET imaging is typically introduced through intravenous (IV) injection of a molecular probe known as a radiotracer into the patient. These radiotracers are formed by
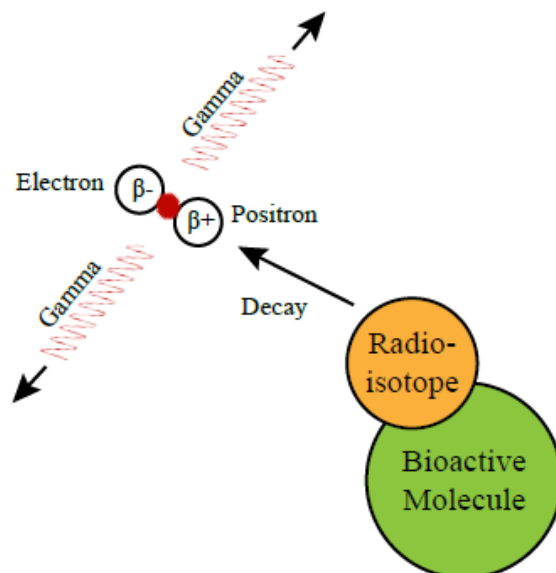


**Figure 2.1**: PET radiotracers consist of a bioactive molecule tagged with a radioisotope which decays by emitting a positron. The interaction of the positron with a surrounding electron produces two gamma photons that are detected in PET.

chemically combining the bioactive molecule of interest with a positron-emitting radioisotope. As the radiotracer travels through the patient's body and reaches the tissue or location of interest, secondary detection of radioisotope decay (Figure 2.1) allows for the visualization of the radiotracer distribution throughout the body.

Radioisotopes undergo spontaneous radioactive decay and is characterized by the half-life, which represents the time it takes for half of the radioactive material present to decay, of that isotope. Half-lives for radioisotopes of interest in PET range from 1.25 minutes ($^{82}$Rb – cardiac perfusion) to 100 hours ($^{124}$I – thyroid imaging). The particular decay pathway that a radioisotope follows is determined by the cause for instability in the underlying atomic nucleus. The nuclei of PET radioisotopes are proton-rich, i.e. the number of protons is too high for the nuclei to be stable. These isotopes undergo decay by eliminating a proton from the nucleus in order to rectify this imbalance. As shown in Equation 1, this correction most often occurs through the transformation of a proton (p) to a neutron (n), releasing a positron (β) and neutrino (ν) in the process *(1)*.

$$^{1}_{1}p^{+} \rightarrow \, ^{1}_{0}n + \, ^{0}_{1}\beta + \nu \qquad\qquad (2.1)$$

While neutrinos pass through body tissue without any interactions, each positron travels a short distance from its origin through the surrounding tissue, gradually dissipating its kinetic energy as a result of collisions and scattering with tissue electrons and nuclei. This distance, known as the positron range, depends on the initial energy of the positron at release and is approximately 1-2 mm for positrons resulting from the decay of $^{18}$F atoms. When its kinetic energy is nearly depleted, a positron undergoes an annihilation event with the next electron it encounters. This annihilation event results in the production of radiation in the form of two characteristic gamma photons of 511 keV energy. Conservation of momentum dictates

that these photons are emitted in anti-parallel directions, but the slightly non-zero momentum

possessed by the positron just prior to the annihilation event results in angles that are slightly

less than 180° *(1)*.

## 2.2 Image Acquisition

PET Detector Ring
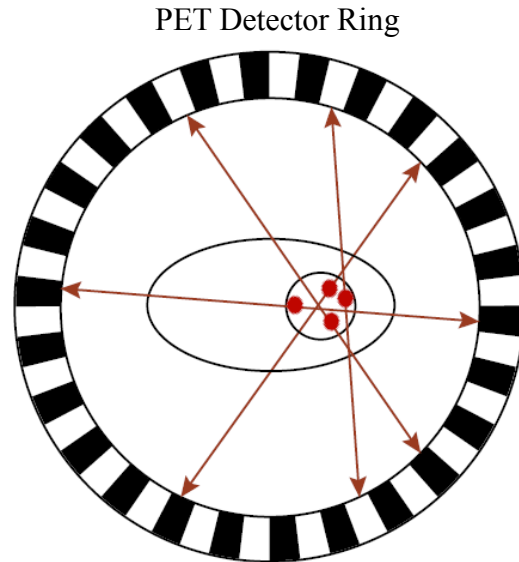


Figure 2.2: The detection of each pair of annihilation photons produces a line
of response (red arrows). A particular line of response indicates that the
underlying annihilation event (red circles) occured somewhere along that line.

Each pair of photons from an annihilation event travels through the patient's body and

reaches the surrounding PET detector ring at approximately the same time, forming what is

known as a line-of-response (LOR). An LOR indicates a linear path along which the

annihilation event that produced the associated photons occurred (Figure 2.2). Due to

differences in the distances traveled by each photon in a pair, it is expected that the lag time

between the first photons reaching a detector and the second photon could be as long as $3-4$

ns. Therefore, the window of time allotted for an LOR to form must be at least as wide as a

few nanoseconds. The collection of LORs produced over the course of the PET study is

organized in the form of a sinogram which is then reconstructed into an image corresponding

to the distribution of the radiotracer in the patient *(1)*.

**2.3 Image Formation**

Once the raw PET data is acquired, it can be reconstructed into a PET image using an analytical approach (*filtered back-projection*) or an iterative approach (*iterative reconstruction*). Iterative methods are preferable to analytical methods due to the improved handling of noise and to the more realistic model of the system utilized. There are five basic components to iterative reconstruction methods. The first component is a *model for the image* to be reconstructed. This is simply the discretization of the image into a certain number of voxels, or volume elements. The second component is a *model of the imaging system* that contains probabilities that emissions of photons originating at a given voxel are detected in a particular projection through that voxel. The third component is a *model of the imaging data*. Since the formation of each LOR is a discrete process, a Poisson model is the most appropriate choice. The fourth component is the *governing principle* of the method. This is the component that defines what a "best" image is for a given set of PET data and is often expressed as a mathematical cost function. In PET, the most common principle is the maximum likelihood (ML) approach. The fifth component is the *algorithm* utilized to optimize the cost function. The reconstruction algorithm employed by the manufacturer in the PET/MRI system is a variant of expectation maximization (EM) algorithms called the ordered subset expectation maximization (OSEM) algorithm *(2)*.

**2.4 Photon Attenuation**

In an ideal world, all gamma photons resulting from the annihilation events would be correctly accounted for by the PET detector system, allowing the reconstruction algorithm to form a PET image that perfectly reflects the distribution of the radiotracer. In reality, there are certain physical processes that prevent a percentage of the annihilation photons from reaching

the detectors, causing a loss of signal that degrades the accuracy of the PET reconstructions (Figure 2.3). These processes are collectively known as photon attenuation. Analytical simulations (Figure 2.4) have shown that, if left uncorrected, photon attenuation can result in errors of approximately 80% or higher in certain regions in the PET field-of-view. At PET photon energy levels, there are two mechanisms through which photons are attenuated: photoelectric effect (low probability) and Compton scattering (high probability) *(1)*.

PET Detector Ring
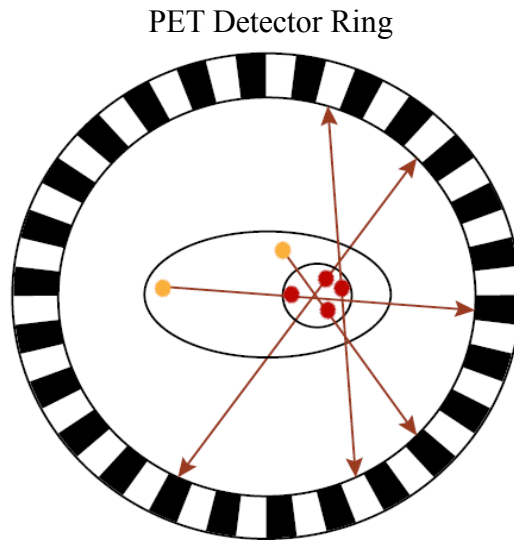


Figure 2.3: Photon attenuation (yellow) occurs as a result of interactions between annihilation photons and electrons in the surrounding tissue. This results in a loss of signal that degrades the accuracy of the reconstructed PET image.

The *photoelectric effect* describes the interaction between an annihilation photon and orbital electrons of atoms in the surrounding tissue. Through this interaction, the photon transfers all of its energy to the electron, ejecting the electron from orbit. In this case, the annihilation photon is eliminated and the underlying annihilation event is completely undetected. The photoelectric effect dominates at photon energies of approximately 100 keV and thus composes a very small percentage of the attenuation events at PET energy (511 keV). The primary mode of photon attenuation in PET is through *Compton scattering* in which an annihilation photon interacts with a loosely bound electron in a surrounding atom. The result

of this interaction is a deflection of the photon's path, along with a corresponding drop in the

photon's kinetic energy *(1)*.

PET Signal

Corrected      400      Uncorrected



0
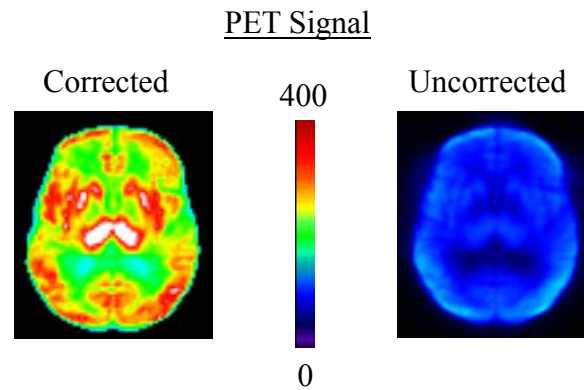
Figure 2.4: Simulated PET images displaying the detrimental effect of photon attenuation.

The deflected trajectory of some scattered photons still leads them towards the PET

detector ring where they are collected in a different detector than originally intended. If this

occurs within the coincidence time window, the resulting LOR does not accurately represent a

line along which the annihilation event occurred. This phenomenon is known as *scatter*. Some

scattered photons are deflected completely out of the range of the PET detector rings. This

phenomenon where the photons are not detected is known as *attenuation* (Section 2.3). This

distinction is important because the presence of scattered photons in the PET raw data

adversely affects image reconstruction. The attenuation correction component of PET

reconstruction assumes that scattered photons are removed from the data, a principle known as

the narrow-beam condition. Therefore, scattered photons must be identified and discarded prior

to performing attenuation correction. If scatter correction is not performed, the PET images

after attenuation correction will broadly overestimate the true PET signal *(1)*.

There are various approaches that can be used to perform scatter correction. One

approach is to use energy windows to isolate scattered photons from photons unaffected by

scatter. Since scattered photons arrive at the detectors with less energy than unscattered

photons, the energy of the detected photons can be used to identify the photons that have been scattered *(1)*. Another approach, which is utilized by the vendor to perform scatter correction in PET/MRI, is known as single-scatter simulation *(3)*. In this method, simulations are conducted using seeds placed in the attenuation map (Section 2.5) generated for the patient in order to estimate the amount of scatter along all possible LORs. These scatter estimates are then subtracted from the acquired PET data to yield the scatter-corrected data. While scatter correction itself is outside the scope of this dissertation, it is important to note that scatter must be addressed prior to performing attenuation correction in order to satisfy the narrow-beam condition. In addition, the scatter correction method utilized by the vendor employs the same attenuation map as the routine for performing attenuation correction, which could result in a compounding of errors if the attenuation map used is not sufficiently accurate.

**2.5 Attenuation Correction**

The basic principle behind attenuation correction is to estimate the percentage of photons that are expected to be attenuated along any given LOR and to compensate for this by modifying the PET raw data accordingly. In order to perform such a correction, knowledge of the likelihood of attenuation along all possible LORs in the PET field-of-view is required. This likelihood depends on both the linear attenuation coefficient (LAC), which is a function of electron density, and the thickness of all tissues along a particular LOR. This attenuation information is organized in the form of an *attenuation map* whose image intensities represent the LAC values at all locations in the field-of-view. The equation for determining the fraction of photons that are expected to be attenuated is shown in Equation 2.2, where $\mu$ represents the LAC value, $L$ represents thickness, and $P/P_0$ represents the fraction of photons that are not attenuated. When forming the attenuation map, the thickness of tissues is ignored since the

15

field-of-view is divided into equally sized voxels. This attenuation map is then integrated into the OSEM reconstruction method to perform the correction for photon attenuation. The primary challenge in attenuation correction lies in the measurement of tissue LAC values for all regions in the PET field-of-view.

$$\frac{P}{P_0} = e^{-\mu L} \tag{2.2}$$

In stand-alone PET systems, this map of linear attenuation coefficients, referred to as a *μ-map*, is acquired using a rotating radiation source that emits gamma photons which travel through the patient's body, similar to CT imaging. Since the number of photons emitted is known and the number of photons detected can be measured, Equation 2.2 can be used to compute the corresponding LAC values. However, the number of photons emitted by the gamma source is relatively low, and a fairly long acquisition time is needed in order to achieve an adequate signal-to-noise ratio (SNR) in the attenuation map. This difficulty in acquiring attenuation maps was a major reason for the development of hybrid PET/CT systems and their eventual replacement of stand-alone PET systems.

**2.6 CT-based Attenuation Correction**

In PET/CT systems, a quick CT scan provides an image that can be transformed and used for PET attenuation correction (AC). CT systems utilize the attenuation of x-rays transmitted through a patient's body as the source of contrast and are also governed by Equation 2.2. Therefore, CT inherently measures the physical parameter of interest in PET attenuation correction, rendering it a logical choice to integrate with PET in order to provide the necessary information. Prior to incorporation, a transformation of CT data is necessary due to the energy dependence of linear attenuation coefficients. High energy photons such as the 511 keV gamma photons in PET are attenuated in greater numbers than low energy photons

such as the approximately 100 keV x-ray photons in CT. More details about the CT-based attenuation correction (CTAC) method, which is regarded as the current gold standard for performing AC in PET, are provided in Chapter 5.

## 2.7 MRI-based Attenuation Correction

While attenuation correction is fairly straightforward in PET/CT due to the relevant information provided by the CT component of the system, this is not the case in PET/MRI systems. MRI signals are primarily dependent on proton density and tissue magnetization relaxation characteristics (Chapter 3); as a consequence, MRI does not directly provide the measure of electron density necessary to correct for photon attenuation. Furthermore, conventional MRI does not provide much information about the primary biological attenuator of photons per unit volume in the human body: bone. In conventional MR images, bone and air are virtually indistinguishable, but they possess LAC values that are on opposite ends of the spectrum. Several studies have commented on the errors introduced into PET reconstructions if bone is ignored in the attenuation map *(4)*.

PET is very effective as a quantitative imaging modality, providing insight about physiological functions by measuring the uptake of injected radiotracers. If this quantitative advantage is to be maintained, errors in PET images, such as the ones produced through inadequate attenuation correction, cannot be tolerated. Thus, development of an accurate MRI-based correction for photon attenuation is paramount. There are existing methods (Chapter 4) that seek to address this issue, but none of them has emerged as the standard for MRI-based attenuation correction (MRAC). To understand both the limitations of MRI to this application and, ironically, how the versatility of MRI can be used to produce an elegant solution to this problem, a thorough background of MRI is required. (Chapter 3)

# REFERENCES

1. Bailey D, Townsend D, Valk P, Maisey M, eds. *Positron Emission Tomography:  Basic Sciences.* London: Springer-Verlag London; 2005.

2. Alessio A, Kinahan P. PET image reconstruction. In: Karesh S, Halama J, Wagner R, Zimmer A, Henkin R, eds. *Nuclear Medicine, 2nd Edition.* Elsevier; 2006.

3. Accorsi R, Adam LE, Werner ME, Karp JS. Optimization of a fully 3D single scatter simulation algorithm for 3D PET. *Phys Med Biol*. 2004;49:2577-2598.

4. Andersen FL, Ladefoged CN, Beyer T, et al. Combined PET/MR imaging in neurology: MR-based attenuation correction implies a strong spatial bias when ignoring bone. *Neuroimage*. 2014;84:206-216.

# CHAPTER 3: MAGNETIC RESONANCE IMAGING

## 3.1 Equilibrium Magnetization

Magnetic resonance imaging (MRI) was initially dubbed *nuclear magnetic resonance imaging*, but the name was subsequently shortened due to the negative connotations attached to the term "nuclear" during the Cold War era. This change is unfortunate since "nuclear" precisely describes the particle being imaged in MRI: the atomic nucleus. In most cases, it is the nuclei of hydrogen atoms ($^1$H) in water molecules, which consist of a single proton, that are of interest in MRI. Although other nuclei may also be used in MR, the $^1$H nuclei (hereby known simply as "proton") are chosen due to the abundance of water in the human body and because these nuclei exhibit non-zero nuclear magnetic moments arising from the *spin* of the proton. Using classical physics, spin can be visualized as a rotation of the object about an axis, but this explanation alone does not suffice to explain the origins of signal in MRI. Therefore, some discussion in terms of quantum mechanics is required.

In quantum mechanical terms, spin provides particles with *angular momentum* and a *magnetic moment*, both of which are expressed as vectors with discrete magnitudes and orientations. While the orientation of a particle's spin may change, the quantum number, i.e. the magnitude, associated with it does not change. These spin quantum numbers start at ½ and can exist in increments of 1 thereafter (ex: ½, $^3/_2$, $^5/_2$ ...). The direction can be indicated as either a positive or a negative spin number (ex: + ½ , - ½ ). The Pauli Exclusion Principle states that two particles with the same spin number and orientation cannot exist in the same location. This forces the particles to be paired with spins of opposite orientations, resulting in the cancellation

of spins for nuclei with even numbered protons and even numbered neutrons. Other nuclei, such as the $^1$H nucleus, exhibit a non-zero spin because they contain an odd number of protons, an odd number of neutrons, or both. This leads to a net nuclear spin for atoms with nuclei of these compositions. Since the nucleus of a $^1$H atom contains a single unpaired proton, $^1$H exhibits a net spin of ½ and contains an angular momentum and a magnetic moment associated with that spin. Equation 3.1 displays the relationship between the angular momentum (**J**) and the magnetic moment (**μ**). The term $\gamma$ in Equation 3.1 is known as the *gyromagnetic ratio*. For protons, $\frac{\gamma}{2\pi}$ = 42.58 MHz/T; for electrons, $\frac{\gamma}{2\pi}$ = 28,025 MHz/T *(1)*.

$$\mu = \gamma \cdot J \tag{3.1}$$

From this point on, a classical view of magnetism will used in lieu of a quantum mechanical view for the sake of simplicity. In their natural state, the magnetic moments associated with $^1$H nuclei in the human body are randomly oriented, resulting in a near-zero vector sum of net magnetization. When a human is placed inside of a strong magnetic field, such as the **B₀** field introduced by an MRI scanner, these individual magnetic moments align with the external field in either the low energy state (in the same direction as the external field) or the high energy state (in the opposite direction). At room temperature, there is a slight preference towards the low energy state, resulting in a non-zero bulk magnetic moment that aligns with the external magnetic field. Since there is an abundance of water in the human body, this bulk magnetic moment, known as the *equilibrium magnetization*, is large enough to be manipulated and detected.

## 3.2 Precession

The vector sum of the magnetization at any given time is represented by a *magnetization vector* (**M**). At equilibrium, the initial vector (**M₀**) is aligned with the direction

of the $\mathbf{B_0}$ field, which is assumed to be the $+z$-axis without loss of generality. While $\mathbf{M_0}$ is aligned with the external magnetic field, the individual magnetic moments of the spins that compose $\mathbf{M_0}$ precess about the $\mathbf{B_0}$ field (Figure 3.1A). This precession phenomenon arises due to the intrinsic angular momentum of the protons and is analogous to the precession of a spinning top about the gravitational field of the earth. For instance, if a top is placed on a table on its sharp end, it will topple over immediately. If the same top is spun about its axis prior to release, the top will precess about the earth's gravitational field until it loses a significant portion of its angular momentum (Figure 3.1B).
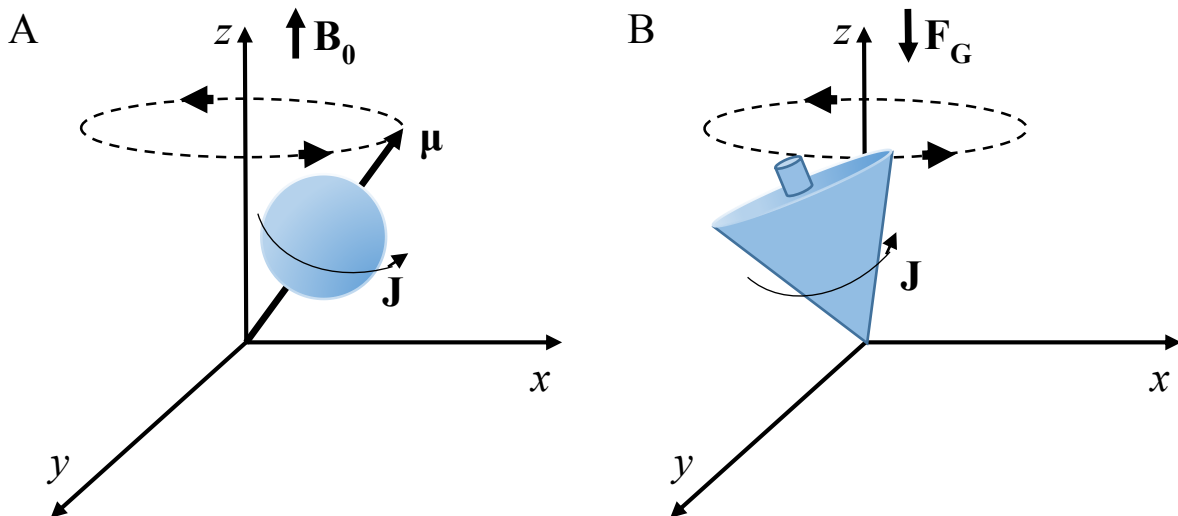


Figure 3.1: The precession of a proton's magnetic moment around the magnetic field (A) is analogous to the precession of a spinning top around the gravitational axis.

The rate of spin precession about a static magnetic field is characterized by the *Larmor frequency* ($\omega_0$). As shown in Equation 3.2, this frequency is a function of both the magnitude of the static $\mathbf{B_0}$ field and the gyromagnetic ratio *(1)*.

$$\omega_0 = \gamma \cdot B_0 \tag{3.2}$$

## 3.3 Radiofrequency Excitation

The net magnetization $\mathbf{M_0}$ is constant and cannot be measured by the receiver coils because only time-varying magnetic flux that cut these coils can be detected. Therefore, radio-

frequency (RF) pulses that are tuned to the Larmor frequency are used to *tip*, or rotate, the magnetic moments of individual spins away from the direction of the main magnetic field. More specifically, this RF pulse effectively rotates the $\mathbf{M_0}$ vector by an arbitrary flip angle (FA) away from the $\mathbf{B_0}$ field, producing a transverse component in the *xy*-plane, or transverse plane, ($\mathbf{M_{xy}}$), and leaving part of the longitudinal component along the *z*-axis ($\mathbf{M_z}$).

As a side note, electrons could theoretically be imaged using MR the way protons are imaged, but the relationship in Equation 3.2 provides a biological limitation on imaging electrons in the human body. Since the value of $\gamma$ for electrons (Section 3.1) is much larger than for protons, the Larmor frequency would also increase by that factor. This increase in frequency requires RF pulses that deposit greater amounts of energy to achieve resonance, too high in fact to safely use on humans.

After the RF pulse is applied and the rotation into the transverse plane is accomplished, the magnetic moments of individual spins tend to realign themselves with the external magnetic field in a process termed *magnetization relaxation*. To describe using the vector notation introduced earlier, $\mathbf{M_{xy}}$ will tend to return to its initial value of zero while $\mathbf{M_z}$ will tend to return to its initial value of $\mathbf{M_0}$.

To summarize the process of acquiring signal in MRI, the net magnetization of all spins is initially aligned with the external magnetic field before an RF pulse is used to rotate part or all of the magnetization into the transverse plane. RF coils are then used to detect the electrical signals induced as the transverse magnetization precesses about the *z*-axis.

The electrical signals produced in the RF coils are recorded in MR imaging space known as *k-space* (more details in Section 3.6). The MR image is then most commonly reconstructed from the imaging space data by utilizing an inverse Fourier transform of the k-

space data. The intensity at any given location in an MR image is a function of the concentration of ^{1}H nuclei (i.e. proton density) and the underlying chemical properties that affect magnetization relaxation. There are two mechanisms through which magnetization relaxation of MR signals occurs: transverse (Section 3.4) and longitudinal (Section 3.5).

**3.4 Transverse Decay**

As mentioned above, the transverse magnetization will tend to relax back to its initial value of zero. This relaxation is also known as *transverse decay* because it describes the *loss* of magnetization in the transverse plane that occurs as a result of the return to the equilibrium. The first-order differential equation that governs the transverse relaxation process is shown in Equation 3.3, where $M_{xy}$ represents the component of the magnetization vector **M** in the transverse plane, while $T_2^*$ and $R_2^*$ respectively represent the time constant and the rate constant for this exponential decay. Since they are reciprocals, $T_2^*$ and $R_2^*$ can be used interchangeably to describe the transverse decay phenomenon.

$$\frac{dM_{xy}}{dt} = -\frac{M_{xy}}{T_2^*} = -(M_{xy}) \cdot R_2^* \qquad (3.3)$$

Transverse decay occurs as a result of the *dephasing* (Figure 3.2) of the spins giving rise to $M_{xy}$. This dephasing can result due to the inhomogeneity in the static field $B_0$ and due to the interactions of spins with each other *(1)*.

One mechanism for transverse magnetization decay is through $B_0$ inhomogeneity. Slight variations in the static $B_0$ magnetic field are caused by the presence of the patient inside the MRI scanner. As suggested by Equation 3.2, this inhomogeneity causes the precession frequency to vary based on position. The differences in the precession frequencies, in turn, cause the spins of interest to be out-of-phase with respect to each other, lowering the magnitude of the magnetization vector $M_{xy}$. The time constant associated with this relaxation is denoted

23

by $T_2'$ whereas the corresponding relaxation rate is denoted by $R_2'$. This type of transverse decay is known as *reversible decay* because certain RF pulses can be used to bring spins back
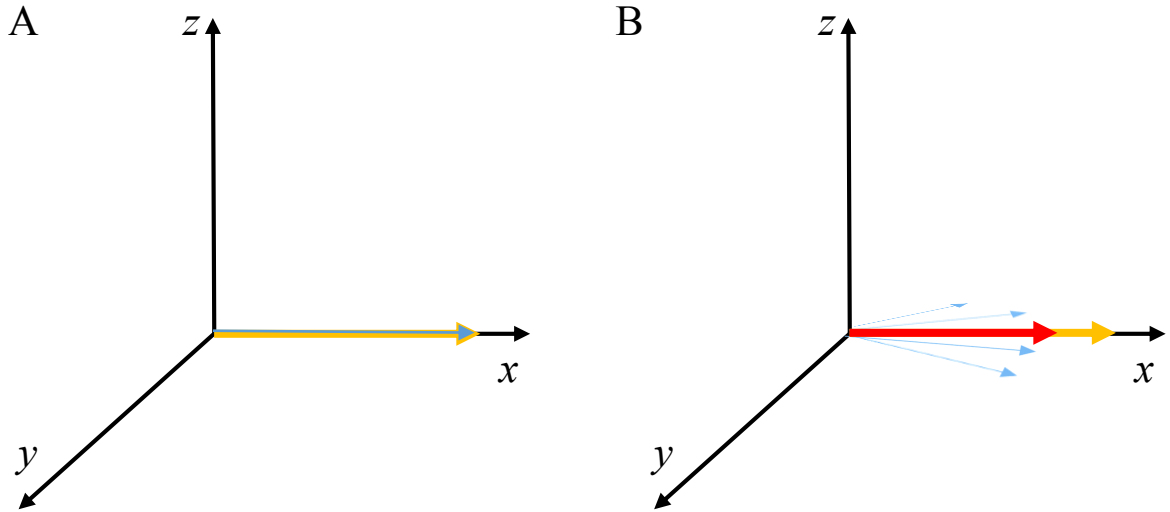


Figure 3.2: After RF excitation, the magnetic moments of the spins (blue) produce a net magnetization vector (gold) in the *xy*-plane (A). Differences in the precession frequencies cause a dephasing effect that lowers the net magnetization (red) (B).

in-phase at a future time-point prior to signal acquisition.

Differences in precession frequencies can also occur due to spin-spin interactions. Since individual spins impose their own individual magnetic moments, there exists a minute magnetic field around each spin. The effect of the magnetic field of one spin on the surrounding spins changes the magnetic field experienced by those spins, resulting in dephasing. This type of transverse decay is known as *irreversible decay* because it cannot be reversed using MR sequence techniques. The time constant associated with this relaxation is denoted by the spin-spin relaxation time $T_2$ while the corresponding relaxation rate is denoted by $R_2$. $T_2$ relaxation is influenced by the underlying chemical structure. Values of $T_2$ are much shorter for solids (on the order of $\mu s$) and much longer for liquids (on the order of $s$).

The resulting transverse decay time ($T_2^*$) and the corresponding transverse relaxation rate rate ($R_2^*$) can be computed as shown in Equations 3.4 and 3.5.

$$\frac{1}{T_2^*} = \frac{1}{T_2} + \frac{1}{T_2'} \tag{3.4}$$

$$R_2^* = R_2 + R_2' \tag{3.5}$$

The evolution of $\mathbf{M_{xy}}$ as a result of the transverse decay is illustrated in Figure 3.3. The changes in the transverse magnetization observed are as seen in the curve associated with $T2^*$ decay unless an aforementioned technique is used to reverse the dephasing effects of $\mathbf{B_0}$ inhomogeneity *(1)*.
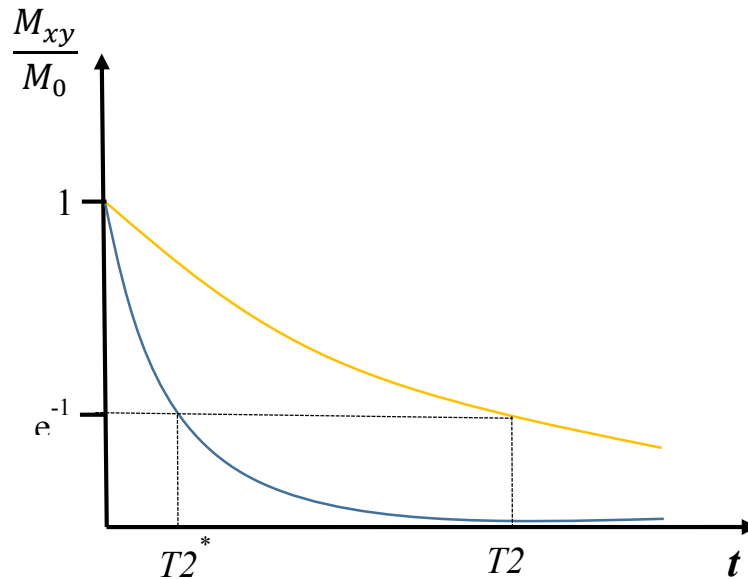


Figure 3.3: The decay of transverse magnetization associated with T2*
(blue) is faster than the decay associated with T2 (gold).

## 3.5 Longitudinal Recovery

Longitudinal magnetization relaxation is also known as *longitudinal recovery* because it describes the *recovery* of the magnetization along the longitudinal axis (parallel to the static magnetic field). Equation 3.6 shows the first-order differential equation that governs the longitudinal relaxation process, where $\mathbf{M_z}$ represents the component of the magnetization

vector along the longitudinal axis, $T_1$ represents the time constant for this relaxation, and $R_1$ represents the corresponding relaxation rate, illustrated in Figure 3.4.

$$\frac{dM_z}{dt} = \frac{M_0 - M_z}{T_1} = (M_0 - M_z) \cdot R_1 \tag{3.6}$$

$T_1$ and $R_1$ are known as the spin-lattice relaxation time and the spin-lattice relaxation rate, respectively, because the energy deposited by the RF excitation is dissipated into the surrounding molecules, or the *lattice (1)*. Since they are reciprocals, $T_1$ and $R_1$ can be used interchangeably to describe the longitudinal recovery phenomenon.
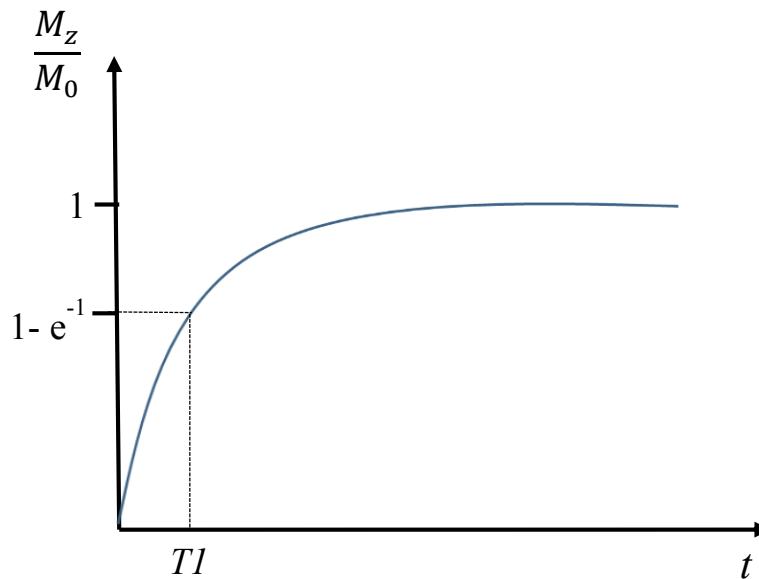


Figure 3.4: The recovery of longitudinal magnetization associated with T1 (blue) is exponential and approaches the equilibrium magnetization.

## 3.6 Pulse Sequences and Image Acquisition

An MRI pulse sequence is the collective execution of system components in order to achieve excitation and signal acquisition. One of the most basic sequences in MRI is the *gradient recalled echo* (GRE) sequence. In a typical GRE-based sequence, RF excitation is used to tip the magnetization of spins located in a particular *volume of interest* by a certain flip angle from the longitudinal axis. After a short time passes and a certain amount of relaxation

occurs, signal is acquired from these spins and reconstructed into an MR image of that volume. This MR signal, and consequently the resulting image, is a function of the number of spins present in the volume, or *proton density* ($\rho$), and the relaxation phenomenon discussed in Sections 3.4 and 3.5.

GRE pulse sequences can be used to acquire images in 2D, where the volume of interest consists of a *slice*, or in 3D, where the volume of interest consists of a *slab*. In 2D imaging, the slice to be acquired is isolated using magnetic gradient fields, known as the *slice-select gradient* (**Gss**). These gradients slightly alter the static **B₀** magnetic field along a given axis. While this axis can be chosen to lie in any direction, the longitudinal axis (*z*) parallel to the **B₀** field is used most commonly. According to Equation 3.2, changing the $B_0$ value along an axis in a predictable manner causes the frequency of the spinning protons to exhibit a certain pattern according to their position along that axis. The magnitude and the sign of this slice-select gradient can be used to alter the Larmor frequency across the patient. The RF pulse, which is tuned to the frequency corresponding to the slice of interest, is applied concurrently and, depending on the desired flip angle, tips a certain percentage of the magnetization in that slice to the transverse plane. Similarly, gradients applied in the transverse place, known as the *read-out gradient* (**G**RO) and the *phase-encoding gradient* (**G**PE), are used to encode the frequency based on location within each slice. A frequency domain table, termed k-space, is then built up by changing **G**PE and **G**RO. Later, the k-space for each slice is transformed into an image using the inverse 2D Fourier transform. Conventionally, the time from the center of the RF pulse to the center of the acquisition window is known as the *echo time* (TE) because the spins will be fully refocused at that time by the judicious use of the gradient waveform. The time between one RF excitation and the next is known as the *repetition time* (TR).

In 3D MR imaging, the excited region consists of all of the spins in the field-of-view of the RF transmitting coil. In the case of head and neck imaging, an RF coil would be used to excite the region of the body superior to the shoulders. The three gradients, named after each principal direction (Gx, Gy, and Gz), are then used to manipulate which part of the 3D k-space is filled out with MR signal data. Once the acquisition is complete, the 3D k-space data is transformed into a 3D image using the inverse 3D Fourier transform. Figure 3.5 illustrates an example of a 3D GRE pulse sequence *(1)*.
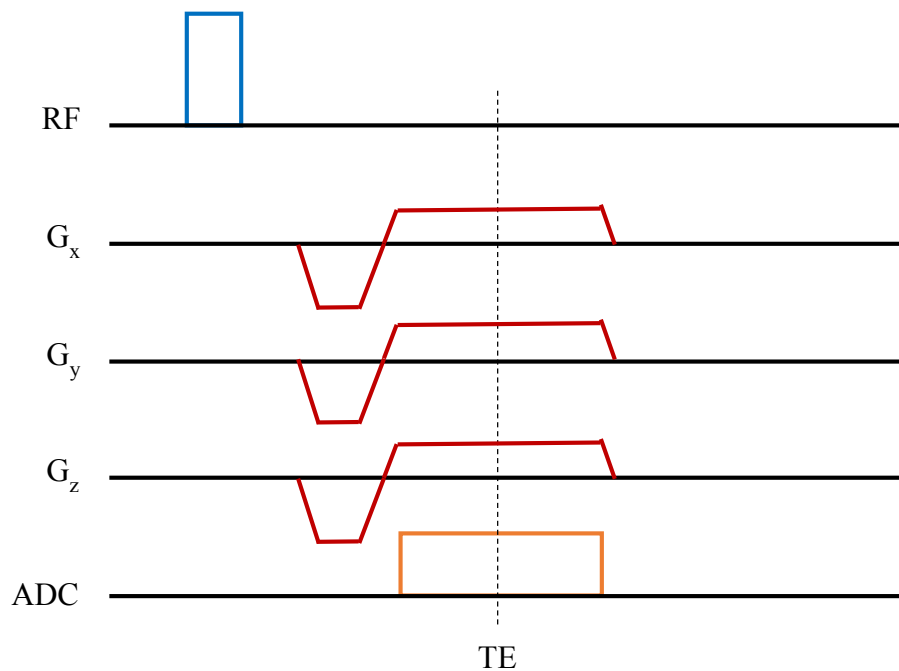


Figure 3.5: Pulse sequence diagram for a conventional 3D GRE sequence.

## 3.7 Shortcomings of MR in Attenuation Correction

In this chapter, the origin of MRI signals and their dependence on water proton density and tissue magnetization relaxation characteristics has been described. As discussed in Chapter 2, the linear attenuation coefficients that reflect the probability of attenuation of PET photons are a function of tissue electron density. A shortcoming of MR is that it cannot be used to safely image electrons *in vivo* due to the tremendous amount of RF energy required (Section 3.3).

This fundamental mismatch between the source of MR signal and the cause of attenuation results in the difficulties encountered in MR-based attenuation correction (MRAC). Furthermore, bone is the primary biological attenuator of PET photons per unit volume in the body and exhibits higher LAC values than any other tissue. Bone also exhibits some of the highest $R2^*$ and $R_1$ values observed in biological tissues. In conventional MR sequences, such as the GRE sequence discussed in Section 3.5, where the echo times are on the order of tens of *ms*, signal from bone decays almost completely before signal acquisition. This renders conventional MRI relatively useless for imaging bone tissue. Recent advances in hardware have allowed for the shortening of TE values to a few *μs*. This allows acquisition of signal to begin much faster and signal from bone tissue to be captured before it decays completely. These extremely short TEs are the biggest advantage offered by *ultrashort echo time* (UTE) MR imaging.

**3.8 Ultrashort Echo Time Imaging**

The shortest TEs offered by UTE-MRI pulse sequences can be achieved using a 3D GRE sequence with a radial acquisition of k-space data. 3D radial acquisition allows for the acquisition of signal to begin as soon as possible after the RF excitation without the need to wait for further encoding by gradients. Figure 3.6 illustrates a pulse sequence for a standard 3D UTE sequence. In UTE imaging, the TE is defined as the time between the center of the RF pulse and the time at which the center of k-space is sampled. Since there are no pre-phasing gradients used, the center of k-space is sampled right at the beginning of the gradient ramp-up. UTE sequences can be utilized to image any region of the body and can be manipulated to collect the information necessary to compute $R_1$ and $R_2^*$. Since bone tissue exhibits the fastest relaxation rates of any tissue, these parameters could aid in identification of bone for PET

attenuation correction. This approach, particularly the use of relaxation rate $R_2^*$, forms the foundation upon which many of the existing MR-based attenuation correction methods in existence today are based (Chapters 4-6).
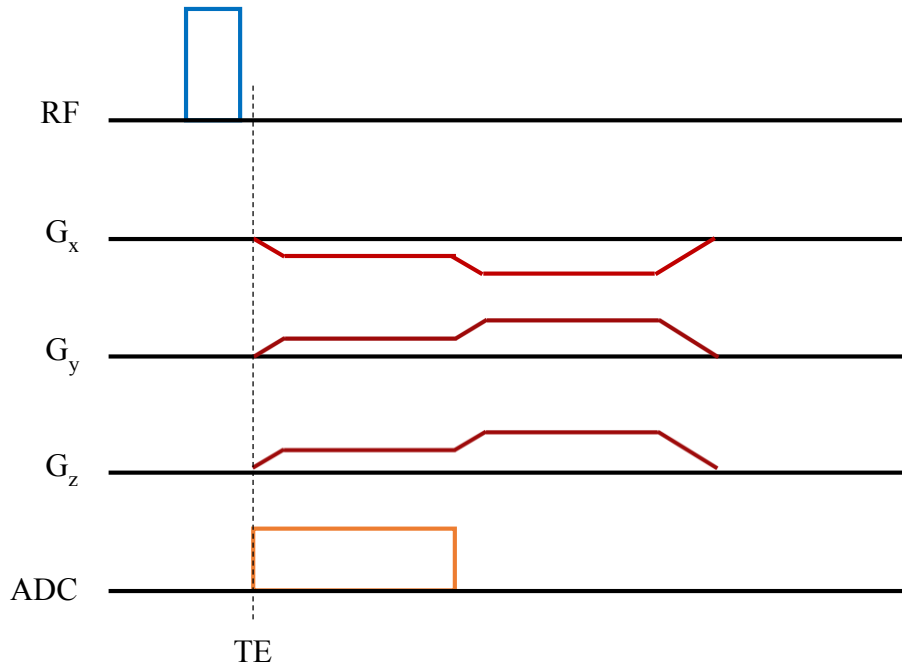


Figure 3.6: Pulse sequence diagram for 3D UTE GRE sequence.

# REFERENCES

1. Haacke E, Brown R, Thompson M, Venkatesan R. *Magnetic Resonance Imaging: Physical Principles and Sequence Design.* 1st ed. New York: Wiley-Liss; 1999.

## CHAPTER 4: EXISTING METHODS

### 4.1 Overview

Initial studies investigating MRI-based or MRI-compatible (MRAC) methods for PET photon attenuation correction were conducted long before the first hybrid PET/MRI system was introduced to the market *(1)*. The level of attention given to this problem is a testament to both the potential benefits of PET/MRI systems and to the anticipated challenge of using MRI to perform attenuation correction. To that end, there are several classes of methods that have been proposed to derive the attenuation maps necessary for attenuation correction in hybrid PET/MRI systems: PET-based methods *(2, 3)*, template-based methods *(4)*, atlas-based methods *(5, 6)*, segmentation-based methods *(7, 8, 9)*, and mapping-based methods *(10)*. Once these attenuation maps are generated for each patient, they can be used to make the correction for attenuation during the reconstruction step of PET data processing pipeline.

### 4.1 PET-based Methods

The first class of methods aims to produce attenuation maps using PET data alone, either by adding a rotating radiation source into the PET/MRI system for transmission imaging (as is done in stand-alone PET systems) *(2)* or by utilizing emission PET data and statistical algorithms to derive the attenuation map necessary for correction *(3)*. One of these algorithms is the maximum likelihood reconstruction of activity and attenuation (MLAA) method. In this method, the activity distribution along with the corresponding attenuation map are simultaneously estimated using an iterative process. Both methods are collectively referred to as PET-based attenuation correction methods and will not be discussed further in this

dissertation since they possess certain limitations crippling their chances of being adopted into standard practice. For example, transmission PET methods require either major modifications to existing systems or the insertion of an external component that would reduce the bore size available to place the patient. While the vendor currently employs the MLAA method to derive portions of patient attenuation maps that are outside of the MR field-of-view, emission based methods are also typically not utilized for the entire attenuation map due to poor accuracy.

## 4.2 Template-based Methods

Template-based approaches also employ PET-derived information in order to derive the attenuation map, but this information is not acquired directly from the patient being imaged. Instead, the attenuation map is derived from a template image which is acquired using a transmission scan on a single test subject or is an average over attenuation maps acquired from multiple subjects. An MR image of the template subject (or average MR image over all
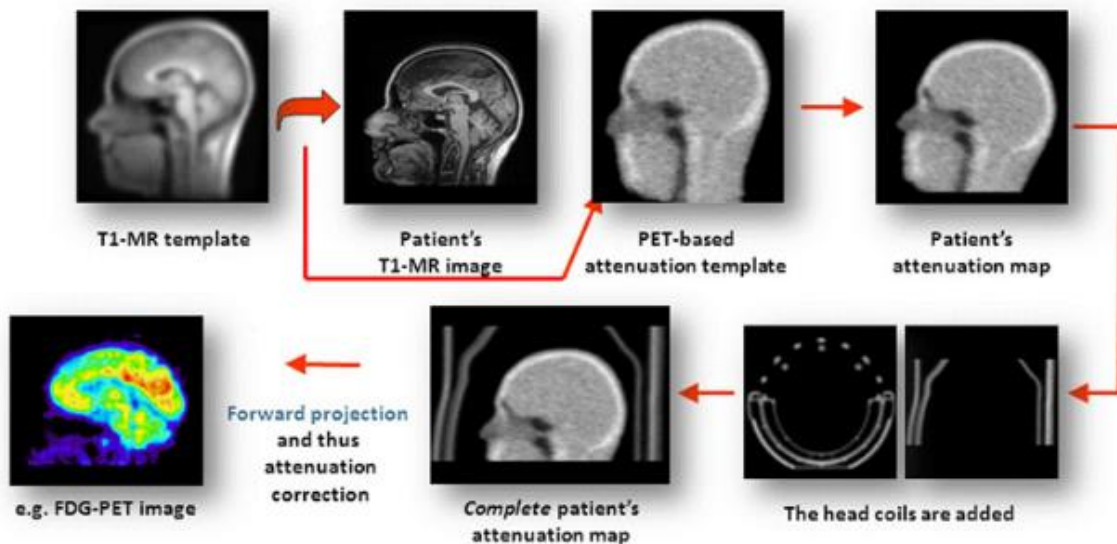


Figure 4.1: Representative flow chart for template-based MRAC methods *(11)*.

template subjects) is co-registered with the corresponding PET attenuation map. This template MR image, as illustrated in Figure 4.1, is then registered to the patient's MR image and the corresponding transformation is applied to the template attenuation map to derive an estimate

of the patient's attenuation map. These approaches are fairly simple but their accuracy depends on the underlying assumption that the template image can be deformed into the patient's MR image with sufficient accuracy. Any major differences in anatomy would have a detrimental effect on the accuracy of these methods.

## 4.3 Atlas-based Methods

Atlas-based methods *(5, 6)* typically rely on a precompiled atlas of paired MR and CT images and a complex algorithm to generate an artificial CT image (pseudo-CT) from patient MR images. These pseudo-CTs are subsequently converted to PET attenuation maps through the same piecewise linear scaling operation used in CT-based attenuation correction (CTAC).

An example of an atlas-based method is one developed by Yasheng Chen *et al*. (2014) which is outlined in Figure 4.2 and briefly described here. This method employs an atlas of
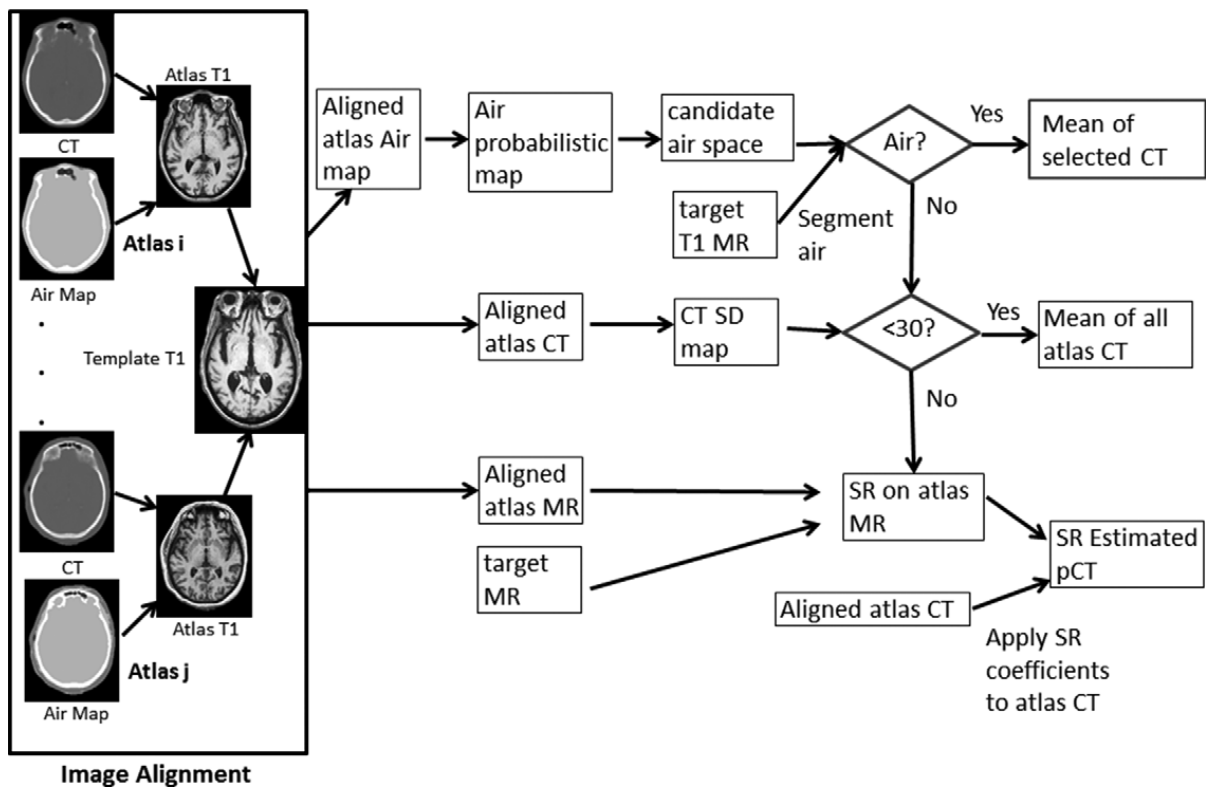


Figure 4.2: A flow chart of the derivation of pseudo CTs using the PASSR method *(6)*.

34

paired $T_1$-weighted MR and CT images and a $T_1$-weighted MR image of the patient in question. Since bone and air appear alike in conventional MR images, such as $T_1$-weighted images, air classification was addressed first. Air segmentation is achieved using a Markov random field (MRF) approach on regions classified as potentially belonging to air by atlas-derived probabilistic air maps. The candidate air space is defined as all voxels with a probability of air greater than 20%. Then, a two class MRF segmentation is utilized within the candidate air space to perform the final classification for air voxels. Finally, CT-HU values are assigned to these values by averaging the CT-HU values of all atlas CT images that classified a particular voxel as air.

For soft tissue and bone regions, a patch-based sparse regression approach is used to estimate the CT-HU values. A template patch ($P_t$) is defined as a 3D volume around a given voxel in the patient's MR image and a search was conducted to select the most relevant patch among all patches ($P_{MR}$) available in corresponding regions of the atlas MR images. This is accomplished using an elastic net method and the minimization of Equation 4.1 to derive the weighting ($\alpha$) of each atlas patch on the template patch.

$$\min \frac{1}{2} \| P_t - \alpha P_{MR} \|^2 + \lambda_1 \| \alpha \| + \lambda_2 \| \alpha \|^2 \qquad (2.1)$$

The values of $\lambda_1$ and $\lambda_2$ represent the weighting terms for the sparse and ridge regression terms, respectively. This approach produces a *pseudo CT* for the patient based on the MR and CT images from the atlas. The pseudo CT is then scaled to a PET attenuation map using a conversion equation from PET/CT. This method was named PASSR (for Probabilistic Air Segmentation and Sparse Regression) and was validated using a leave-one-out approach in 20 subjects. In this study, the PASSR method yielded a sample mean absolute percent error

35

(MAPE) value of 2.42% with a standard deviation of approximately 1% in whole-brain when PET reconstructions using this method were compared to PET reconstructions performed using the gold standard CT-based method.

The advantages of this method are that it emphasizes local information and provides highly accurate PET reconstructions. A significant drawback is that the attenuation maps require a lengthy amount of time (mean computation time = 10.5 hours) to be generated *(6)*. Furthermore, variations in the patient's anatomy cannot be accurately captured unless this variation is represented in the atlas. These drawbacks are common among atlas-based methods in general and exhibit a need for simpler, more patient-specific MRAC methods *(11)*.

### 4.4 Segmentation based Methods

Segmentation-based approaches utilize MR images and segmentation algorithms to classify the voxels present in the FOV into a number of tissues. Each tissue is then assigned an LAC value that most closely represents all voxels of that tissue. These approaches differ from their atlas-based counterparts in that they are generally quick and generate attenuation maps from patient MR images alone (patient-specific) *(12)*. Initial approaches utilized conventional MR images, such as T1-weighted images, and existing algorithms, such as k-means clustering, to perform the segmentation. Next, methods using Dixon-based fat/water separation were presented *(13, 14)*, but the lack of bone delineation adversely affects the accuracy of these methods in the head and neck region.

Recently, UTE-MRI sequences have been proposed as a means of identifying bone tissue, which is difficult to distinguish using conventional MRI (Chapter 3). These approaches utilized dual-echo UTE (DUTE) methods to identify regions of bone by examining differences in images acquired with and without bone signal present (first and second echo, respectively).

36

Keereman et al. *(7)* used an approach based on $R2^*$ signal decay between the first and second echoes to identify regions of bone and a region-growing approach to identify regions of air. Catana et al. *(8)* used arithmetic operations on DUTE images after normalization to identify regions of bone and air. Berker et al. *(9)* presented a method that distinguishes bone/air regions using arithmetic operations on UTE images and differentiates fat/water regions using a Dixon-based separation. Two advantages of segmentation-based methods, relative to atlas methods, are shorter computation time and better representation of inter-patient anatomical variation. However, segmentation-based methods tend to produce less accurate PET reconstructions compared to atlas-based methods *(12)*. This reduced accuracy may result from incorrect segmentation of tissues and/or the homogeneous representation of bone LACs. Therefore, a method that provides better segmentation of tissues as well as a continuous-valued LAC representation of bone tissue without significantly improving computation time would be advantageous.

**4.5 Mapping-based methods**

Mapping-based approaches are relatively novel and utilize the segmentation of UTE-MRI images as a pre-cursor before assigning continuous-valued LACs to one or more tissues in the field-of-view using primarily patient MR information. Although the possibility of using $R2^*$ information to estimate CT values was postulated by Delso *et al*. *(15)*, the first method utilizing this approach was presented by Cabello *et al. (10)*. In this method, $R2^*$ values in bone were normalized and empirically mapped to PET LAC values based on the mode and standard deviation of the $R2^*$ value. Additionally, an intensity equalization step was used to match the intensity histogram of the $R2^*$ method to that of the CT-based method.

Recently, a method based on water- and fat-suppressed proton projection imaging (WASPI) utilizing a zero echo time (ZTE) sequence was proposed to measure bone density for the purposes of PET attenuation correction *(16)*. WASPI suppresses most fat and water signals, leaving only signal from the short-$T_2$ components present in the bone matrix. ZTE imaging provides acquisition at an echo time of essentially zero, allowing for acquisition of signal short-$T_2$ tissues that are missed by UTE imaging. Image intensities from this technique were correlated with LAC values and were used to provide continuous-valued attenuation coefficients for bone. PET reconstructions from this method better agreed with CT-based reconstructions than the vendor-provided method.

Another recent method from Wiesinger *et al*. *(17)* also utilizes a ZTE sequence along with sequence parameters that enabled proton density weighting. The negative log of the image intensities from this sequence were correlated to CT-Hounsfield units and were proposed as a means to derive continuous-valued LACs for all tissues of the head. While this method is presented as a potential MR-based attenuation correction approach, no PET results were reported in this study.

## 4.6 Vendor-provided Methods

Two commonly used vendor-provided MRAC methods are the Dixon-based method (vDixon) and the UTE-based method (vUTE). Both of these correction methods fall under the umbrella of segmentation-based approaches with similarities to the methods presented by Martinez-Moller *et al*. (vDixon) *(13)* and Catana *et al.* (vUTE) *(8)*, respectively. The vDixon method employs in- and opposed-phase MR images to derive classifications for air, adipose tissue, and soft tissue before assigning a single LAC value to represent all voxels of each class. While these methods are not as accurate as some of the other methods described here, they are

utilized by the vendor in PET/MRI systems in part due to the rapid computation time of the attenuation maps.

## 4.7 Summary

There are many classes of MRAC methods that have been proposed in literature, including atlas-based, segmentation-based, and mapping-based methods. Atlas-based approaches suffer from lengthy computation times while segmentation-based approaches suffer from lack of accuracy, in part due to the assumption of LAC homogeneity in tissues. While the three mapping-based methods discussed in Section 4.5 have made some progress in addressing this limitation, they have yet to be rigorously tested on PET data from large numbers of patients. The methods proposed in this dissertation are among the first in the mapping-based class of methods and employ a segmentation of UTE-MRI images to provide attenuation maps with continuous-valued LACs initially for bone (Chapter 5) and eventually for brain and adipose tissue as well (Chapter 6). Furthermore, these methods have been extensively tested, using PET data from large numbers of subjects that span two academic centers.

# REFERENCES

1. Hofmann M, Pichler B, Scholkopf B, Beyer T. Towards quantitative PET/MRI: A review of MR-based attenuation correction techniques. *Eur J Nucl Med Mol Imaging*. 2009;36 Suppl 1:S93-104.

2. Mollet P, Keereman V, Bini J, Izquierdo-Garcia D, Fayad ZA, Vandenberghe S. Improvement of attenuation correction in time-of-flight PET/MR imaging with a positron-emitting source. *J Nucl Med*. 2014;55:329-336.

3. Mehranian A, Zaidi H. Emission-based estimation of lung attenuation coefficients for attenuation correction in time-of-flight PET/MR. *Phys Med Biol*. 2015;60:4813-4833.

4. Montandon ML, Zaidi H. Atlas-guided non-uniform attenuation correction in cerebral 3D PET imaging. *Neuroimage*. 2005;25:278-286.

5. Hofmann M, Steinke F, Scheel V, et al. MRI-based attenuation correction for PET/MRI: A novel approach combining pattern recognition and atlas registration. *J Nucl Med*. 2008;49:1875-1883.

6. Chen Y, Juttukonda M, Su Y, et al. Probabilistic air segmentation and sparse regression estimated pseudo CT for PET/MR attenuation correction. *Radiology*. 2015;275:562-569.

7. Keereman V, Fierens Y, Broux T, De Deene Y, Lonneux M, Vandenberghe S. MRI-based attenuation correction for PET/MRI using ultrashort echo time sequences. *J Nucl Med*. 2010;51:812-818.

8. Catana C, van der Kouwe A, Benner T, et al. Toward implementing an MRI-based PET attenuation-correction method for neurologic studies on the MR-PET brain prototype. *J Nucl Med*. 2010;51:1431-1438.

9. Berker Y, Franke J, Salomon A, et al. MRI-based attenuation correction for hybrid PET/MRI systems: A 4-class tissue segmentation technique using a combined ultrashort-echo-time/Dixon MRI sequence. *J Nucl Med*. 2012;53:796-804.

10. Cabello J, Lukas M, Forster S, Pyka T, Nekolla SG, Ziegler SI. MR-based attenuation correction using ultrashort-echo-time pulse sequences in dementia patients. *J Nucl Med*. 2015;56:423-429.

11. Wagenknecht G, Kaiser HJ, Mottaghy FM, Herzog H. MRI for attenuation correction in PET: Methods and challenges. *MAGMA*. 2013;26:99-113.

12. Bezrukov I, Mantlik F, Schmidt H, Scholkopf B, Pichler BJ. MR-based PET attenuation correction for PET/MR imaging. *Semin Nucl Med*. 2013;43:45-59.

13. Martinez-Moller A, Souvatzoglou M, Delso G, et al. Tissue classification as a potential approach for attenuation correction in whole-body PET/MRI: Evaluation with PET/CT data. *J Nucl Med*. 2009;50:520-526.

14. Eiber M, Martinez-Moller A, Souvatzoglou M, et al. Value of a dixon-based MR/PET attenuation correction sequence for the localization and evaluation of PET-positive lesions. *Eur J Nucl Med Mol Imaging*. 2011;38:1691-1701.

15. Delso G, Carl M, Wiesinger F, et al. Anatomic evaluation of 3-dimensional ultrashort-echo-time bone maps for PET/MR attenuation correction. *J Nucl Med*. 2014;55:780-785.

16. Huang C, Ouyang J, Reese TG, Wu Y, El Fakhr G, Ackerman JJH. Continuous bone density measurement for simultaneous MR-PET attenuation correction using water- and fat-suppressed projection imaging (WASPI). *International Society for Magnetic Resonance in Medicine*. Toronto:2015.

17. Wiesinger F, Sacolick LI, Menini A, et al. Zero TE MR bone imaging in the head. *Magn Reson Med*. 2015.

**CHAPTER 5: CAR-RiDR**

**5.1 Overview**

There are two major components of mapping-based MRAC methods: the acquisition of MR images using specialized sequences and the processing of those images to form the PET attenuation maps. The goal of this initial study was to utilize images acquired from standard vendor-provided sequences to develop an improved attenuation map processing scheme for use in PET/MRI neurological studies. Specific aims include accurately identifying regions of bone and air and providing continuous-valued attenuation coefficients for bone via the MR relaxation parameter $R_2^*$. A manuscript summarizing this study was recently published in *Neuroimage (1)*, and a version of that manuscript has been adapted for inclusion in this dissertation as follows.

**5.2 Materials and Methods**

*5.2.1 Image Acquisition and Pre-processing*

PET/MRI and CT datasets were obtained from 98 subjects (mean age [± standard deviation]: 66 years [±9.8], 57 females, 3 with very mild dementia) at Washington University in St. Louis, MO using an IRB-approved protocol and with informed consent. No participants had comorbidities that could interfere with testing, and participants did not receive additional radiotracer administrations within 24 hours. The enrollment exclusion criteria included contraindications to PET, PET/CT, or PET/MRI (e.g. electronic medical devices, inability to lie still for long periods), known claustrophobia, pregnancy, and breast-feeding.

[18]F-Florbetapir (Amyvid [Avid], Eli Lilly, Indianapolis, IN) PET images were acquired for each subject on a hybrid PET/MRI system (Biograph mMR, Siemens AG, Erlangen, Germany). Subjects were injected with 352±29 MBq of ^{18}F-Florbetapir tracer, and PET acquisitions were begun either immediately or 50 minutes after injection. CT images of the head were acquired separately using a PET/CT system (Biograph 40 PET/CT, Siemens AG, Erlangen, Germany). Images were acquired at 120 kVp with a voxel size of $0.59{\times}0.59{\times}3.0$ $mm^3$ and a matrix size of $512{\times}512{\times}74$. The CT and PET/MRI images were acquired within 8.3±6 days of each other with no surgical procedures in between. All images were de-identified before being transferred off-line for image analysis.

DUTE images were acquired using the VB18 version of the UTE AC sequence provided by the vendor. This sequence is considered a "work-in-progress" (WIP). The following imaging parameters were used: repetition time (TR)/echo time 1 ($TE_1$)/echo time 2 ($TE_2$) = 2300/0.07/2.46 ms, acquisition time = 1 min 40 sec, flip angle = 10°, FOV = 300 $mm^2$, and voxel size = $1.56{\times}1.56{\times}1.56$ $mm^3$. Two-point Dixon images were acquired using the vendor-provided Dixon-VIBE AC sequence with the following imaging parameters: $TR/TE_1/TE_2$ = 2300/1.23/2.46 ms, acquisition time = 18 sec, flip angle = 10°, and voxel size = $2.6{\times}2.6{\times}3.12$ $mm^3$. T1-weighted MR (T1-MR) images were acquired using a 3-dimensional magnetization-prepared rapid gradient-echo (MPRAGE) sequence with the following imaging parameters: TR/TE = 2300/2.95 ms, inversion time = 900 ms, acquisition time = 5 min 11 sec, flip angle = 9°, number of partitions = 176, FOV = 256 $mm^2$, and voxel size = $1{\times}1{\times}1.2$ $mm^3$.

Prior to processing, the CT and MR images of each subject were first transformed into μ-map space (i.e. Dixon image space) as required by the vendor-provided PET reconstruction program (e7tools, Siemens Medical Solutions, Knoxville, TN). To achieve this transformation,

the CT, T1-MR, and DUTE images of each subject were registered to the corresponding in-phase Dixon image (already in μ-map space) using a 6-parameter rigid model and mutual information as implemented by the FSL Toolbox (FMRIB, Oxford, United Kingdom). Registration was performed instead of resampling because, in addition to performing resampling, registration also accounts for any shift in subject position between scans. The results of these registrations were manually inspected to ensure good alignment. Images were also inspected for artifacts, and it was found that 89 of 98 subjects exhibited some level of dental artifacts. These artifacts were left uncorrected in order to derive attenuation maps as they are often produced in a clinical setting. All intermediate images derived from the MR data were first computed in their native space and subsequently transformed to μ-map space.

*5.2.2 Tissue Segmentation*

Accurate identification of bone is of paramount importance for two key reasons: 1) it is prominently present in the head, and 2) it has higher LACs than other tissues. In addition, there are three other regions of interest in the head that must be properly identified: air, fat, and soft tissue. $R_2^*$, Dixon-Fat, Dixon-Water, and iUTE images were used as intermediate images to segment bone, fat, soft tissue, and air, respectively, using simple thresholding. Figure 5.1
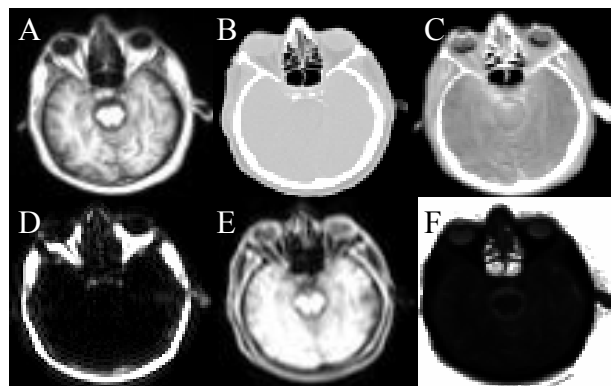


Figure 5.1: Sample slices from T1 (A) and CT (B) are shown here along with corresponding slices from $R_2^*$ (C), Dixon-Fat (D), Dixon-Water (E), and iUTE (F), respectively.

shows the T1 (Figure 5.1A), CT (Figure 5.1B), and the four intermediate images (Figure 5.1 C-F).

*Air*. Since regions of air exhibit the lowest signal intensities in the UTE echo 1 (UTE$_1$) image, the intermediate image for air (Figure 5.1F) was acquired by computing the voxel-wise multiplicative inverse of the UTE$_1$ image (iUTE). The iUTE images were then normalized to their 99$^{th}$ percentile value before a simple threshold (cutoff = 0.06) was applied to segment air.

The cutoff threshold for air in iUTE images was determined using histogram analysis to preferentially select air voxels over bone and CSF voxels and was identical for all subjects. The UTE sequence parameters produce sufficiently high contrast between air and the rest of the head in the iUTE images, as shown in Figure 5.1F, to provide consistently good air segmentation across subjects.

*Bone*. Regions of bone exhibit faster transverse decay characteristics compared to soft tissue. Therefore, the R$_2$$^*$ map for each subject was computed in a similar manner as in *(2)* via Equation 5.1. These R$_2$$^*$ maps were used as the intermediate images for bone segmentation (Figure 5.1C). UTE$_1$/TE$_1$ and UTE$_2$/TE$_2$ represent the images/echo times from the first and second echoes of the DUTE sequence, respectively.

$$R_2^* = \frac{\ln(3 \cdot UTE_1) - \ln(UTE_2)}{TE_2 - TE_1} \tag{5.1}$$

Unusually low voxel intensities in the UTE$_1$ image, presumably due to eddy current effects, resulted in negative R$_2$$^*$ values in some brain regions. To perform a correction for this phenomenon in post-processing, the UTE$_1$ image of each subject was scaled by an empirically-determined factor of three during R$_2$$^*$ computation (Equation 5.1). This was the smallest factor that ensured most brain voxels displayed a higher signal intensity in the UTE$_1$ image than in

the UTE$_2$ image, resulting in positive R$_2$* values. This scaling was performed only for the computation of the R$_2$* maps, and the mention of UTE$_1$ elsewhere in this work refers to the original acquired images. Due to the noisy nature of the R$_2$* images, voxels classified as air were removed from the R$_2$* image prior to thresholding for bone. A simple threshold (cutoff = 550 s$^{-1}$) was then applied to the R$_2$* maps to identify regions of bone. This threshold value, which is slightly higher than the threshold used by Keereman *et al.(2)*, was chosen to select as many bone voxels as possible while minimizing the number of fat and CSF voxels included. As with the threshold for air, the cutoff threshold for bone segmentation was identical for all subjects in the study.

*Adipose and Soft Tissue*. The fat and water images computed by the vendor-provided Dixon sequence were used as the intermediate images for adipose (Figure 5.1D) and soft tissue (Figure 5.1E) segmentation, respectively. Simple thresholds were used to segment both adipose (cutoff = 250) and soft tissue (cutoff = 150). A head mask was derived through binary and morphological operations on the UTE$_1$ image, and any voxel in the mask not already classified as air, bone, adipose tissue, or soft tissue was given a classification of soft tissue. If a voxel was segmented as both adipose and soft tissue, the adipose tissue class was given higher priority. This classification of adipose and soft tissue also serves to reduce erroneous classifications in noisy regions of R$_2$* images. Thus, the proposed segmentation method is hereby referred to as <u>R</u>$_2$* and <u>i</u>UTE-based segmentation with <u>D</u>ixon-based <u>R</u>efinement (RiDR).

*5.2.3 Mapping CT-Hounsfield units using MR parameter R$_2$*

As previously noted, MR signal intensities have no direct correlation with LAC values. However, certain MR decay parameters may be associated with attenuation coefficients. The parameter R$_2$* represents the rate constant of MR signal decay following RF excitation. R$_2$*

incorporates both the transverse irreversible relaxation rate $R_2$ as well as the reversible relaxation rate $R_2$'. Recent studies investigating the microstructure of bone have shed light on the $R_2$ characteristics of the different water domains present in bone. According to Horch *et al.* *(3)*, water present in porous domains (lower density) of cortical bone exhibits a lower $R_2$ value than water present in collagen-bound domains (higher density). Since $R_2$ is a component of $R_2^*$, we postulate that $R_2^*$ values should provide a reasonable measure of bone density, and thus, LAC values.
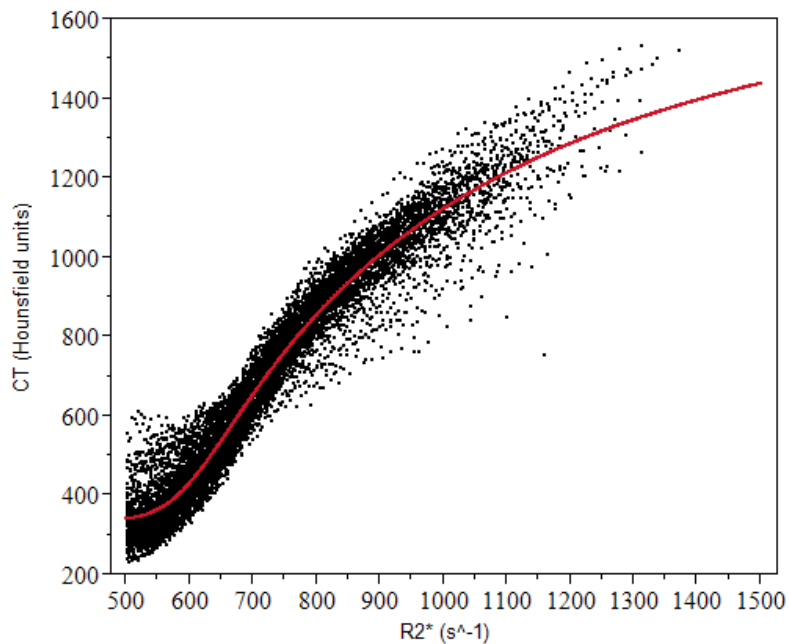


Figure 5.2: A mean R2* vs CT-HU scatter plot derived from 97 subjects using a leave-one-out approach suggests a sigmoid relationship.

Regression analysis was performed between $R_2^*$ and CT-Hounsfield unit (CT-HU) values for each subject using data from voxels classified as bone by both modalities. For CT, any voxel with a value greater than 100 HU was classified as bone *(4)*. This relatively low CT threshold was chosen to provide a complete characterization of the relationship between $R_2^*$ and CT in bone. For $R_2^*$, any voxel with a value greater than 500 $s^{-1}$ was classified as bone *(2)*, which is slightly lower than the $R_2^*$ threshold used for the segmentation. This lower value was chosen to include as many bone voxels as possible when deriving a relationship between MR

$R_2^*$ and CT-HU with the knowledge that misclassifications will be minimized after intersection with the CT classification, a luxury not available during segmentation.

$$CT = D + \frac{A - D}{\left[1 + \left(\frac{R_2^*}{C}\right)^B\right]^G}$$

(5.2)

Due to high levels of noise present in the $R_2^*$ maps, a voxel-by-voxel comparison between $R_2^*$ and CT-HU was avoided. Instead, the following spatially-mapped binning approach was followed. For each subject, the $R_2^*$ values of bone voxels were sorted numerically and divided into 100 bins, each containing an equal number of voxels. For all voxels within an $R_2^*$ bin, the CT-HU values were matched through spatial correspondence from the aligned CT image. The mean $R_2^*$ and CT-HU values of each bin were then computed and plotted for the first 98 bins. The last two bins were excluded due to high levels of noise. A five-parameter sigmoid model (Equation 5.2) was fit to the mean data using the following parameters and conventions: A = lower horizontal asymptote, B = steepness (positive), C = inflection point, D = higher horizontal asymptote, and G = asymmetry of steepness *(5)*.

In order to validate the regression model, a "leave-one-out" procedure was employed. For each subject, an $R_2^*$ vs. CT-HU curve was generated from the remaining 97 subjects using the procedure described in the preceding paragraph. The sigmoid model was derived for a given subject by fitting data (MATLAB and "Five Parameter Logistic Regression", MATLAB Central File Exchange, The Mathworks, Inc., Natick, MA) from the remaining 97 subjects, which produced a conversion equation to estimate CT values from $R_2^*$. A sigmoid relationship derived for an example subject (Figure 5.2) indicates a strong ($r^2$=0.95) correlation between mean $R_2^*$ and CT-HU values. This conversion, dubbed the <u>c</u>ontinuous-valued <u>a</u>ttenuation

coefficients from $\underline{R}_2^*$ (CAR) method, was then employed to generate the bone portion of the PET attenuation maps.

*5.2.4 Formation of Attenuation Maps*

Two attenuation maps were generated for each subject: the gold standard CT-based map and the map derived from the proposed CAR-RiDR method. The vendor-provided Dixon-based attenuation map was not included due to known poor performance resulting from ignoring bone *(6, 7)*.

As presented by Carney *et al.(8)*, the gold standard CT-based map ($\mu_{CT}$) was derived for each subject through piecewise linear scaling of the subject CT image. As shown in Equation 5.3, voxels with values < 50 HU (air-tissue mix) were scaled differently than voxels with values ≥50 HU (tissue-bone mix).

$$\text{Below } 50 \; HU: \mu = \; 9.6 \times 10^{-5} \cdot (HU + \; 1000) cm^{-1}$$

$$\textit{Above } 50 \; HU: \mu = 5.1 \times 10^{-5} \cdot (HU + 1000) + 4.71 \times 10^{-2} \; cm^{-1} \tag{5.3}$$

The RiDR segmentation for bone, air, fat, and soft tissue was used as the basis for the proposed attenuation map ($\mu_{CAR\text{-}RiDR}$). First, each tissue class (excluding bone) was assigned a constant PET LAC value: air = 0 cm$^{-1}$ *(9)*, fat = 0.092 cm$^{-1}$ *(10)*, and soft tissue = 0.1 cm$^{-1}$ *(11)*. Next, $R_2^*$ values in voxels classified as bone were converted to CT-HU values using the CAR relationship. These estimated CT values were translated to PET attenuation coefficients using the same piecewise linear scaling *(8)* employed by the gold standard method.

The vendor-provided UTE (vUTE) attenuation map is derived from a previously published segmentation-based method *(9)*. This map ($\mu_{vUTE}$) provides classifications for bone, air, and soft tissue and uses constant LAC values (0.151 cm$^{-1}$, 0 cm-1, and 0.1 cm$^{-1}$, respectively) for each class.

*5.2.5 PET Data Reconstruction*

PET data for all subjects were acquired from both the head and neck regions. However, acquired CT images had inadequate coverage of the neck region, resulting in gold standard attenuation maps that did not capture the entire PET FOV. This discrepancy in imaging coverage was addressed by replacing affected slices in the gold standard map with slices from the vendor-provided MR Dixon-based attenuation map, which provided full coverage of the head and neck. To ensure fair comparison, this replacement was also performed in the $\mu_{CAR\text{-}RiDR}$ and $\mu_{vUTE}$ maps.

The e7Tools program was used to reconstruct raw list-mode PET data. For each subject, two reconstructions were performed, one using each attenuation map. PET images were reconstructed using an ordered subset expectations maximization (OSEM) algorithm with 3 iterations and 21 subsets to a standard clinical voxel size of 2.09 x 2.09 x 2.03 mm$^3$ and image size of 344 x 344 x 127. Data from six subjects were excluded from PET reconstruction either due to problems with the PET acquisition (n=3) or due to failure of the Dixon fat/water classification (n=3). Analysis of segmentation and PET results was performed on the remaining 92 subjects.

*5.2.6 Data Analysis*

The analysis in this study was designed according to previously presented guidelines *(12)* for evaluating MR-based attenuation correction methods and was conducted using MATLAB software.

RiDR segmentations of bone and air were derived for each subject using the procedure described in Section 5.2.2. CT segmentations were derived from CT images by classifying voxels greater than 300 HU as bone and voxels less than -500 HU as air *(9)*. The segmentation

accuracy of the MR methods (RiDR and vUTE) was analyzed by computing Dice coefficients (Equation 5.4) for bone and air segmentations with respect to the CT-based method. The numerator of Equation 5.4 isolates the intersection, or overlap, between MR and CT classifications, while the denominator corresponds to the total number of voxels identified by both modalities. The sample mean and standard deviation (SD) of the Dice coefficients were then computed for the RiDR method.

$$\text{Dice } coefficient = \frac{2 \cdot (MR \cap CT)}{MR + CT} \tag{5.4}$$

The strength of the regressions in Section 5.2.3 was measured by the coefficient-of-determination ($r^2$), and the accuracy of the model to estimate bone CT-HU values was evaluated via a percent-error comparison with acquired CT images. In order to study the improvement provided by the $R_2^*$ to CT-HU conversion, the accuracy of assigning a single CT value to all bone voxels was also evaluated. First, the CT-HU value corresponding to the routinely assigned LAC value of 0.151 cm$^{-1}$ *(9)* was found through Equation 3 to be 1037 HU. Next, a percent-error computation was performed between the CT-HU values of bone voxels and this constant value. The mean percent-error across subjects was computed for the CAR method and the constant method to gauge the improvement provided by the CAR method.

Percent-error maps were computed for PET images reconstructed with the MR-based attenuation map (PET$_{\text{CAR-RiDR}}$ and PET$_{\text{vUTE}}$) against PET images reconstructed with the gold standard (PET$_{\text{CT}}$). From these error maps, the mean absolute percent-error (MAPE) in whole-brain (Equation 5.5) was computed for each subject, similar to *(13)*, followed by the sample mean and SD. In order to measure the range of errors, the difference between the 95$^{\text{th}}$ and 5$^{\text{th}}$ percentiles was computed for each subject, followed by the sample mean and SD.

$$\text{MAPE (\%)} = \frac{\sum_{i=1}^{n} 100 \cdot \frac{|PET_{CAR-RiDR} - PET_{CT}|_i}{(PET_{CT})_i}}{\sum_{i=1}^{n} i} \tag{5.5}$$

In addition to error maps, voxel-wise correlations between CT-based reconstructions and MR-based reconstructions were also computed. The $PET_{CT}$ signal intensities of brain voxels were plotted against the corresponding $PET_{CAR\text{-}RiDR}$ voxel intensities for each subject. Linear regressions were performed, and the slopes of the resulting "lines-of-best-fit" were used to further characterize the accuracy of the proposed method.

The ICBM 2009c nonlinear symmetric brain atlas (McConnell Brain Imaging Centre, Montreal, Canada), which contains detailed anatomical labeling, was chosen to define several regions-of-interest (ROIs) for regional PET error analysis. This atlas was aligned to subject PET images through a series of nonlinear (ANTS, PICSL, Philadelphia, PA) and linear (FSL Toolbox, FMRIB, Oxford, United Kingdom) registrations using patient T1-MR images. Once aligned, 24 brain regions (Figure 5.7) were selected and the MAPE calculations were repeated for these ROIs.

In order to visualize the directionality of the errors (under vs. overestimation) in these ROIs, the mean percent-error (MPE) was computed for all ROIs (Equation 5.6) in each subject, followed by the sample mean across subjects. Box-and-whisker plots were generated for these sample mean data for each ROI, and outliers were defined as subjects with errors larger in magnitude than 1.5 times the interquartile ($75^{th} - 25^{th}$ percentile) range (IQR).

$$\text{MPE (\%)} = \frac{\sum_{i=1}^{n} 100 \cdot \frac{(PET_{CAR-RiDR} - PET_{CT})_i}{(PET_{CT})_i}}{\sum_{i=1}^{n} i} \tag{5.6}$$

2.6.5 Statistical Analysis

The statistical comparisons between results were analyzed using two-tailed paired Student's t-tests. A result was considered to be statistically significant when the p-value of the t-test was less than 0.05.

## 5.3 Results

### 5.3.1 Segmentation of Bone and Air

Mean Dice coefficients ($\pm$SD) across subjects for the RiDR method were 0.75 ($\pm$0.05) for bone and 0.60 ($\pm$0.08) for air. The corresponding values for the vUTE method were 0.36 ($\pm$0.09) for bone and 0.52 ($\pm$0.07) for air. The Dice coefficients for both bone ($p<10^{-6}$) and air ($p<10-6$) were significantly higher for the RiDR method compared to the vUTE method. Representative results for one subject (Figure 5.3) show good agreement between the proposed method and CT-based segmentation for both bone and air, wheras the vUTE method exhibits severe underestimation of bone and overestimation of air.
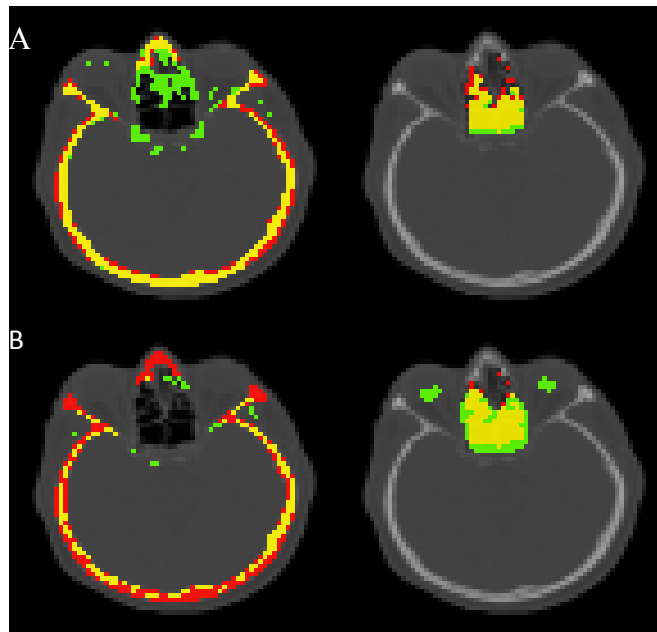


Figure 5.3: Representative segmentation results from one subject for the RiDR method (A) and vUTE method (B) overlaid on CT for bone (left) and air (right). True positives (yellow), false positives (green, overestimation), and false negatives (red, underestimation) are shown.

*5.3.2 Regression*

The mean and SD values across all subjects of the five parameters in the sigmoid model derived for each subject are shown in Table 5.1. As can be seen from the low SDs exhibited by each of the five parameters, the parameters are highly consistent across subjects. The sample mean percent-error (±SD) in the estimation of CT-HU was 28.2% (±3.0) for the CAR method and 46.9% (±5.8) for the method employing constant CT-HU values ($p<10^{-6}$).

Table 5.1: Sigmoid Parameters

| Parameter | Mean | SD |
|-----------|--------|-------|
| A | 333.2 | 0.89 |
| B | 16.9 | 0.15 |
| C | 593.5 | 0.62 |
| D | 1851.8 | 18.18 |
| G | 0.083 | 0.002 |

*5.3.3 Attenuation Maps*
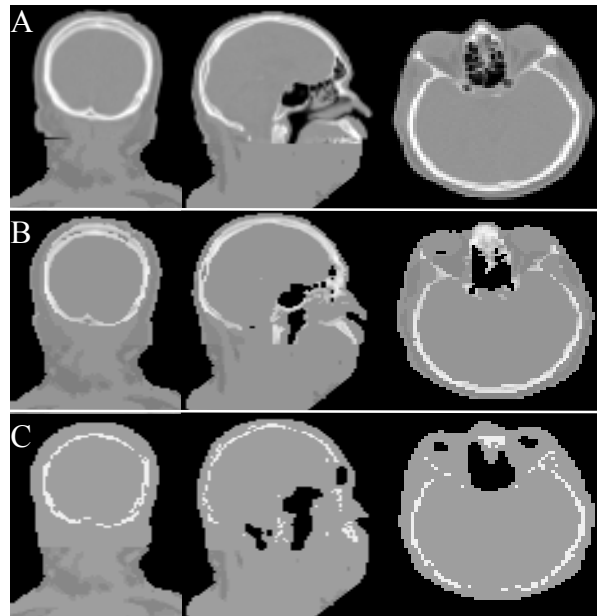


Figure 5.4: Sample slices from the $\mu_{CT}$ (A), $\mu_{CAR\text{-}RiDR}$ (B), and $\mu_{vUTE}$ (C) attenuation maps from one subject in three orientations.

Representative slices from the attenuation maps from one subject (Figure 5.4) provide qualitative confirmation of accurate segmentation of bone and air voxels in the $\mu_{CAR\text{-}RiDR}$ map compared to $\mu_{CT}$. By comparison, these regions are not as well-identified in the $\mu_{vUTE}$ map.

54

Visual inspection of the $\mu_{CAR-RiDR}$ map (Figure 5.4B) provides confirmation of the accurate representation of continuous bone LACs using the CAR conversion method while the $\mu_{vUTE}$ map does not account for these differences.

*5.3.4 Whole-brain PET Errors*
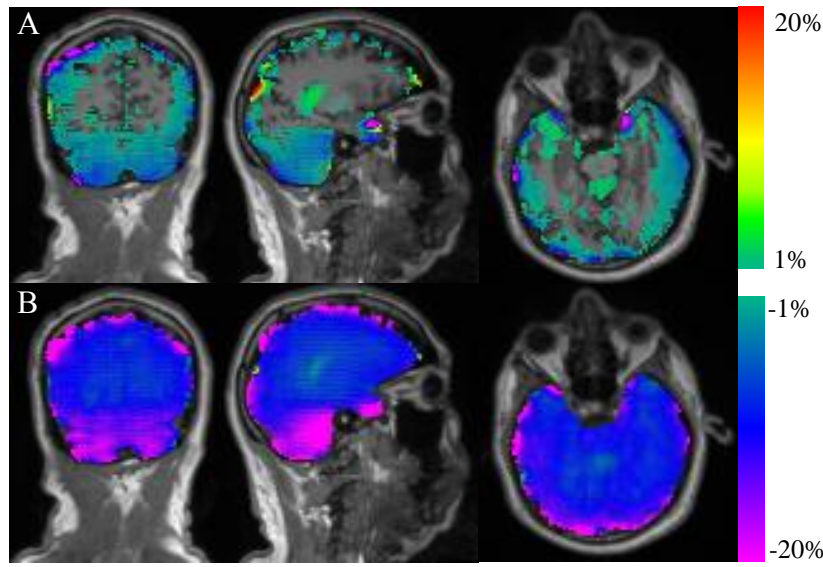


Figure 5.5: Representative slices from percent-error maps from one patient show drastically reduced errors across the brain in PET$_{CAR-RiDR}$ (A) compared to PET$_{vUTE}$ (B). Errors between ±1% are suppressed for visual clarity.

The whole-brain MAPEs (±SD) value across subjects relative to the PET$_{CT}$ reconstructions were 2.55% (±0.86) for the PET$_{CAR-RiDR}$ reconstructions and 12.25% (±2.09) for the PET$_{vUTE}$ reconstructions (p<10-6). The differences between the 95th and 5th percentile (±SD) error values across subjects in whole-brain were 9.89% (±4.22) for the PET$_{CAR-RiDR}$ reconstructions and 20.93% (±9.77) for the PET$_{vUTE}$ reconstructions (p<10-6). The proposed method produced favorable error characteristics across the brain as illustrated in Figure 5.5.

Figure 5.6 shows a scatter plot of PET$_{CT}$ vs. PET$_{CAR-RiDR}$ for a representative subject. As shown in Figure 5.6A, PET$_{CAR-RiDR}$ displays an almost one-to-one relationship with PET$_{CT}$, indicating a good correlation between the two methods. The mean slope (±SD) across subjects

of $PET_{CT}$ vs. $PET_{CAR\text{-}RiDR}$ was 0.98 (±0.03). As shown in Figure 5.6B, $PET_{vUTE}$ underestimates the true distribution, represented by by $PET_{CT}$.
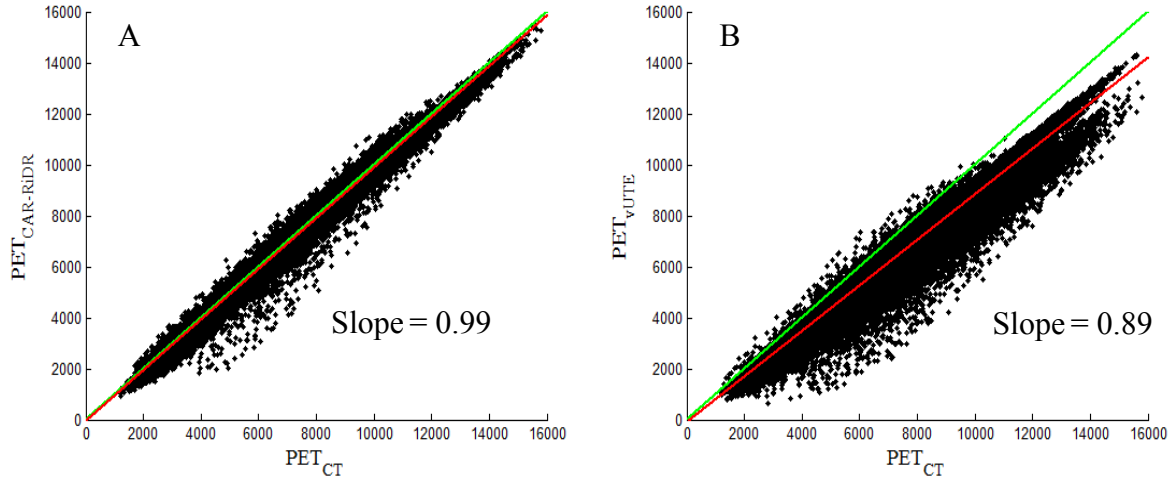


Figure 5.6: The lines-of-best-fit (red) displayed for a representative subject show that $PET_{CAR\text{-}RiDR}$ (A) approaches unity slope (green) when regressed with $PET_{CT}$ whereas $PET_{vUTE}$ (B) displays consistent underestimation.

*5.3.5 Regional PET Errors*

The results from ROI analysis of the mean MAPE values across subjects (Figure 5.6) are in good agreement with the results from the whole-brain analysis in Section 5.3.3. The regional MAPEs in the $PET_{CAR\text{-}RiDR}$ reconstructions ranged from 0.88 to 3.79% in the 24 ROIs studied. In contrast, the regional mean errors using the $PET_{vUTE}$ method ranged from 6.36 to 22.36% in the same ROIs. The $PET_{CAR\text{-}RiDR}$ reconstructions were overall more accurate than the $PET_{vUTE}$ reconstructions in all ROIs studied. The variation in errors across patients is also drastically reduced in the proposed method compared to the vUTE method.

**5.4 Discussion**

Two of the major challenges in MR-based attenuation correction in the head are proper identification of bone and air and accurate estimation of bone LACs. The proposed method CAR-RiDR, developed to address these challenges, consists of two components. The first component RiDR is a method for accurate bone/air segmentation based on intermediate images

derived from UTE and Dixon data. The second component CAR is a mechanism for the conversion of bone UTE data in the form of $R_2^*$ values to CT-HU values, which are subsequently translated to continuous PET LAC values.
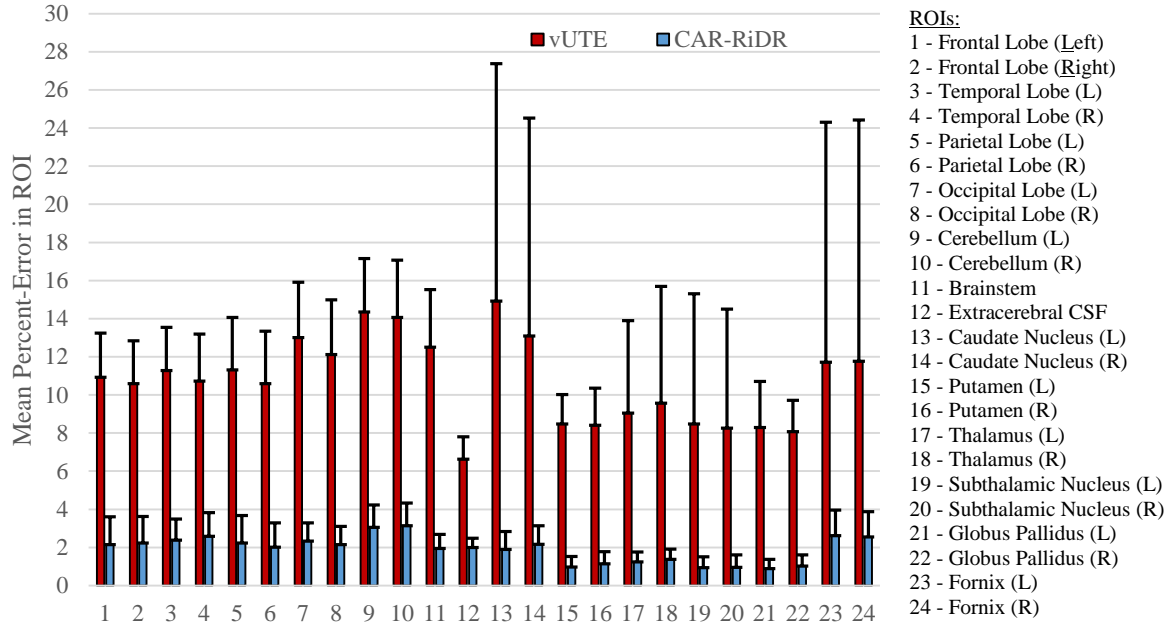


Figure 5.7: Mean percent-errors computed in a variety of brain region ROIs show that the proposed method results in lower local errors than the vUTE method in all ROIs tested. The standard deviations at each ROI (indicated by the error bars) are also much lower for the proposed method.

Segmentation-based methods for AC rely on accurate segmentation of MR images, the performance of which can be quantitatively measured using Dice coefficients. Based on the mean Dice coefficients reported in Section 5.3.1, the proposed RiDR segmentation method performs well in identifying both bone and air voxels. Qualitatively, visual overlap between CT-based segmentation and MR-based segmentations of bone and air (Figure 5.3) can be used to identify degree of misclassification. The RiDR method exhibits a high degree of similarity (yellow) with CT in regions of bone but overestimates the amount of bone (green) in sinus soft tissue. These errors may be due to susceptibility artifacts occurring near air-tissue interfaces, which result in abnormally high $R_2^*$ values and lead to classification errors. The RiDR method also exhibits a high degree of similarity (yellow) with CT in regions of air.

The RiDR segmentation method employs static thresholding of four intermediate images in order to arrive at classifications for bone, air, fat, and soft tissue. These thresholds were empirically selected to minimize misclassifications, and led to low Dice coefficient standard deviations (Section 5.3.1) for the RiDR method. Thresholding of MR images is not commonly used due to the sensitivity of voxel intensities to acquisition conditions, thereby making inter-subject comparison of intensities difficult. The RiDR method overcomes this limitation by basing its segmentation in part on normalized intermediate images. For air segmentation, iUTE images were normalized to the $99^{th}$ percentile value. For bone segmentation, normalization is achieved by virtue of $R_2^*$ being a physical parameter. While the intermediate images for fat and soft tissue were not normalized, good segmentations were still achieved with static thresholds. The advantage of static thresholds is they remove the need for operator involvement in the segmentation process and automate the RiDR segmentation component of the proposed method.

The CAR method employs a five-parameter sigmoid equation to convert measured patient $R_2^*$ values into estimated CT-HU values in bone. The parameters for this equation were computed from regression analysis of CT-HU and $R_2^*$ values from a population of subjects. Validation of this model, which was performed using a leave-one-out strategy, revealed little variation (Section 5.3.2) across subjects for each of the five parameters. Thus, the conversion equation governing the relationship between $R_2^*$ and CT values can remain static across patients. These conversion parameters can be computed offline from an existing population of subjects, thereby automating the conversion component of the proposed method. When used in combination with the static thresholds from the RiDR segmentation method, static conversion parameters result in complete automation of the CAR-RiDR method.

58

The proposed CAR-RiDR method is a hybrid MRAC method that combines the quickness and robustness of segmentation-based methods with the increased accuracy exhibited by atlas-based methods. It differs from existing segmentation-based methods by providing continuous-valued LACs for bone and differs from existing atlas-based methods by avoiding time-consuming variants of pattern recognition methods to estimate these LACs. The $R_2^*$ to CT-HU conversion can be pre-defined using population data. For a given subject, this conversion can be directly applied to the $R_2^*$ maps without the need for image registration. As a result, the total computation time is extremely short ($< 15$ sec). This reduction in computation time allows for better integration of attenuation correction into the PET/MRI clinical workflow.

The proposed CAR-RiDR method results in accurate PET reconstructions when evaluated against the gold standard CT-scaled method. Whole-brain (Figures 5 and 6) and regional analysis (Figure 5.7) of PET reconstruction errors demonstrates that the proposed method performs well across different brain regions and greatly outperforms the vUTE method in attenuation correction of the head. . A previous study by Burgos *et al*. demonstrated errors seen in the vUTE method, which uses a very similar VB18 WIP-UTE acquisition protocol, that are comparable to those seen in this study – a whole-brain error of 11.86% *(14)*. Burgos *et al*. employed a slightly different approach to computing whole-brain error than the method presented in this manuscript (MAPE). Recomputing error using their approach yields a whole-brain error of 2.44% for the CAR-RiDR method. Based on the whole-brain error results of Burgos *et al*. and those reported in this study, it is clear the proposed CAR-RiDR method produces much more accurate PET reconstructions than the vendor-provided VB18 UTE-AC method.

Direct comparisons between the accuracy of the proposed method and other methods in literature were not performed due to differences in data and in the reference method used for error computations. Errors for segmentation-based methods are typically computed against the "silver standard" *(9)* CT-segmented method, while atlas-based methods are generally compared to the gold standard. To generate the silver standard attenuation map, a CT image is segmented (as opposed to scaled), and the resulting segmentation is assigned a constant LAC value by tissue class, including bone. The true error (i.e. error when compared to the gold standard) for these methods is therefore unknown.

Recently, a few methods *(13, 15)* combining both atlas- and segmentation-based approaches have been presented. Poynton *et al*. *(16)* integrated an atlas-based tissue probability map into a previously presented segmentation-based method *(9)*, improving the accuracy compared to the segmentation-based method alone. However, the analysis in this study was performed against the aforementioned silver standard. Combining T1-MPRAGE and SPM atlas information, Izquierdo-Garcia *et al*. *(13)* have reported a MR based attenuation correction method that can achieve a good accuracy in PET AC (MAPE =3.9% in the whole brain) with a computation time of 30 minutes per attenuation map. Our proposed CAR-RiDR method produces comparable PET errors (MAPE = 2.6% in the whole brain) with a computation time of less than 15 seconds.

There are a few limitations to our study. First, UTE images (the basis for the $R_2^*$ maps used both for segmentation and for conversion to CT) suffer from susceptibility artifacts as well as noise issues. These artifacts and noise result in misclassifications of the soft tissue in the sinus regions (Figure 5.3A). Additionally, images used in this study were acquired mostly from normal subjects at one center using the same PET/MRI and PET/CT scanners. Further

evaluation will be needed to determine if differences in the acquisition system or presence of disease states with focal lesions affect the results achieved with the proposed method. The data used in this study were primarily from older subjects (mean age: 66 years ± 9.8). Thus, further validation of the proposed method in more diverse populations is needed. Incorporation of additional population demographics will allow multivariable regression analysis of $R_2^*$ and CT-HU values, which may reveal demographic-dependent variation of the conversion parameters. Finally, cerebellar regions display the highest ROI errors (median MPEs of -2 to -3%) across patients. Because of their spatial proximity to petrous bone, the cerebellar regions are more subject to bone/air misclassification. This is potentially problematic in clinical applications where PET signal in the cerebellum is used for normalization, resulting in propagation of error to the rest of the brain. Therefore, caution needs to be taken in such normalization.

To our knowledge, the proposed method is the first MR-based attenuation correction method to directly associate the MR relaxation rate $R_2^*$ with CT-HU in bone, providing continuous-valued attenuation coefficients for bone using only patient information. A previous study *(4)* examined a joint histogram of $R_2^*$ maps and co-registered CT images and noted a potential relationship for voxels with a CT value of greater than 100 Hounsfield units (HU), i.e. bone. However, until now, there have been no MR-based attenuation correction methods presented that estimate LAC values for bone based on $R_2^*$ values. The proposed method has been shown to be highly accurate, producing $< 3\%$ error in whole-brain. Moreover, our method greatly decreases the spatial variations of PET errors as evidenced by the reduction in the difference between the 95th and 5th percentiles of the PET errors (Section 5.3.4). In contrast to other studies of experimental MRAC methods reported in literature, the accuracy of the CAR-

RiDR method has been validated using data from a large number of subjects (n = 92). Based on the large dataset used, we can be confident that the results presented in this study are a good measure of the performance of the method.

**5.5 Conclusions**

In summary, we propose an MR-based attenuation correction method (CAR-RiDR) for use in quantitative PET neurological imaging. The CAR-RiDR method employs UTE and Dixon images and consists of two novel components: 1) accurate segmentation of air and bone using the inverse of the $UTE_1$ image and the $R_2^*$ image, respectively and 2) estimation of continuous LAC values for bone using a regression between $R_2^*$ and CT-HU. From our analysis, we conclude the proposed method closely approaches ($< 3\%$ whole-brain error) the gold standard CT-scaled method in PET reconstruction accuracy. Additionally, the required UTE images can be acquired quickly ($\sim 1.5$ min), and the attenuation maps can be computed rapidly ($< 15$ sec), allowing for ease of incorporation into the PET/MRI clinical work flow.

# REFERENCES

1. Juttukonda MR, Mersereau BG, Chen Y, et al. MR-based attenuation correction for PET/MRI neurological studies with continuous-valued attenuation coefficients for bone through a conversion from R2* to CT-hounsfield units. *Neuroimage*. 2015;112:160-168.

2. Keereman V, Fierens Y, Broux T, De Deene Y, Lonneux M, Vandenberghe S. MRI-based attenuation correction for PET/MRI using ultrashort echo time sequences. *J Nucl Med*. 2010;51:812-818.

3. Horch RA, Nyman JS, Gochberg DF, Dortch RD, Does MD. Characterization of 1H NMR signal in human cortical bone for magnetic resonance imaging. *Magn Reson Med*. 2010;64:680-687.

4. Delso G, Carl M, Wiesinger F, et al. Anatomic evaluation of 3-dimensional ultrashort-echo-time bone maps for PET/MR attenuation correction. *J Nucl Med*. 2014;55:780-785.

5. Gottschalk PG, Dunn JR. The five-parameter logistic: A characterization and comparison with the four-parameter logistic. *Anal Biochem*. 2005;343:54-65.

6. Bezrukov I, Mantlik F, Schmidt H, Scholkopf B, Pichler BJ. MR-based PET attenuation correction for PET/MR imaging. *Semin Nucl Med*. 2013;43:45-59.

7. Keereman V, Mollet P, Berker Y, Schulz V, Vandenberghe S. Challenges and current methods for attenuation correction in PET/MR. *MAGMA*. 2013;26:81-98.

8. Carney JP, Townsend DW, Rappoport V, Bendriem B. Method for transforming CT images for attenuation correction in PET/CT imaging. *Med Phys*. 2006;33:976-983.

9. Catana C, van der Kouwe A, Benner T, et al. Toward implementing an MRI-based PET attenuation-correction method for neurologic studies on the MR-PET brain prototype. *J Nucl Med*. 2010;51:1431-1438.

10. Linstrom P, Mallard W. NIST chemistry WebBook, NIST standard reference database number 69. Gaithersburg MD: National Institute of Standards and Technology; . Available from: http://webbook.nist.gov. Accessed November 26, 2014.

11. Martinez-Moller A, Souvatzoglou M, Delso G, et al. Tissue classification as a potential approach for attenuation correction in whole-body PET/MRI: Evaluation with PET/CT data. *J Nucl Med*. 2009;50:520-526.

12. Wagenknecht G, Kaiser HJ, Mottaghy FM, Herzog H. MRI for attenuation correction in PET: Methods and challenges. *MAGMA*. 2013;26:99-113.

13. Izquierdo-Garcia D, Hansen AE, Forster S, et al. An SPM8-based approach for attenuation correction combining segmentation and nonrigid template formation: Application to simultaneous PET/MR brain imaging. *J Nucl Med*. 2014;55:1825-1830.

14. Burgos N, Cardoso MJ, Thielemans K, et al. Attenuation correction synthesis for hybrid PET-MR scanners: Application to brain studies. *IEEE Trans Med Imaging*. 2014;33:2332-2341.

15. Johansson A, Karlsson M, Nyholm T. CT substitute derived from MRI sequences with ultrashort echo time. *Med Phys*. 2011;38:2708-2714.

16. Poynton CB, Chen KT, Chonde DB, et al. Probabilistic atlas-based segmentation of combined T1-weighted and DUTE MRI for calculation of head attenuation maps in integrated PET/MRI scanners. *Am J Nucl Med Mol Imaging*. 2014;4:160-171.

# CHAPTER 6: TESLA

## 6.1 Overview

The CAR-RiDR attenuation correction method presented in Chapter 5 possesses many favorable characteristics such as low errors in the whole-brain ($< 3$ %), rapid computation time ($< 15$ sec), and full automation *(1)*. However, there are certain limitations to this method (Section 5.4) that should be addressed.

First, segmentation of $R_2{}^*$ images results in major misclassifications in the sinus regions due to susceptibility effects near air-tissue interfaces. These artifacts occur near tissue boundaries where the magnetic susceptibility of the tissues varies greatly. Magnetic susceptibility represents the degree to which a particular tissue/material is magnetized in response to the **B₀** magnetic field imposed by the MRI scanner. In the sinus regions of the head, there are many locations where air and soft tissue, which possess vastly different magnetic susceptibilities, are adjacent. The result is lower-than-expected signal intensities in the soft tissue regions of the sinuses due to more rapid dephasing. The image acquired at the second echo time of the UTE sequence is more severely affected by this phenomenon than the image acquired at the first echo. Thus, the $R2^*$ values in these soft tissue regions are artificially elevated, resulting in a misclassification as bone.

The next limitation of the CAR-RiDR method is that images acquired at the first echo time in the DUTE sequence experience greater detrimental effects from eddy currents compared to images acquired at the second echo time. This is due to the acquisition of data during the ramp-up portion of the gradient waveforms (Chapter 3) and results in regions where

the signal is lower at the first echo time compared to the second. Therefore, the $R_2^*$ values computed by measuring the signal decay from the first to the second echo will be negative in these regions. This effect is especially detrimental in soft tissue regions. The CAR-RiDR method overcomes this by empirically scaling the first UTE image, but such a correction is approximate and the resulting $R_2^*$ values may not represent the true values. Furthermore, any change made to the UTE sequence by the vendor that alters the distribution of image intensities could require further manipulation of this scaling factor.

Third, $R_2^*$ images are very noisy and result in over-classification of many soft and adipose tissue regions as bone. A Dixon-based separation technique can be used to separately identify soft and adipose tissues for the purpose of refining the R2*-based segmentation (as is done in the CAR-RiDR method), but this requires an image acquisition with an additional sequence.

Finally, the heterogeneity of soft and adipose tissue LAC values has not been thoroughly addressed by any current method. In the brain, LAC differences between gray matter (GM), white matter (WM), and cerebrospinal fluid (CSF) have been assumed to be negligible and, therefore, not likely to affect the accuracy of attenuation correction if represented by a single LAC value. In the CAR-RiDR method, it was not possible to address the heterogeneity of soft tissue LACs because no relationship was observed between $R_2^*$ and CT-HU values in soft tissue. However, since photon attenuation is a function of both LAC values and the thickness of tissue (Chapter 2), the sheer amount of brain tissue present could introduce errors into the PET reconstruction if a homogeneous LAC distribution is assumed for all soft tissue types.

The goal of this study was to address these limitations of the CAR-RiDR method. The first aim was to streamline the image acquisition in order to acquire all necessary images using one sequence. This would simplify the image acquisition and reconstruction process, reducing the likelihood of operator error. The second aim was to improve the CAR-RiDR attenuation map processing method by better utilizing the new information provided by the sequence modifications. Specifically, priority was given to providing continuous-valued attenuation coefficients not just to bone but to adipose and soft tissues as well.

## 6.2 Materials and Methods

### 6.2.1 Modifications to UTE Sequence

Many approaches were examined when determining which sequence structure would be the optimal one for use in this application. First, an inversion recovery UTE (IR-UTE) sequence along with phase-sensitive reconstruction was considered. This sequence would allow for the separation of bone and adipose tissue by selectively nulling the adipose tissue using inversion recovery prior to RF excitation. However, the RF pulses needed to perform the magnetization inversion deposit large quantities of energy into the patient, requiring repetition times that are too long to be clinically feasible. Next, the structure of the UTE sequence was modified, to what is known as balanced steady-state free precession (bSSFP) due to the
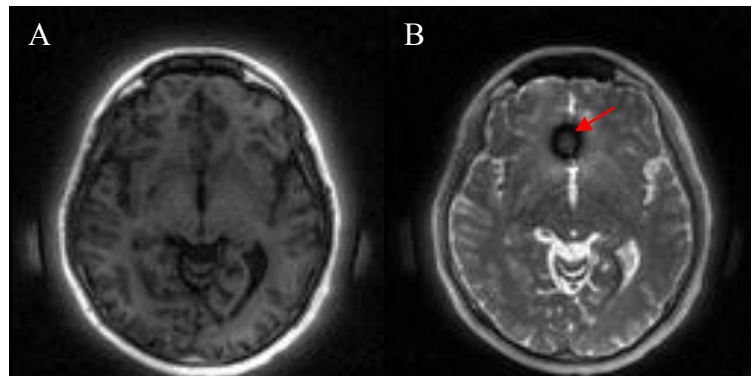


Figure 6.1: Images from spoiled GRE sequences (A) are not as affected by susceptibility artifacts (arrow) as images from bSSFP sequences (B).

reported insensitivity of this sequence to eddy current effects *(2)*. However, images from this sequence introduce additional problems such as severe susceptibility artifacts in regions of the brain that are not adjacent regions of air (Figure 6.1). Thus, the vendor-provided UTE sequence, which utilizes a spoiled GRE approach, was used as the basis for the proposed sequence.

The vendor-provided UTE sequence consists of a 3D radial GRE acquisition scheme with the following parameters: echo times (*TEs*) = 0.07 *ms*/2.46 *ms*, repetition time (*TR*) = 12 *ms*, flip angle (*FA*) = 10°, radial spokes (*Kr*) = 25,000. While these sequence parameters are the ones used to acquire images in the CAR-RiDR method, they may not be optimal for obtaining the information needed for every MRAC method. In this study, we determine the optimal values for these parameters in order to acquire the most appropriate images for developing accurate attenuation maps. This analysis was conducted using simulations of the signal equation (Equation 6.1) associated with the GRE sequence, where *C* is a scalar and $M_0$ is the magnitude of the equilibrium magnetization.

$$S(FA) = \frac{C * M_0 * \sin(FA) * \left(1 - e^{-\frac{TR}{T1}}\right) * e^{-\frac{TE}{T2^*}}}{1 - e^{-\frac{TR}{T1}} * \cos(FA)} \tag{6.1}$$

The first parameter examined was the repetition time. The vendor-provided UTE sequence employs a TR of 12 *ms* which is much longer than the second echo time (2.46 ms) at which data is acquired. Reducing the TR allows for a shorter total acquisition time but also results in a decrease in MR signal. Through signal calculations using Equation 1, it was found that lowering the TR from 12 ms to 9 ms results in a reduction in signal of approximately

12.5% but allows for a 25% reduction in acquisition time. Therefore, the value for TR for the new sequence was reduced to 9 ms.
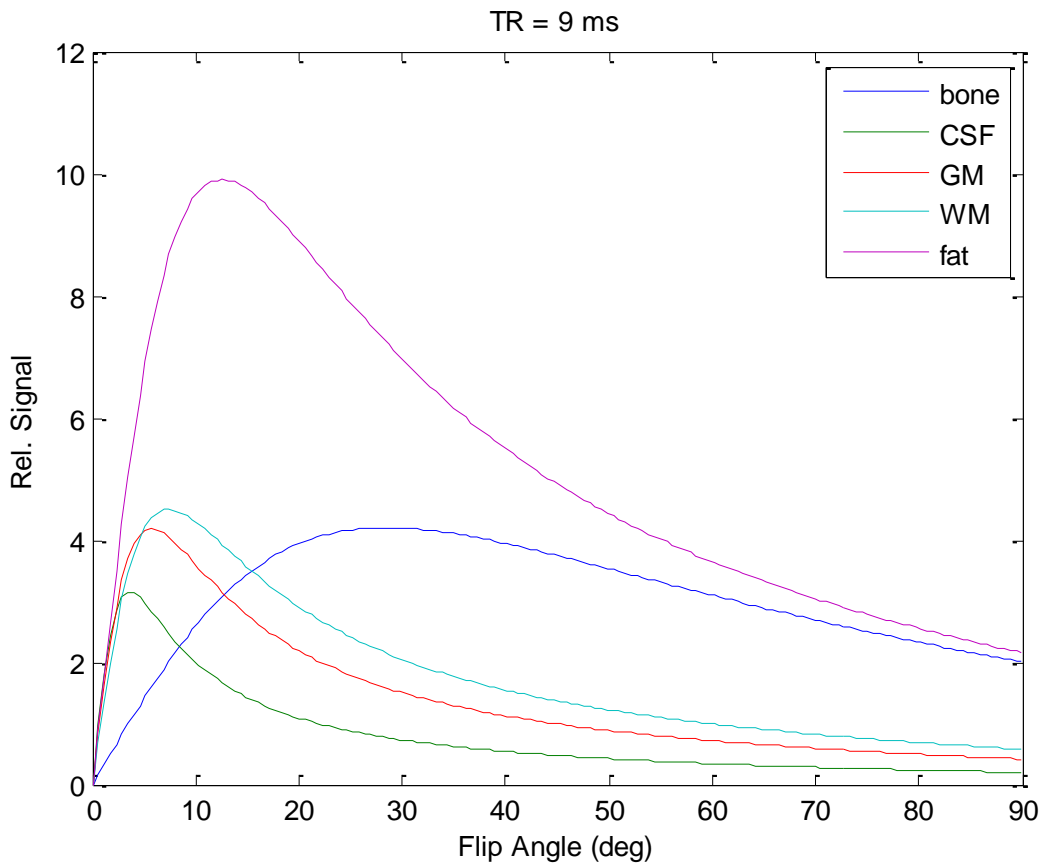


Figure 6.2: A plot of relative signal vs. flip angle is shown here for a TR = 9 ms.

The second parameter considered was the flip angle of the sequence. Since the image from the first echo time suffers greatly from eddy current effects, the $R_2^*$ values that are computed from the first to second echo are not quantitatively reliable. Therefore, utilizing the longitudinal relaxation rate $R_1$ may be more beneficial. Since $R_1$ represents the recovery of longitudinal magnetization through thermal exchange with the lattice (Chapter 3), it could be an indicator of tissue density since protons present in high density environments can more easily encounter atoms in the surrounding lattice. There are many methods that can be used to compute $R_1$ including inversion recovery and saturation recovery approaches. The approach utilized in this study was a variable flip angle (VFA) approach where images are acquired at

two different flip angles keeping all other parameters constant. Since the gradient structure of the two acquisitions should be identical, the differences in eddy current effects across the two images should be minimal. Therefore, the computation of $R_1$ should be more quantitatively reliable than the computation of $R_2$*.

Theoretically, any two (or more) flip angles may be chosen for the computation of $R_1$. This flexibility was strategically utilized to optimize another component from the CAR-RiDR processing method. Previously, the reciprocal of the $UTE_1$ image was used to identify regions of air. However, the threshold was carefully chosen in order to avoid selecting CSF and bone voxels, which also display low signal intensities in the $UTE_1$ image due to the flip angle of the sequence used (FA = 10°). GRE signal simulations were used once again to determine whether a better separation of air from CSF and bone would be possible if the flip angles are strategically chosen. Using the results of the simulation (Figure 6.2), it was determined that flip angles of 3° and 25° would be optimal for this purpose. At a flip angle of 3°, CSF exhibits high signal, whereas bone exhibits low signal; the opposite is true at a flip angle of 25°. Meanwhile, regions of air should exhibit low signal in images acquired using both flip angles. Therefore, the flip angles chosen for the sequence were 3° and 25°.

The third parameter examined was the second echo time ($TE_2$). Currently, the value chosen for $TE_2$ causes signals from fat and water protons, which have slightly different Larmor frequencies, to be in-phase during signal acquisition. Therefore, adipose tissue and soft tissue cannot be readily separated by examining signal differences between the images at $TE_1$ and $TE_2$. Increasing the value of $TE_2$ to 3.69 *ms* allows for the acquisition of signal at a time when fat and water signals are 180° out-of-phase. A two-point Dixon technique could then be used

on these images, eliminating the need for images from a separate Dixon acquisition. For this reason, the value of $TE_2$ was raised to 3.69 ms.

The last parameter that was examined was the number of radial lines acquired. Currently, 25,000 k-space lines are acquired in a multi-shot (multiple lines per RF excitation) approach that requires an acquisition time of 1 min and 40 sec. Thus far, the proposed sequence requires two acquisitions of the UTE sequence (one at each flip angle) and does not utilize a multi-shot approach. Therefore, it would be advantageous to reduce the number of radial lines acquired in order to minimize the total acquisition time. The number of radial lines chosen (Kr = 13,000) is approximately half of the original number and provides comparable image quality with minimal blurring effects (Figure 6.3).
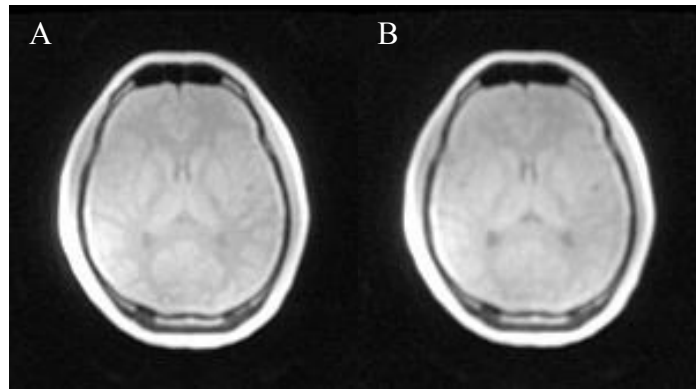


Figure 6.3: The image on the left was acquired with 25,000 radial lines (A) while the image on the right was acquired with 13,000 k-space lines.

The proposed sequence (dubbed DUFA for Dual-echo UTE with variable Flip Angles) acquires data according to the following parameters: echo times (TEs) = 0.07 *ms*/3.69 *ms*, repetition time (TR) = 9 *ms*, flip angles (FA) = 5°/25°, radial lines (Kr) = 13,000. The total acquisition time is 3 min 54 sec.

### 6.2.2 Data Acquisition

Imaging data were acquired from subjects enrolled in an Alzheimer's dementia study at Washington University Hospitals (St. Louis, MO). PET, MRI, and CT datasets were

prospectively obtained from 36 patients (mean age [range]: 75 yrs [59 89]; 14 females) using an IRB-approved protocol and with informed consent. $^{18}$F-Florbetapir (Amyvid [Avid], Eli Lilly, Indianapolis, IN) PET images and MR images were acquired on a hybrid PET/MR system (Biograph mMR, Siemens, Erlangen, Germany). Patients were injected with approximately 370 MBq of the $^{18}$F-Florbetapir tracer, and PET acquisitions were begun either immediately after injection or 50 minutes after injection. Patients did not have any comorbidities that could interfere with testing, and did not receive any other PET injections within 24 hours. The enrollment exclusion criteria included contraindications to PET, PET/CT or PET/MR (e.g. electronic medical devices, inability to lie still for long periods), known claustrophobia, pregnant or breast-feeding.

T1-weighted MR (MPRAGE) images were acquired using an MPRAGE sequence with the following imaging parameters: Repetition Time (TR)/Echo Time (TE) = 2300/2.95 $ms$, Inversion Time (TI) = 900 $ms$, flip angle = 9°, number of partitions=176, field-of-view (FOV) = 256 mm$^2$ and a voxel size of 1×1×1.2 mm$^3$. The vendor-provided UTE (vUTE) MRAC images were acquired with the following imaging parameters: TR/TE$_1$/TE$_2$ = 12/0.07/2.46 $ms$, flip angle = 10°, field-of-view (FOV) = 300 mm$^2$ and a voxel size of 1.56×1.56×1.56 mm$^3$. The attenuation maps generated from these images were also utilized in the study. The proposed DUFA sequence was used to acquire UTE images (DUFA-UTE) with the following parameters: TR/TE$_1$/TE$_2$ = 9/0.07/3.69 $ms$, flip angles = 3°/25°, FOV = 300 mm$^2$ and a voxel size of 1.56x1.561.56 mm$^3$. These images will be referred to hereby with the following naming convention: FA$_{Flip Angle}$UTE$_{Echo Number}$.

CT images of the head were acquired separately using a PET/CT system (Biograph 40 PET/CT, Siemens, Erlangen, Germany) with 120 keV, 25 effective mAs, a voxel size of

0.59×0.59×3.0, and a matrix size of 512×512×74. Images acquired using the DUFA-UTE sequence suffered from poor signal in some regions in the anterior portion of the head such as the mouth and neck. This was due to the RF receiver coil in this area not being switched on prior to acquisition. Furthermore, a pre-scan calibration that is typically done to correct for different RF coil sensitivities was not performed. As a result, the acquired images (Figure 6.4) displayed signal degradation in the affected regions that hindered the accurate computation of $R_1$ as well as the Dixon decomposition. In order to correct for this degradation, two sets of images were acquired on a template subject using the DUFA-UTE sequence. The first set was acquired using the same RF coil set-up as the clinical data with no pre-scan normalization. The second set was acquired using an identical RF coil set-up with pre-scan normalization. For each of the four images acquired using the DUFA-UTE sequence, a ratio image was computed between the second set of images to the first set. The DUFA-UTE images of each patient from the clinical data were then multiplied by the corresponding ratio image derived from the template subject. This correction was performed prior to any processing of patient images.
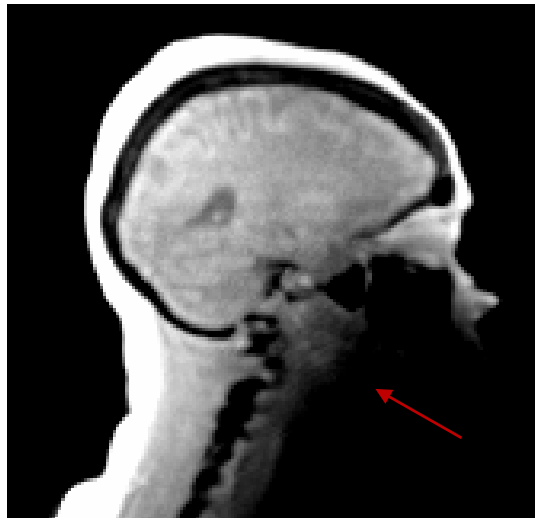


Figure 6.4: Regions in images acquired using the DUFA-UTE sequence displayed signal loss in anterior portions of the head.

All images were de-identified before being transferred offline for image analysis. For each subject, the MPRAGE and CT images were rigidly registered to the corresponding $FA_3UTE_1$ image via a rigid body transformation with mutual information using the 'FLIRT' command in the FSL toolbox (FMRIB, Oxford, United Kingdom).

*6.2.3 Identification of Tissues*

A mask of the head and neck region was formed using a threshold of the $FA_{25}UTE_1$ image, followed by connected component analysis and morphological operations to isolate the subject from background. The four images produced ($FA_3UTE_1$, $FA_3UTE_2$, $FA_{25}UTE_1$, $FA_{25}UTE_2$) from the DUFA sequence were then used strategically to produce intermediate images for the segmentation of bone, air, brain tissue, soft tissue and adipose tissue.
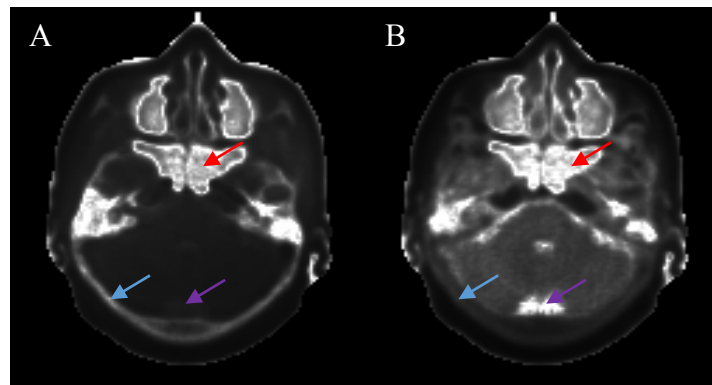


Figure 6.5: The iUTE3 image (A) displays large intensities in areas of bone (blue) and air (red), while the iUTE25 image (B) displays large intensities in regions of csf (purple) and air (red).

*Air*. In the $FA_3UTE_1$ images, bone and air appear alike, and in the $FA_{25}UTE_1$ images, CSF and air appear alike. The multiplicative inverse of these images, $iUTE_3$ and $iUTE_{25}$ respectively, were computed and normalized to their respective 99th percentile values. Initially, a simple threshold ($iUTE_3$ cutoff = 0.2; $iUTE_{25}$ cutoff = 0.4) was applied to each iUTE image to separately segment air. Next, the intersection of the classifications for air from each flip

angle was taken to produce the final classification for air. The iUTE images from each flip angle are displayed in Figure 6.5.

*Bone*. An estimate of the longitudinal relaxation rate $R_1$ was computed using a linear fit of the signal acquired in the $UTE_1$ images at two different flip angles (Equation 6.2).

$$Y = e^{\frac{-TR}{T1}} * X + M_0 * \left(1 - e^{\frac{-TR}{T1}}\right); \quad X = \frac{S}{\tan(FA)}, Y = \frac{S}{\sin(FA)} \tag{6.2}$$

An estimate of the transverse relaxation rate $R_2^*$ was also computed using the $FA_{25}UTE_1$ and $FA_{25}UTE_2$ images acquired using a flip angle of 25° as previously described *(1)* but without the need for empirical scaling of the $UTE_1$ image. Bone tissue exhibits faster longitudinal magnetization recovery and faster transverse magnetization decay compared to other biological tissues, as seen in Figure 6.6. This allows for the $R_1$ (cutoff = 7 s$^{-1}$) and $R_2^*$ (cutoff = 200 s$^{-1}$) images to be thresholded independently for the identification of bone. The intersection of these thresholds was then used to produce the final classification for bone.
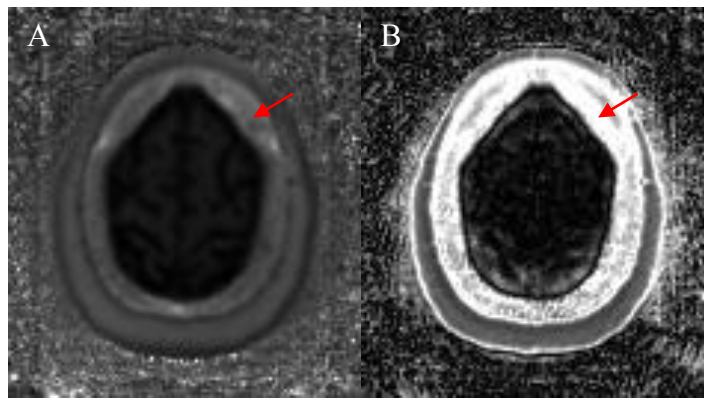


Figure 6.6: The R1 image (A) and the R2$^*$ image (B) display large intensities in areas of bone (red).

*Brain tissue*. Brain tissues are difficult to distinguish using $R_2^*$ since there are minimal differences in transverse decay rates between the tissues. However, $R_1$ can be readily used to separate GM, WM, and CSF. Empirically determined thresholds of $R_1$ were used to separate CSF (0 s$^{-1}$ < $R_1$ < 1.25 s$^{-1}$), GM (1.25 s$^{-1}$ < $R_1$ < 2.25 s$^{-1}$), and WM (2.25 s$^{-1}$ < $R_1$ < 4.5 s$^{-1}$).

Voxels between $R_1 = 4.5 \text{ s}^{-1}$ and $R_1 = 7 \text{ s}^{-1}$ were classified as general soft tissue. Sample results from this segmentation are shown in Figure 6.7A.
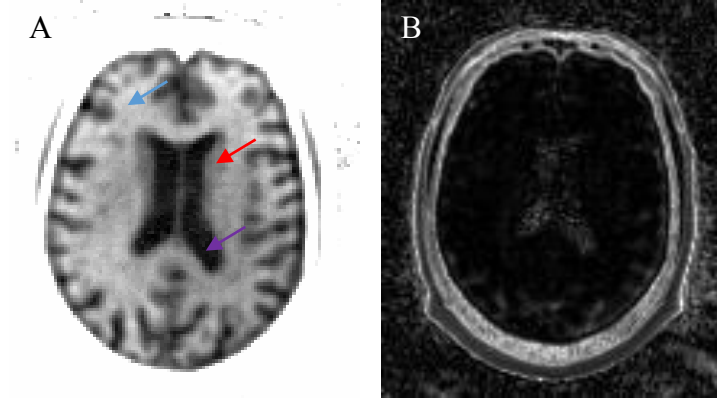


Figure 6.7: The R1 image (A) enables good separation of GM (red), WM (blue), and CSF (purple) while the R2* image (B) shows minimal contrast between these tissues.

*Adipose tissue.* Adipose tissue segmentation was performed in two stages. First, potential regions were identified using a simple threshold (cutoff $= 7 \text{ s}^{-1}$) of the $R_1$ image. Next, a Dixon decomposition was used to refine the initial segmentation. Intermediate images were computed from the $UTE_1$ (in-phase) and $UTE_2$ (opposed-phase) images acquired using both flip angles (Equation 6.3). Sample adipose tissue intermediate images are displayed in Figure 6.8 for a representative subject.

$$\text{Dixon}_1 = \frac{FA_3UTE_1 - FA_3UTE_2}{2}; \ \text{Dixon}_2 = \frac{FA_{25}UTE_1 - FA_{25}UTE_2}{2};$$

$$\text{Dixon}_3 = \frac{FA_{25}UTE_1 + FA_{25}UTE_2}{2}$$

(6.3)

The segmentation of adipose tissue from $R_1$ was then refined by combining the thresholds of each intermediate Dixon image (Equation 6.4).

$$\text{Adipose} = [(\text{Dixon}_1 > 150) \cap (\text{Dixon}_2 > 500)] \cup (\text{Dixon}_3 > 1000)$$

(6.4)
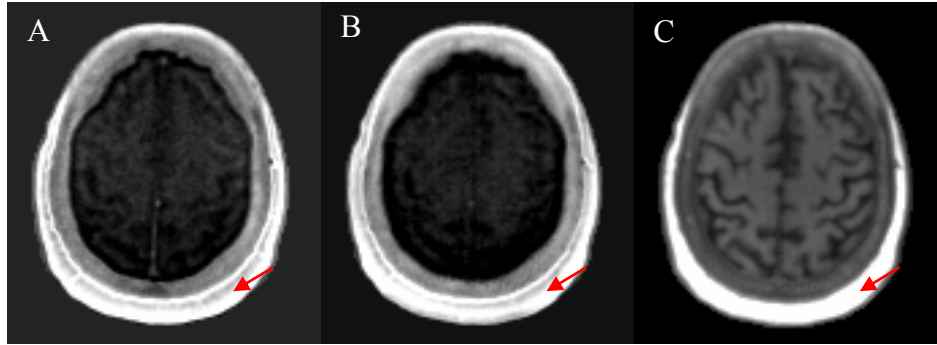
Figure 6.8: The Dixon$_1$ (A), Dixon$_2$ (B), and Dixon$_3$ (C) images allow for the refinement of adipose tissue (red) segmentation.

Any voxels in the head mask that were not classified as bone, air, brain, or adipose tissue, were assigned a general soft tissue classification. When segmentations overlapped, air classifications were given first priority over all other tissues. In addition, in cases of overlap between adipose tissue and bone, adipose tissue classification was prioritized.

*6.2.4 Assignment of LAC values*
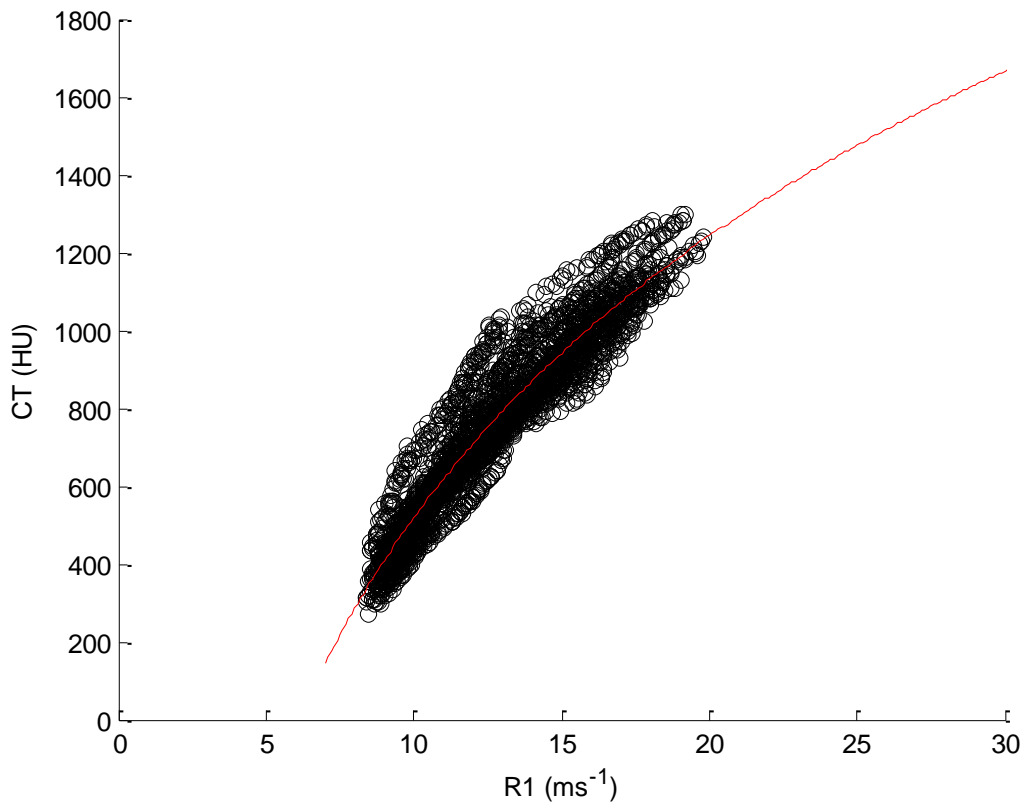


Figure 6.9: The scatter plot of mean R1 values vs. CT-HU values in bone tissue shows a logarithmic relationship.

It has long been assumed that MR signals have no direct correlation with PET LAC values, but certain MR relaxation parameters may be used to estimate the corresponding attenuation coefficients. Previously, $R_2^*$ has been used to estimate the LAC values of bone *(1, 3)*. However, no attempts have been made thus far to produce continuous-valued attenuation coefficients for soft tissue and adipose tissue. Since $R_1$ is a measure of interaction of hydrogen protons with the surrounding lattice, we employ $R_1$ as a means to estimate density (as measured by CT- Hounsfield units) of bone as well as soft tissue and adipose tissue.
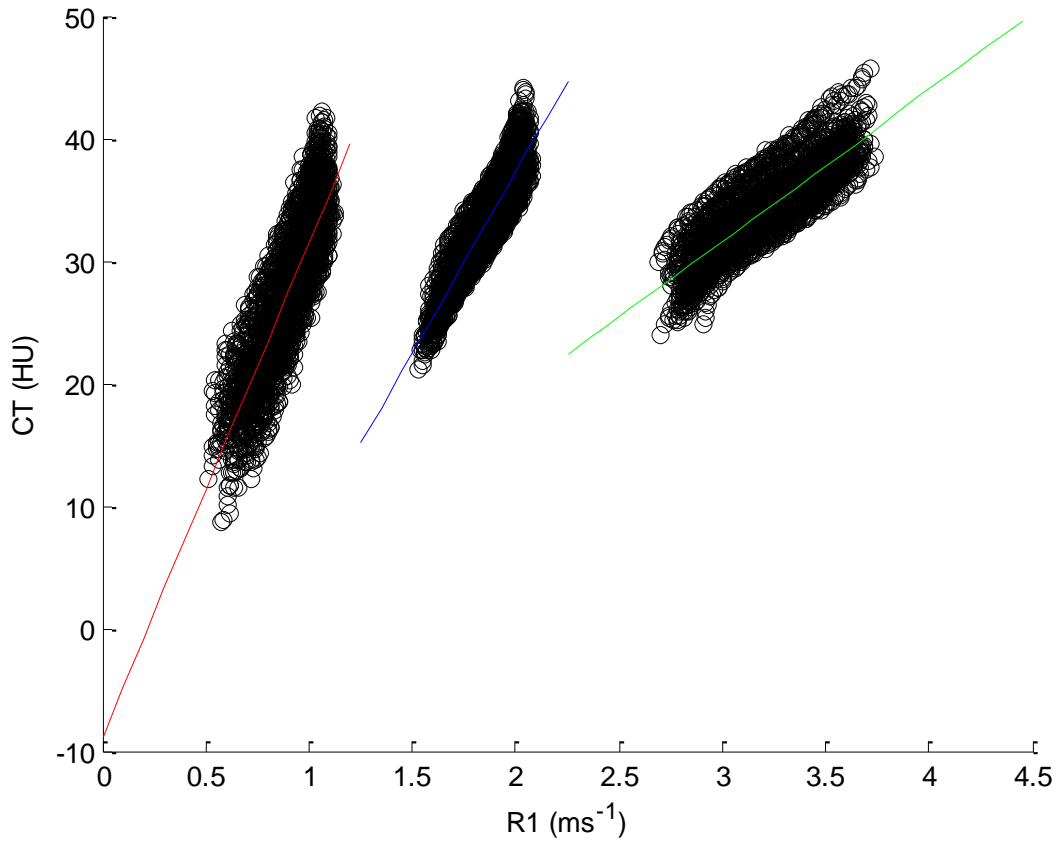


Figure 6.10: The scatter plot of mean R1 values vs. CT-HU values in brain tissue shows a piecewise linear relationship with separate conversions for CSF (red), GM (blue), and WM (green).

Regression analysis was performed between $R_1$ and CT-HU values for each subject using tissue masks formed by combined segmentations from each modality and is similar to the procedure described in Chapter 5. A brief description is provided here for convenience. A

spatially-mapped binning approach was followed for the regression. For each subject, the $R_1$ values of each tissue were sorted numerically and divided into 100 bins, each containing an equal number of voxels. For all voxels within an $R_1$ bin, the CT-HU values were matched through spatial correspondence from the aligned CT image. The mean $R_1$ and CT-HU values of each bin were plotted for all 100 bins for all patients using a leave-one-out approach. This procedure was repeated for the data a second time while sorting by the CT-HU values. The mean $R_1$ and CT-HU values derived from both methods were averaged and plotted for bins 10-90. Relationships between $R_1$ and CT-HU were discerned from these plots and statistical models were chosen empirically based on the plots. A linear model (Equation 6.4) was fit to the mean data for CSF, GM, WM, (Figure 6.10) and adipose tissue (Figure 6.11), while a logarithmic model (Equation 6.4) was fit to the mean data for bone (Figure 6.9). The fit parameters for each tissue are displayed in Table 6.1.

$$\text{Linear Fit: } CT = a*R1 + b; \quad \text{Log Fit: } CT = a*\log(R1) + b \tag{6.4}$$

Table 6.1: Representative fit parameters for one subject.

| Tissue | a | b |
|---|---|---|
| Cerebrospinal Fluid | 40.35 | -8.78 |
| Gray Matter | 29.60 | -21.9 |
| White Matter | 12.36 | -5.48 |
| Adipose Tissue | 3.48 | -99.89 |
| Bone | 1045.4 | -1888 |

Voxels belonging to the general soft tissue class were simply assigned a constant value of 42 HU. After the estimation of the CT values for each tissue using Eq. 4, both the actual CT

images and the pseudo-CTs produced from the R1 regression were scaled to PET LAC values according to a previously established procedure used in PET/CT systems (Equation 6.5).

$$\text{Below 50 HU: } \mu = 9.6 \times 10^{-5} \cdot (\text{HU} + 1000) \, \text{cm}^{-1}$$

$$\text{Above 50 HU: } \mu = 5.1 \times 10^{-5} \cdot (\text{HU} + 1000) + 4.71 \times 10^{-2} \, \text{cm}^{-1}$$

(6.5)

This MRAC method was dubbed the $T_1$-Enhanced Segmentation and assignment of Linear Attenuation coefficients (TESLA).
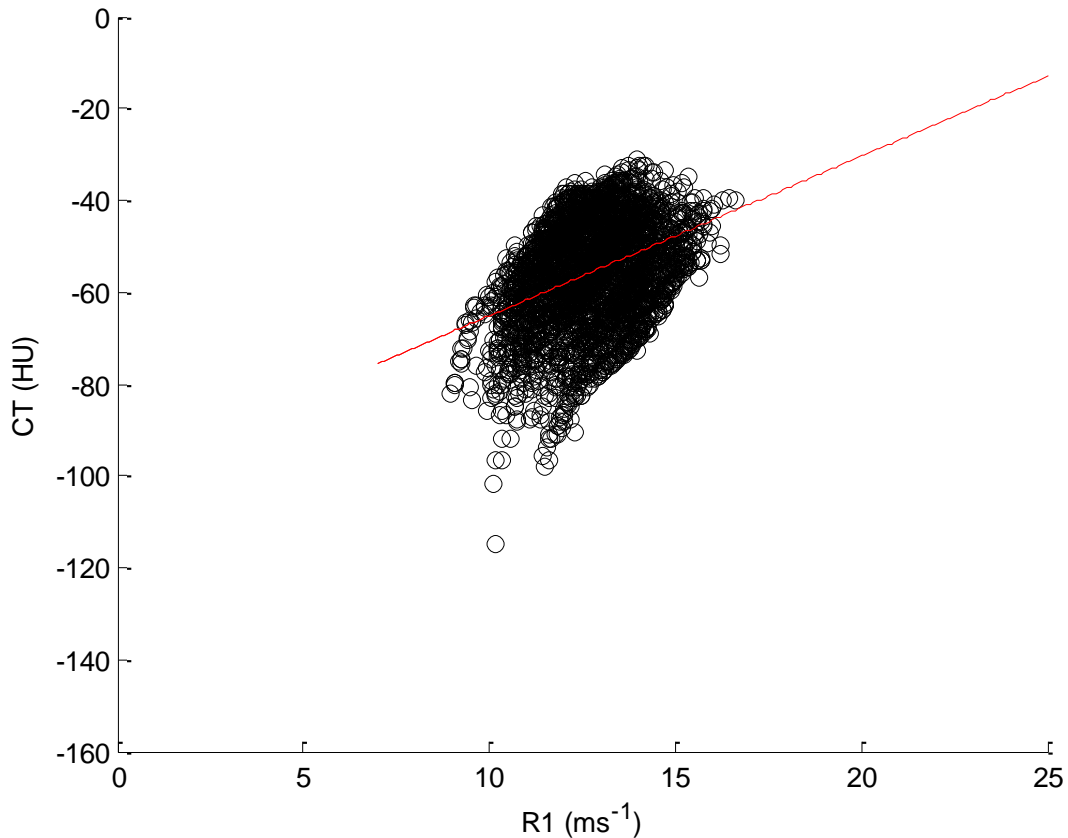


Figure 6.11: The scatter plot of mean R1 values vs. CT-HU values in adipose tissue shows a weak linear relationship.

*6.2.5 PET Image Formation*

The vendor-provided e7Tools program was used to reconstruct PET data present either in raw list-mode or raw sinogram formats. For 28 out of 36 subjects, reconstructions were

performed using the CT-based map ($\mu_{CT}$), the map from the TESLA method ($\mu_{TESLA}$), the map from the CAR-RiDR method ($\mu_{CAR\text{-}RiDR}$), and the vendor-provided attenuation map ($\mu_{vUTE}$). The vendor-provided map was acquired from the scanner and utilized the VB20 version of the UTE sequence and attenuation map processing protocol. PET images were reconstructed using an ordered subset expectations maximization (OSEM) algorithm with 3 iterations and 21 subsets to a standard clinical voxel size of 2.09 x 2.09 x 2.03 mm$^3$ and image size of 344 x 344 x 127. PET data from 8 of the remaining subjects was not reconstructed either due to issues with the compatibility of the attenuation map header information or due to image registration problems.

PET and UTE-MR data for all subjects were acquired from a full head and neck FOV. The CT images, however, had inadequate coverage of the neck region. This discrepancy was addressed by replacing affected slices in the CT-based map with slices from the vendor-provided UTE-based attenuation map, which provides full coverage of the head and neck. This step was also performed in the map derived from the TESLA and CAR-RiDR methods for the sake of fair comparison, but is not required as the DUFA sequence also provides full coverage of the head and neck region.

*6.2.6 Data Analysis*

*PET Image Formation*. Percent error maps were computed for the PET images reconstructed using the TESLA method (PET$_{TESLA}$), the CAR-RiDR method (PET$_{CAR\text{-}RiDR}$), and the vendor-provided method (PET$_{vUTE}$) against the PET images reconstructed using the CT-based method (PET$_{CT}$). The mean absolute percent-error (MAPE) was computed (Equation 6.4) in the whole-brain as well as in 24 ROIs identified using the ICBM 2009c nonlinear symmetric brain atlas (McConnell Brain Imaging Centre, Montreal, Canada). This atlas was

first aligned to subject MPRAGE images using the ANTS software package (PICSL, Philadelphia, PA). The atlas in MR-space was then aligned to PET images using the FSL Toolbox (FMRIB, Oxford, United Kingdom) using MPRAGE images that were transformed to PET space as the target.

$$\text{MAPE (\%)} = \frac{\sum_{i=1}^{n} 100 \cdot \frac{|PET_{CAR-RiDR} - PET_{CT}|_i}{(PET_{CT})_i}}{\sum_{i=1}^{n} i} \quad , n = \text{\# of voxels} \tag{6.4}$$

*Statistics*. Statistical analysis of the proposed method's accuracy in LAC estimation and PET image reconstruction was conducted using two-tailed paired Student's t-tests with statistical significance indicated by p-values of less than 0.05.

## 6.3 Results

### 6.3.1 Tissue Segmentation
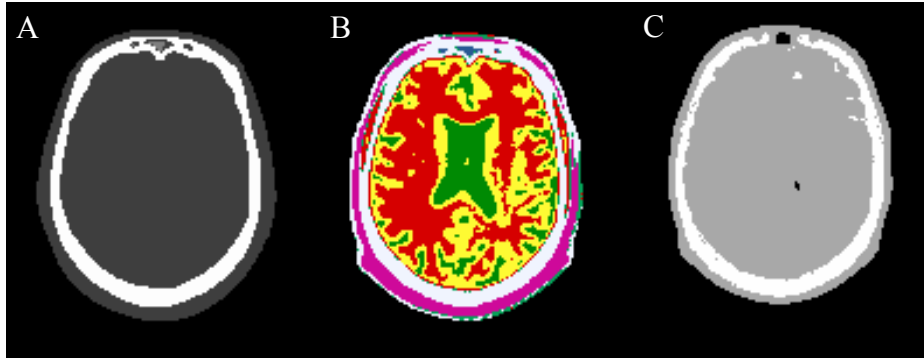


Figure 6.12: Segmentation results from one subject using a CT-based method (A), the TESLA method (B), and the vUTE method (C).

Representative results for one subject show good agreement between the TESLA method (Figure 6.12B) and CT-based segmentation (Figure 6.12 A) for regions of bone, whereas the vUTE method (Figure 6.12C) displays underestimation of bone near the sinuses and misclassification of some brain regions as bone.
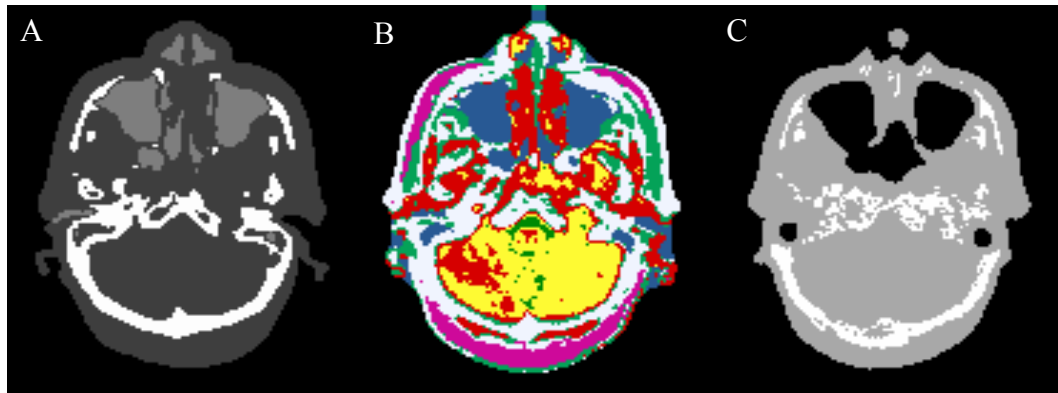


Figure 6.13: Segmentation results from one subject using a CT-based method (A), the TESLA method (B), and the vUTE method (C).

Representative results for one subject show good agreement between the TESLA method (Figure 6.13B) and CT-based segmentation (Figure 6.13 A) for regions of air as well, whereas the vUTE method (Figure 6.13C) displays significant overestimation of air in the maxillary sinus regions.
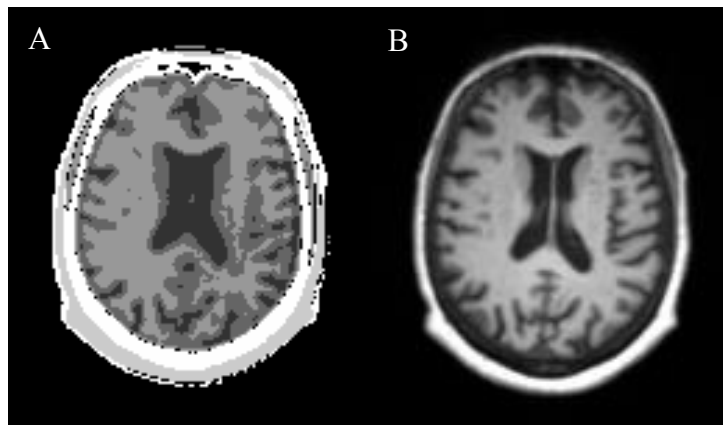


Figure 6.14: Segmentation results from one subject using the TESLA method (A) and the corresponding slice from the T1-MPRAGE image (B).

A visual comparison of the segmentation results from the TESLA method (Figure 6.14A) and the corresponding slice from the T1-MPRAGE image (Figure 6.14B), which provides good soft tissue contrast, shows that the TESLA method is capable of accurately identifying regions of GM, WM, and CSF.

*6.3.2 Regression*

Table 6.2: Mean ($\pm$ SD) of fit parameters across subjects.

| Tissue | a | b |
|---|---|---|
| Cerebrospinal Fluid | 40.55 ($\pm$ 0.22) | -8.89 ($\pm$ 0.23) |
| Gray Matter | 29.58 ($\pm$ 0.11) | -21.8 ($\pm$ 0.19) |
| White Matter | 12.39 ($\pm$ 0.09) | -5.56 ($\pm$ 0.28) |
| Adipose Tissue | 3.46 ($\pm$ 0.11) | -100 ($\pm$ 1.44) |
| Bone | 1049 ($\pm$ 6.01) | -1897 ($\pm$ 15.4) |

The mean ($\pm$SD) across subjects of the fit parameters in the regression model derived using a "leave-one-out" approach for each tissue are shown in Table 6.2. As can be seen from the low SDs, the parameters are highly consistent across subjects.

*6.3.3 Attenuation Maps*

Representative slices from the attenuation maps from one subject (Figure 6.14) provide further confirmation of accurate segmentation of bone and air in the $\mu_{TESLA}$ map compared to $\mu_{CT}$. By comparison, these regions are not as well-identified in the $\mu_{vUTE}$ map.

Visual inspection of the $\mu_{TESLA}$ map (Figure 6.15) provides confirmation of the accurate representation of continuous LACs for brain tissue using the TESLA method while the $\mu_{vUTE}$ map does not account for these differences.
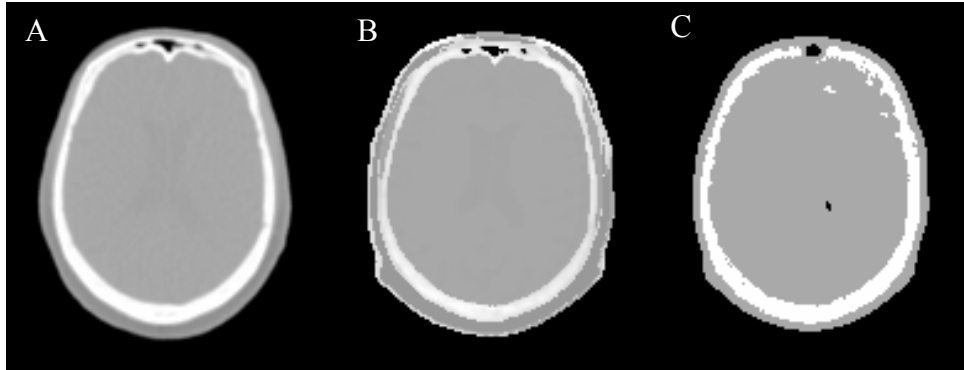


Figure 6.15: Sample attenuation maps shown from $\mu_{CT}$ (A), $\mu_{TESLA}$ (B), and $\mu_{vUTE}$ (C).

## 6.3.4 Whole-brain PET Errors
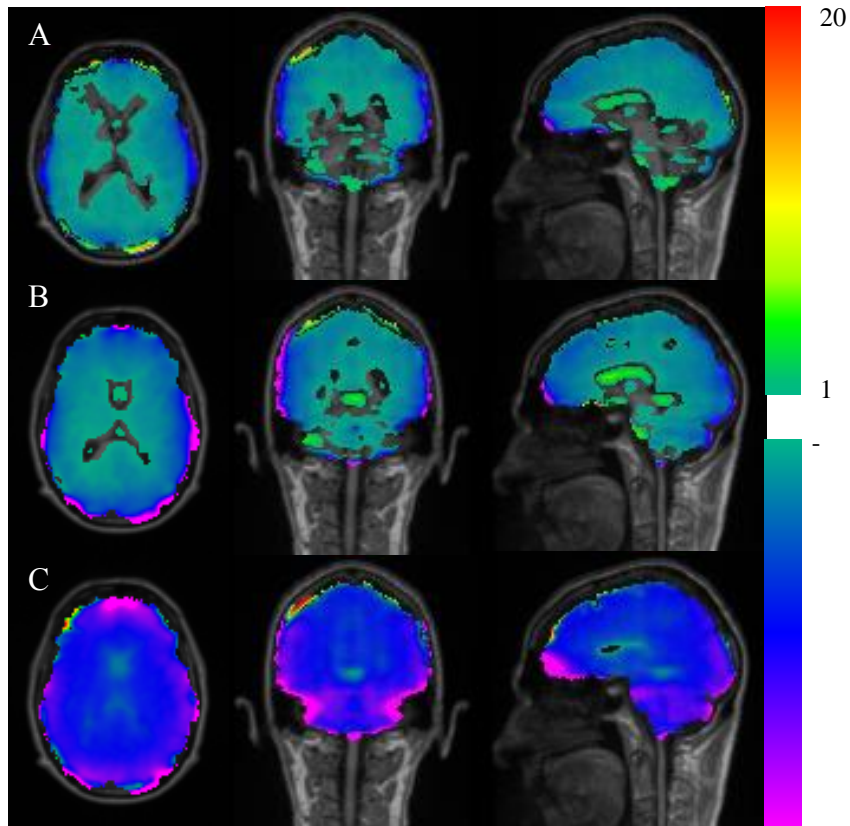


Figure 6.16: Sample percent-error maps for one subject for $PET_{TESLA}$ (A) and $PET_{CAR-RiDR}$ (B) and $PET_{vUTE}$ (C). Errors within +/- 1% are suppressed. Errors larger than +/- 20% were floored to +/- 20%.

The whole-brain MAPEs (±SD) value across subjects relative to the $PET_{CT}$ reconstructions were 2.53% (± 0.70) for the $PET_{TESLA}$ reconstructions, 2.59% (± 0.70) for the $PET_{CAR-RiDR}$ reconstructions, and 7.63% (± 1.71) for the $PET_{vUTE}$ reconstructions. The whole-brain MAPEs for the $PET_{TESLA}$ reconstructions were significantly different from the $PET_{vUTE}$ (p<0.01). The differences between the 95th and 5th percentile (±SD) error values across subjects in whole-brain were 8.51% (± 1.15) for the $PET_{TESLA}$ reconstructions, 10.19% (± 1.80) for the $PET_{CAR-RiDR}$ reconstructions, and 13.70% (± 2.48) for the $PET_{vUTE}$ reconstructions. The proposed TESLA method produces difference values that are significantly lower compared to both the CAR-RiDR and vUTE methods. Sample percent-error distributions for one subject are shown in Figure 6.16.
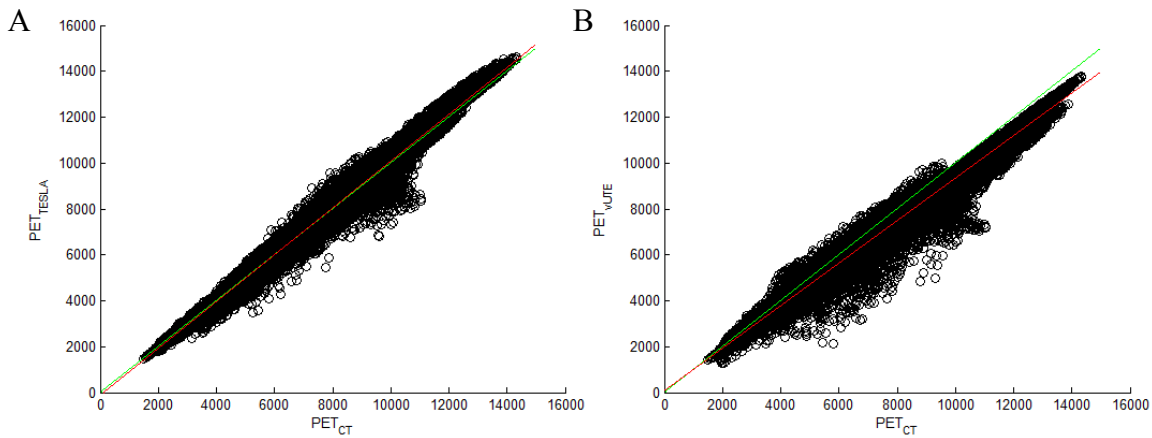


Figure 6.17: Voxel-wise scatter plots of $PET_{CT}$ vs. $PET_{TESLA}$ (A) and $PET_{CT}$ vs. $PET_{vUTE}$ (B) brain voxel intensities from a representative subject are shown here. The unity slope (green line) indicates a case with ideal correlation. The line of best bit for each plot is indicated by the red line.

Figure 6.17 shows a scatter plots of $PET_{CT}$ vs. $PET_{TESLA}$ and $PET_{CT}$ vs. $PET_{vUTE}$ for a representative subject. As shown in Figure 6.16A, $PET_{TESLA}$ displays an almost one-to-one relationship with $PET_{CT}$, indicating a good correlation between the two methods. This behavior was also observed for the CAR-RiDR method. The mean slope (±SD) across subjects was 0.99 (±0.01) for $PET_{CT}$ vs. $PET_{TESLA}$ and 0.99 (±0.01) for $PET_{CT}$ vs. $PET_{CAR-RiDR}$. In contrast

(Figure 6.17B), $PET_{vUTE}$ underestimates the true PET distribution, as represented by $PET_{CT}$. The mean slope ($\pm$SD) across subjects of $PET_{CT}$ vs. $PET_{TESLA}$ was 0.91 ($\pm$0.02).

### 6.3.5 Regional PET Errors

The results from ROI analysis of the mean MAPE values across subjects (Figure 6.18) are in good agreement with the results from the whole-brain analysis in Section 6.3.4. The regional MAPEs ranged from 0.89% to 2.63% in the $PET_{TESLA}$ reconstructions and 0.92% to 3.14% in the $PET_{CAR-RiDR}$ reconstructions in the 24 ROIs studied. In contrast, the regional mean errors using the $PET_{vUTE}$ method ranged from 2.39% to 9.87% in the same ROIs. The $PET_{TESLA}$ reconstructions were overall more accurate than the $PET_{vUTE}$ reconstructions in all ROIs studied. The variation in errors across patients is also drastically reduced in the TESLA method compared to the vUTE method. Comparing the TESLA method with the CAR-RiDR method, the differences in mean MAPEs were statistically significant ($p < 0.05$) in 9 out of the 24 ROIs



ROIs:
1 - Frontal Lobe (Left)
2 - Frontal Lobe (Right)
3 - Temporal Lobe (L)
4 - Temporal Lobe (R)
5 - Parietal Lobe (L)
6 - Parietal Lobe (R)
7 - Occipital Lobe (L)
8 - Occipital Lobe (R)
9 - Cerebellum (L)
10 - Cerebellum (R)
11 - Brainstem
12 - Extracerebral CSF
13 - Caudate Nucleus (L)
14 - Caudate Nucleus (R)
15 - Putamen (L)
16 - Putamen (R)
17 - Thalamus (L)
18 - Thalamus (R)
19 - Subthalamic Nucleus (L)
20 - Subthalamic Nucleus (R)
21 - Globus Pallidus (L)
22 - Globus Pallidus (R)
23 - Fornix (L)
24 - Fornix (R)

Figure 6.18: Mean absolute percent-errors for $PET_{vUTE}$ (blue), $PET_{CAR-RiDR}$ (red), and $PET_{TESLA}$ (orange) computed inside 24 ROIs. The error bars represent one standard deviation of the mean.

studied. The TESLA method outperformed the CAR-RiDR method in 8 of these regions which included several deep gray matter structures.

**6.4 Discussion**

The proposed method TESLA method improves on its predecessor, the CAR-RiDR method, by optimizing the UTE acquisition scheme and by modifying the processing protocol to better utilize the acquired images. The structure of the UTE sequence was modified by increasing the number of flip angles to 2, increasing the second echo time, reducing the TR, and reducing the number of k-space lines acquired. The processing protocol was modified by segmenting soft tissue CSF, GM, and WM in addition to bone, adipose tissue and soft tissue. Furthermore, a mechanism is provided for the conversion of $R_1$ values of bone, CSF, GM, WM, and adipose tissue to CT-HU values, which are subsequently translated to continuous PET LAC values.
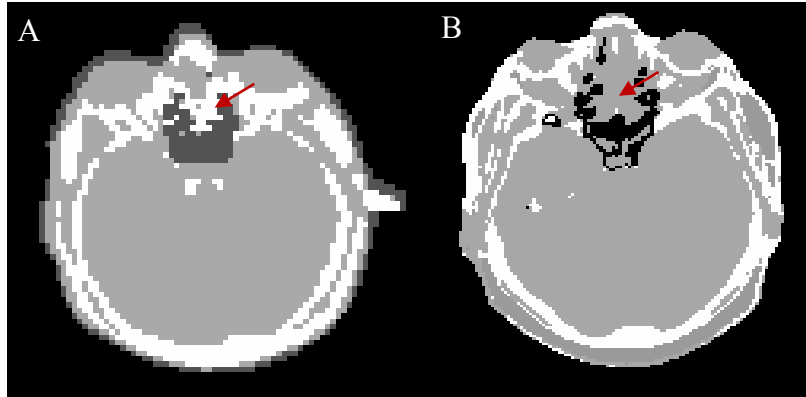


Figure 6.19: Over-classifications of bone in the soft tissue regions of the sinuses is reduced in the TESLA method (B) compared to the CAR-RiDR method (A).

The goal of this study was to address certain limitations of the $R_2^*$-based CAR-RiDR attenuation correction method presented in Chapter 5. First, the $R_2^*$ computed using the dual-echo UTE images, particularly $UTE_2$, suffer from susceptibility artifacts near air-tissue interfaces, resulting in major overestimations of bone in these regions due to artificially high values of $R_2^*$ in these regions (Figure 6.19A). Since both images used in the computation of

$R_1$ are acquired during the first echo of the UTE sequence, the differences in the effects of susceptibility artifacts are minimal. Thus, the segmentations derived using the TESLA method do not exhibit the misclassification of tissue near the air-tissue boundary as bone (Figure 6.19B).

Next, the $R_2^*$ computation was modified in order to roughly account for eddy current effects, which resulted in lower-than-expected image intensities. These eddy current effects are more prevalent in the $UTE_1$ image than in the $UTE_2$ image because image the acquisition of data at the first echo time is begun while the gradient is still being ramped up. This is not the case for the second echo time. The computation of $R_1$ is not as severely affected by this phenomenon because both images used are acquired during the first echo time with the same gradient waveforms. Thus, the effects of eddy currents are expected to be approximately the same across the $UTE_1$ images of both flip angles.

Third, the CAR-RiDR method employs a Dixon-MRI acquisition in addition to a UTE acquisition in order to perform a refinement for the the $R_2^*$-based bone segmentation. While this extra acquisition is fairly quick (18 sec), it requires an alignment of the Dixon images to the UTE images before the fat/water information can be utilized in the segmentation process. This alignment step requires time and introduces a source of error into the segmentation results. Furthermore, it has been reported that the fat/water separation from Dixon-VIBE sequence fails to properly segment fat and water tissues in about 8% of patients *(4)*. In these cases, the CAR-RiDR method cannot produce an accurate attenuation map since it relies on the Dixon-based refinement to correct overestimations of bone. The TESLA method overcomes these problems by computing the necessary fat/water information directly from the UTE images. Since the $UTE_1$ image is acquired at an echo time where fat and water signals are essentially

in-phase and the $UTE_2$ image is acquired at an echo time where fat and water signals are 180 degrees out-of-phase, these images can be used to refine the bone segmentation.

Finally, the CAR-RiDR method provides continuous-valued LACs for bone tissue but does not address the heterogeneity of soft tissue and adipose tissue LAC values. This is due to the fact that no relationship was found between the $R_2^*$ values of soft tissue and their corresponding CT-HU values. In the TESLA method, a relationship was derived for soft and adipose tissues using the longitudinal relaxation rate $R_1$. First, $R_1$ values were used to segment brain tissue into CSF, GM, and WM. Next, a spatially-matched binning approach was used to derive a relationship between $R_1$ and CT-HU inside each of these tissues as well as bone and adipose tissue. The results (Figures 6.9 - 6.11) showed that a linear relationship exists between $R_1$ and CT-HU values of CSF, GM, WM, and adipose tissue, while a logarithmic relationship exists between the $R_1$ and CT-HU values of bone tissue.

The TESLA segmentation method employs static thresholding of six intermediate images in order to arrive at classifications for bone, air, CSF, GM, WM, adipose tissue and general soft tissue. These thresholds were empirically selected to minimize misclassifications. Thresholding of MR images is not commonly used due to the sensitivity of voxel intensities to acquisition conditions, thereby making inter-subject comparison of intensities difficult. The TESLA method overcomes this limitation by basing its segmentation in part on normalized intermediate images. For air segmentation, $iUTE_3$ and $iUTE_{25}$ images were normalized to the 99th percentile value. For bone segmentation, normalization is achieved by virtue of $R_1$ being a physical parameter. While the intermediate images for fat and soft tissue were not normalized, good segmentations were still achieved with static thresholds. The advantage of

static thresholds is they remove the need for operator involvement in the segmentation process and automate the segmentation component of the TESLA method.

The parameters for the equations for the conversion from $R_1$ to CT-HU were computed from regression analysis on data from a population of subjects. Validation of this model, which was performed using a leave-one-out strategy, revealed little variation across subjects for the fit parameters of each tissue type. Thus, the conversion equation governing the relationship between $R_1$ and CT values can remain static across patients for each tissue type. These conversion parameters can be computed offline from an existing population of subjects, thereby automating the LAC assignment component of the TESLA method. When used in combination with the static thresholds from the segmentation component, static conversion parameters result in complete automation of the TESLA method.

The proposed TESLA method is a mapping-based MRAC method that combines the quickness and robustness of segmentation-based methods with the high accuracy exhibited by atlas-based methods. It differs from existing mapping-based methods by providing continuous-valued LACs for bone, CSF, GM, WM, and adipose tissue. The use of continuous-valued LACs for brain soft tissues made little difference in whole-brain error compared to using a single LAC value, but showed some differences in individual ROIs studied. Future work should examine these effects in detail.

The proposed TESLA method results in accurate PET reconstructions when evaluated against the gold standard CT-scaled method. Whole-brain (Figures 6.16 and 6.17) and regional analysis (Figure 6.18) of PET reconstruction errors demonstrates that the proposed method performs well across different brain regions and greatly outperforms the vUTE method in attenuation correction of the head. While differences in errors between PET reconstructions

using the TESLA method and the CAR-RiDR differences were not significant in the whole-brain (n = 28), the TESLA method significantly outperformed the CAR-RiDR method in 8 of 9 ROIs where a difference was observed. Furthermore, the TESLA method produces significantly lower differences between the $95^{th}$ and $5^{th}$ percentile error values in the whole-brain when compared to both the CAR-RiDR and vUTE methods.

There are a few limitations to our study that are worth elaborating on. First, the variable flip angle approach to compute $R_1$ is susceptible to $\textbf{B}_1$ inhomogeneity. As a reminder, the $\textbf{B}_1$ field refers to the RF pulse that is utilized in order to tip the magnetization into the transverse plane, While $\textbf{B}_0$ inhomogeneity refers to differences in the static magnetic field across the field-of-view, $\textbf{B}_1$ inhomogeneity refers to differences in the flip angle achieved at different locations. If the flip angle at any given location varies from what is expected, the computation of $R_1$ will be inaccurate in these regions. Recently, it has been demonstrated that this effect has a more severe impact short $T_2$ tissues, such as bone, than on tissues with longer $T_2$ times *(5)*. The solution proposed by that study involves estimating correction factors for the flip angle assumed at every voxel by utilizing a dual-TR UTE image acquisition. The $T_1$ can then be re-computed using the corrected flip angles *(5)*. Such a correction method can be incorporated into the TESLA method for more accurate quantitation of $R_1$, if necessary.

Second, the acquisition time required to acquire the necessary images increased from 1:40 min to 3:54 min due to the second flip angle acquisition. While this an increase in time by a factor of two, there are many strategies that can be explored to potentially reduce this acquisition time to under 2 min. These strategies include further lowering the TR and Kr parameters used in the sequence and utilizing a multi-shot acquisition similar to the vendor's approach.

Finally, some of the same limitations presented for the CAR-RiDR study in Chapter 5 apply to this study as well. Images used in this study were acquired mostly from normal subjects at one center using the same PET/MRI and PET/CT scanners. Further evaluation will be needed to determine if differences in the acquisition system or presence of disease states with focal lesions affect the results achieved with the proposed method. The data used in this study were primarily from older subjects (mean age: 75 years). Thus, further validation of the proposed method in more diverse populations is needed.

To our knowledge, the TESLA method is the first MR-based attenuation correction method to directly associate the MR relaxation rate $R_1$ with CT-HU, providing continuous-valued attenuation coefficients not just for bone tissue but for adipose and brain tissues as well. The proposed method has been shown to be highly accurate, producing $< 3\%$ error in whole-brain. Moreover, our method greatly decreases the spatial variations of PET errors compared to the vendor-provided UTE method as evidenced by the reduction in the difference between the $95^{th}$ and $5^{th}$ percentiles of the PET errors (Section 6.3.4).

## 6.5 Conclusions

In summary, this study presents an accurate MR-based attenuation correction method (TESLA) for use in quantitative PET/MRI neurological imaging. The TESLA method employs UTE images acquired at two flip angles to estimate LAC values for bone, CSF, GM, WM, and adipose tissue using a regression between $R_1$ and CT-HU. From our analysis, we conclude the proposed method closely approaches ($< 3\%$ whole-brain error) the gold standard CT-scaled method in PET reconstruction accuracy.

# REFERENCES

1. Juttukonda MR, Mersereau BG, Chen Y, et al. MR-based attenuation correction for PET/MRI neurological studies with continuous-valued attenuation coefficients for bone through a conversion from R2* to CT-hounsfield units. *Neuroimage*. 2015;112:160-168.

2. Nielles-Vallespin S, Speier P, Weale P, Shah S, Mueller E. 3D double echo TrueFISP and FLASH ultra-short echo time musculoskeletal imaging. *Proc Intl Soc Mag Reson Med.* 2009.

3. Cabello J, Lukas M, Forster S, Pyka T, Nekolla SG, Ziegler SI. MR-based attenuation correction using ultrashort-echo-time pulse sequences in dementia patients. *J Nucl Med*. 2015;56:423-429.

4. Andersen FL, Ladefoged CN, Beyer T, et al. Combined PET/MR imaging in neurology: MR-based attenuation correction implies a strong spatial bias when ignoring bone. *Neuroimage*. 2014;84:206-216.

5. Han M, Larson P, Krug R, Rieke V. Actual flip angle imaging to improve T1 measurement for short T2 tissues. Toronto, Canada: International Society for Magnetic Resonance in Medicine; 2015.

**CHAPTER 7: CLINICAL APPLICATIONS**

There are many clinical applications in neurology *(1)* and oncology *(2)* where simultaneous PET/MRI systems have garnered significant interest due to the possibility of using MRI to complement the information from PET. This complementary information comes in the form of anatomical MR images with excellent soft tissue and in the form of MR images where the source of contrast (diffusion, flow, etc.) is different from that in PET images. In this chapter, two such applications in epilepsy and prostate cancer will be discussed along with the relevance of the work presented in this dissertation to those applications.

**7.1 Epilepsy**

*7.1.1 Overview*

Epilepsy, a term which is derived from the ancient Greek for "to seize", is the name given to the collection of neurological disorders characterized by chronic epileptic seizures and has been documented since as far back as 2000 B.C. *(3)*. An epileptic seizure is defined as an episode of abnormally excessive neuronal activity in the gray matter of the brain *(4)*. The symptoms of a seizure episode can range from a temporary loss of awareness to the characteristic uncontrollable jerking motions seen in many patients. Epilepsy is the third most frequent neurological disorder in the United States with over two million Americans already affected and approximately 150,000 new cases each year *(5)*.

*7.1.2 Multi-drug Resistant Epilepsy*

The most unsettling statistic related to epilepsy is that one-third of patients present with a form of the disease that does not respond well to any currently available medication *(5)*, a

condition known as multi-drug resistant epilepsy. A lobectomy can performed if focal epileptogenic zone, the origin of the malevolent electrical activity, is known. Since the more brain tissue the patient retains the better, it is extremely beneficial for neurosurgeons to have a precise location of the epileptic focus so no more tissue is removed than absolutely necessary. To complicate matters, the surgery is not performed at all in cases where the seizure focus cannot be localized, leaving the patient to live with recurring seizures. Currently, a battery of tests including PET, SPECT, MRI, surface EEG, intra-cranial EEG and neuropsychology evaluations are conducted to try to pinpoint the seizure focus. Recently, the possibility of acquiring simultaneous functional information from PET and MRI as well as structural information from MRI has been suggested as a tool that neuro-radiologists could utilize when making the diagnosis. Thus, the identification of epileptic seizure foci is potentially an excellent application for simultaneous PET/MRI systems *(6)*.

*7.1.3 PET Localization of Seizure Foci*

During the inter-ictal phase, or the period between seizures, the affected region exhibits decreased glucose metabolism, or hypo-metabolism, compared to the unaffected contralateral hemisphere. Thus, [18-F] fluorodeoxyglucose (FDG) is an ideal PET radiotracer for use in epilepsy. [18-F] FDG is a glucose analog where a hydroxyl group is replaced with the fluorine-18 radioisotope. This tracer reflects all of the physiological characteristics of glucose when injected into the body, including uptake into cells, but cannot be metabolized by the cells, rendering [18-F] FDG an excellent tracer for examining which brain regions are demanding glucose. Since seizure foci exhibit decreased metabolism, neuro-radiologists look for regions of lower than expected signal intensities in PET images compared to the contralateral side. If the PET study is conducted during an ictal phase, i.e. during a seizure, the affected region is

expected to display an increase in glucose metabolism, or hyper-metabolism, due to the increased electrical activity of the neurons.

Many seizures occur without any observable symptoms in the patient, and an ictal event may go unnoticed by the operator. Without any additional knowledge, it is difficult to distinguish between hypo-metabolism in one hemisphere and hyper-metabolism in the contralateral hemisphere. Neuro-radiologists address this difficulty by normalizing their readings to the region of the brain known as the thalamus. When functioning normally, the thalamus is expected to uptake more glucose than the cortex. Thus, if the cortex in either hemisphere appears to take up as much as or more [18-F] FDG than the thalami, it can be classified as a case of hyper-metabolism in that hemisphere. If not, then the hemisphere with lower uptake of [18-F] FDG is said to be exhibiting a case of hypo-metabolism.

*7.1.4 MRI Localization of Seizure Foci*

Presently, anatomical MR images such as T1- and T2-weighted images are used to look for regions of atrophy, or tissue death, which is characteristic of the brain region containing the epileptic seizure focus. This approach works for some cases, but functional and microstructural changes often occur before changes in the macrostructure. Therefore, various functional and microstructural MRI approaches may be more beneficial in identifying seizure foci in regions where conventional MRI fails. One example of such an approach is diffusion MRI.

Diffusion-weighted imaging (DWI) measures the ability of protons to freely diffuse in tissue. The less structured the environment, such as seen in CSF, the higher the diffusion. The more structure present in tissue, such as seen in GM, the lower the diffusion. The tissue atrophy that occurs in the epileptic focus may result in a breakdown in the microstructure of GM that

restricts the diffusion of water protons. Thus, higher than normal diffusion in certain GM regions could be an indication of abnormality.

*7.1.5 PET/MRI Localization of Seizure Foci*

Since [18-F] FDG PET and diffusion MRI provide complementary information, both scans could be used to develop a quantitative approach for identifying seizure foci. Currently, studies are being conducted in-house to determine if a ratio of the apparent diffusion coefficient (ADC) which is a measure of diffusion to the standardized uptake value (SUV) of glucose could provide a good indication of seizure foci. ADC values can be computed using DWI, while SUV values of glucose can be computed from PET imaging using [18-F] FDG. Diffusion is expected to increase in the problematic regions while the metabolism is expected to decrease, making the ratio of ADC to SUV in these regions higher than normal. Preliminary studies have shown promise in identifying seizure foci using this approach (Figure 7.1).
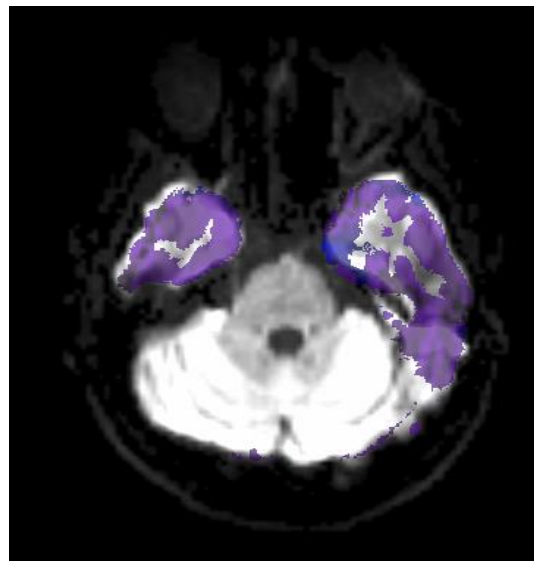


Figure 7.1: A sample ADC-PET ratio image overlaid on an anatomical image shows regions of high ADC-PET ratio (blue) in lobe where the seizure focus is present.

There are a few limitations to using this approach that must be addressed before it can be reliably used. First, the ratio of ADC to SUV would not be indicative of the seizure focus if the PET scan was acquired during an ictal event since the SUV value would be considerably higher during a seizure. Thus, ictal vs. inter-ictal PET scans need to be accurately determined and an adjustment must be made for ictal cases. Next, CSF regions normally display very high ADC values since diffusion is not restricted and display low SUV values since glucose uptake is normally low in CSF. Therefore, the ratio image of ADC to CSF would be contaminated with high intensities in CSF regions, making identifying abnormal regions in GM very difficult. This problem could potentially be solved by removing regions of CSF prior to computing the ratio image.

*7.1.6 Relevance of MR-based Attenuation Correction*

For the qualitative PET readings that contribute to the initial diagnosis of seizure focus location, PET images reconstructed using the vendor-provided Dixon-MRI method are being used. As mentioned in earlier in this chapter, this method results in large errors in the PET images, particularly in the cortical brain regions adjacent to the skull. Since these regions of GM are of utmost importance in epilepsy, these errors cannot be tolerated. Utilizing a method that provides more favorable error characteristics in these GM regions may increase the confidence of the radiologist reading the image or may help find regions that were completely missed in the vendor-reconstructed PET image.

*7.1.7 Pilot Study Examining Clinical Utility of TESLA Method*

To analyze the clinical utility of the MRAC method TESLA proposed in Chapter 6 versus the presently used vendor-provided Dixon-based method, a reader study was conducted using PET and MR data from five patients in an IRB-approved study at UNC Hospitals. [18-

F] FDG PET data were acquired for these patients on a simultaneous PET/MRI system. The proposed DUFA-UTE sequence outlined in Chapter 6 was used to acquire MR data according to the following parameters: echo times (TEs) = 0.07 ms/3.69 ms, repetition time (TR) = 9 ms, flip angles (FA) = 5°/25°, radial lines (Kr) = 13,000, acquisition time = 3 min 54 sec, and voxel size = $1.56 \times 1.56 \times 1.56$ mm$^3$. Two-point Dixon images were acquired using the vendor-provided Dixon-VIBE AC sequence with the following imaging parameters: TR/TE$_1$/TE$_2$ = 2300/1.23/2.46 ms, acquisition time = 18 sec, flip angle = 10°, and voxel size = $2.6 \times 2.6 \times 3.12$ mm$^3$. MR images were reconstructed on the scanner while raw PET data was transferred offline for image reconstruction.



Figure 7.2: A representative slice from a representative attenuation map derived using the TESLA method show that regions of bone and air are well identified.

The UTE images from the DUFA-UTE sequence were processed in a manner similar to the segmentation and attenuation map generation protocol outlined in Chapter 6. Regions of the attenuation maps where the DUFA-UTE images did not provide enough coverage were replaced with corresponding regions from the vendor-provided UTE map. The Dixon-based attenuation maps were used as provided by the PET/MRI scanner. A transverse slice from the attenuation map of a representative subject is shown in Figure 7.2. PET images were

reconstructed offline using each of the Dixon-based attenuation map and the TESLA-based attenuation map for all 5 patients using the vendor-provided PET image reconstruction platform (E7Tools, Siemens Healthcare, Knoxville, TN).

A board-certified Nuclear Medicine physician at UNC Hospitals performed a blind review on the reconstructed PET images using the Dixon and the proposed TESLA method. For each set of images of each patient, the physician was asked to identify possible abnormal PET regions and provide a diagnostic score on a 1-5 scale: 1: definitely negative; 2: probably negative; 3: equivocal; 4: probably positive; 5: definitely positive. In some cases, a PET image reconstructed using one method provided a result that was not observed in the PET image reconstructed using the other method. For example, if a region of strong hypo-metabolism was detected in the left temporal lobe in the PET image from the Dixon-based method, this reading would be assigned a diagnostic score of 5. If the corresponding region in the PET image from the TESLA method strongly disagrees with this read, the indication of hypo-metabolism in the left temporal lobe would be assigned a 1 for this method. If it moderately disagrees, this indication would be assigned a 2. If a judgment cannot be made, this indication would be assigned a 3. The radiological findings of the reader study for the five patients are summarized in Table 7.1 along with the clinical finding for the seizure focus identified using intracranial EEG.

Table 7.1: Results of PET reader study

| Patient | PET$_{Dixon}$ | PET$_{TESLA}$ | Seizure Focus |
|---------|---------------|---------------|---------------|
| 1 | Hypo: Left Hemisphere – 1 | Hypo: Left Hemisphere – 5 | Left Temporal |

| | | | |
|---|---|---|---|
| 2 | Hypo: Left Hemisphere – 1<br><br>Left Mesial-Temp – 2<br><br>Left Temp-Parietal – 2 | Hypo: Left Hemisphere – 5<br><br>Hypo: Left Mesial-Temp – 5<br><br>Hypo: Left Temp-Parietal – 5 | Left Temporal |
| 3 | Hypo: Right Mesial-Temp – 4<br><br>Hypo: Right Hemisphere – 1<br><br>Hyper: Left Temp – 1 | Hypo: Right Mesial-Temp – 5<br><br>Hypo: Right Hemisphere – 5<br><br>Hyper: Left Temp – 3 | Left Temporal |
| 4 | Hypo: Left Temporal – 5<br><br>Hypo: Left Parietal – 5<br><br>Hypo: Left Hemisphere – 5 | Hypo: Left Temporal – 5<br><br>Hypo: Left Parietal – 5<br><br>Hypo: Left Hemisphere – 3 | Left Temporal-Central |
| 5 | Hypo: Left Frontal – 4<br><br>Hypo: Right Parietal – 4<br><br>Hypo: Right Occipital – 4 | Hypo: Left Frontal – 3<br><br>Hypo: Right Parietal – 4<br><br>Hypo: Right Occipital – 4 | Right Temporal-Occipital |

As can be seen in Table 7.1, the region identified as containing the clinical seizure focus was able to be identified as a potential region of abnormality in all five patients with fairly high confidence using the PET images reconstructed using the TESLA method. Meanwhile, the PET images reconstructed using the Dixon method resulted in no visual abnormalities for two patients (patients 1 and 2). Furthermore, in one case (patient 3), a region of focal uptake corresponding to a hyper-metabolic lesion was clearly visible in PET$_{TESLA}$ reconstruction and was completely indiscernible in PET$_{Dixon}$ (Figure 7.3). These preliminary results demonstrate that the TESLA method for performing MRAC generally leads to different estimates of confidence when compared to the currently utilized Dixon-based method for identifying epileptic seizure foci.

Preliminary studies (Section 7.1.5) conducted using the quantitative ADC to SUV ratio utilized the vendor-provided PET images reconstructed using the Dixon method which are not very beneficial for qualitative applications much less for quantitative ones. Thus, it is expected that the confidence level of radiological diagnosis should improve if the PET images are reconstructed with a more accurate MRAC method such as the TESLA method. It remains to be determined whether this improvement in PET quantification accuracy is beneficial in computing the ADC to SUV ratio metric.
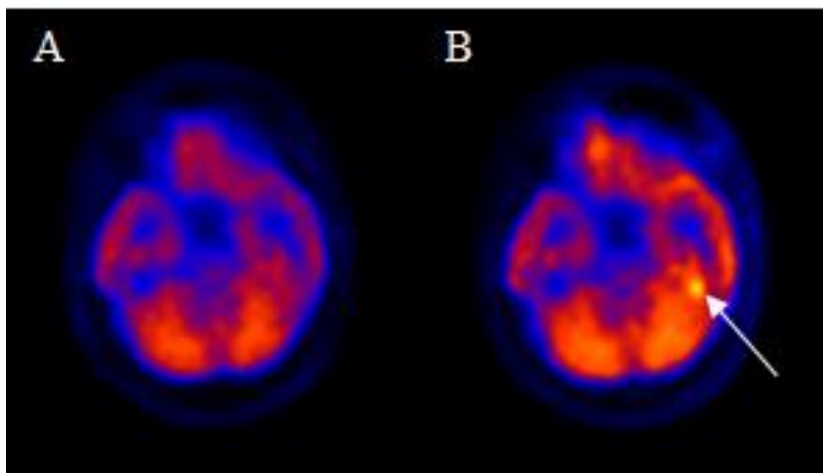


Figure 7.3: Sample slices from PET$_{Dixon}$ (A) and PET$_{TESLA}$ (B) reconstructions for one patient show the presence of a hyper-metabolic lesion in the PET$_{TESLA}$ image that is indiscernible in the PET$_{Dixon}$ image (arrow).

## 7.3 Prostate Cancer

### 7.3.1 Overview

Prostate cancer is the third most prevalent type of cancer in the United States trailing lung and breast cancers and just ahead of colorectal cancer *(7)*. MRI, specifically T2-weighted MR imaging, is currently considered the imaging standard for evaluating prostate cancer. Multi-parametric MRI with MR spectroscopy (MRS), DWI, and dynamic contrast-enhanced (DCE) MRI has recently gained some ground as a complement to structural T2-weighted imaging of the prostate. PET imaging using radiotracer analogs of choline derivatives has been used to detect the important biomarker for this disease – prostate specific antigen (PSA). The

use of PET in prostate cancer has been limited, however, in part due to difficulty distinguishing the peripheral zone from the transition zone of the tumor in CT. The high resolution imaging offered by MRI coupled with the excellent soft tissue contrast make hybrid PET/MRI an appealing modality for imaging prostate cancer *(8)*.

*7.3.1 Relevance of MR-based Attenuation Correction*

The anatomy in the region of interest in prostate cancer presents a unique challenge in PET due to the prominent presence of bone in the surrounding region. The hip bone and the pelvic bone are in position to attenuate a large percentage of photons emitted by annihilation events from the PET radiotracer molecules in the prostate. Currently, the Dixon-based approach is used for generated attenuation maps for body applications, including the pelvic region for prostate imaging. As previously mentioned, this approach is not very accurate because it ignores bone completely (Figure 7.4). Atlas-based methods, which are fairly accurate in the head, are not as successful in the body due to the increased complexity of the inter-subject nonlinear image registrations required. Therefore, a purely patient-specific MR-based approach, such as the one presented in this dissertation, is very desirable in body imaging.
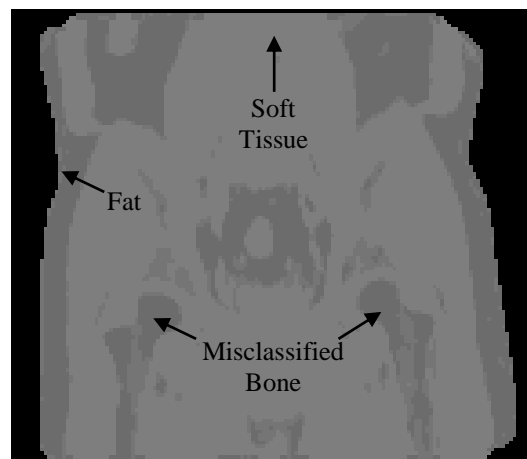


Figure 7.4: A Dixon-based attenuation map
derived for the pelvis region.

Proof-of-concept studies that have been conducted using the TESLA method in the pelvis region (Figure 7.5) show that the method is capable of identifying regions of bone, soft tissue, and fat in the pelvic region. Due to the many differences in anatomy between the head/neck region and the pelvic region, further studies are necessary in order to refine the segmentation method and to evaluate whether the relationship between R1 values and LAC values exists outside of the head. Furthermore, nonuniformity artifacts due to the much larger field-of-view in the abdomen compared to the head could hinder the utility of UTE imaging in the pelvis.
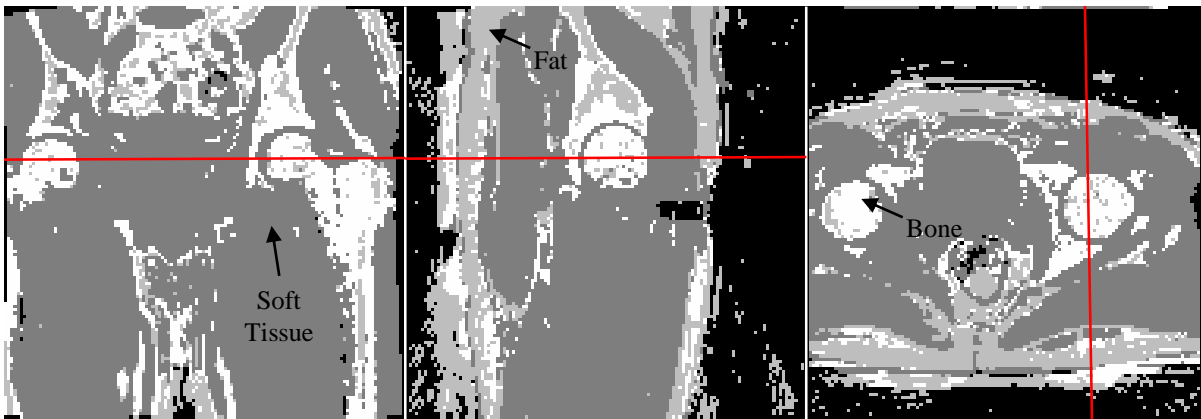


Figure 7.5: Slices in three orientations (left to right: coronal, sagittal, axial) from a TESLA-based segmentation derived for the pelvis region. The red lines indicate the position of the orthogonal slices.

# REFERENCES

1. Catana C, Drzezga A, Heiss WD, Rosen BR. PET/MRI for neurologic applications. *J Nucl Med*. 2012;53:1916-1925.

2. Yankeelov TE, Peterson TE, Abramson RG, et al. Simultaneous PET-MRI in oncology: A solution looking for a problem? *Magn Reson Imaging*. 2012;30:1342-1356.

3. Magiorkinis E, Sidiropoulou K, Diamantis A. Hallmarks in the history of epilepsy: Epilepsy in antiquity. *Epilepsy Behav*. 2010;17:103-108.

4. Fisher RS, van Emde Boas W, Blume W, et al. Epileptic seizures and epilepsy: Definitions proposed by the international league against epilepsy (ILAE) and the international bureau for epilepsy (IBE). *Epilepsia*. 2005;46:470-472.

5. Epilepsy Foundation. An introduction to epilepsy. . Available from: http://www.epilepsy.com/start-here/introduction-epilepsy. Accessed June 12, 2015.

6. Catana C, van der Kouwe A, Benner T, et al. Toward implementing an MRI-based PET attenuation-correction method for neurologic studies on the MR-PET brain prototype. *J Nucl Med*. 2010;51:1431-1438.

7. American Caner Society. About cancer. . Available from: www.cancer.gov. Accessed June 12, 2015.

8. de Perrot T, Rager O, Scheffler M, et al. Potential of hybrid (1)(8)F-fluorocholine PET/MRI for prostate cancer imaging. *Eur J Nucl Med Mol Imaging*. 2014;41:1744-1755.

# CHAPTER 8: SUMMARY AND CONCLUSION

## 8.1 Major Contributions

Simultaneous PET/MRI systems, while opening the door to novel clinical applications, are currently plagued by the lack of an accurate method to perform MRI-based correction for PET photon attenuation. Current methods provided by the vendor quickly produce the attenuation maps needed to perform the correction but result in PET images that contain average errors in whole-brain of much greater than 5% compared to the gold standard in neurological PET/MRI applications. There have been many attempts to develop an MRAC method that is both accurate and quick, but there seems to exist a trade-off between these two characteristics.

Atlas-based methods employ a population of paired MR and CT images in order to derive an attenuation map with continuous-valued LACs that produces reconstructions that are accurate (whole-brain error < 5%) compared to the gold standard. Consequently, the computation times required by the algorithms utilized by these methods are typically too high to be clinically feasible. Segmentation-based methods employ a classification of tissues before deriving the attenuation map by assigning one LAC value to each tissue. This class of methods, to which the vendor-provided methods belong, are generally quick but produce PET reconstructions that are not as accurate as the ones produced by atlas-based methods, partly due to their inability to address the heterogeneity of tissue LACs.

Recently, a new class of methods has emerged with the capacity to combine the rapidness of segmentation methods with the accuracy of atlas-based methods. These methods

are known as mapping-based methods because they produce patient-specific attenuation maps with continuous-valued attenuation maps by utilizing a conversion between MR signal intensities or relaxation parameters and PET LAC values. The methods presented in this dissertation are among the first of this class.

The CAR-RiDR method presented in Chapter 5 accurately segments patient images into bone, soft tissue, adipose tissue, and air and derives a relationship between MR relaxation rate $R_2^*$ and CT-Hounsfield units for bone tissue. This relationship is then used to produce attenuation maps with continuous-valued LACs for bone that produce accurate PET reconstructions when compared to the gold standard. This method was the first to establish a quantitative relationship between $R_2^*$ and CT-HU for bone tissue in order to produce pseudo-continuous attenuation maps without the need for an atlas. Furthermore, this method was rigorously tested on data from a larger group of subjects than any other method presented to date.

The TESLA method presented in Chapter 6 improves on its predecessor by optimizing and acquiring all necessary information using the UTE sequence. The relaxation rates $R_1$ and $R_2^*$ along with a two-point Dixon decomposition are computed UTE images from two flip angles. This MR data is then used to segment bone, air, gray matter, white matter, CSF, and adipose tissue. A relationship between $R_1$ and CT-HU is utilized to provide continuous-valued LACs for brain and adipose tissue in addition to bone. This method is the first to establish a quantitative relationship between R1 and CT-HU for these tissues in order to produce attenuation maps for neurological applications that are mostly continuous without the need for information from an atlas.

**8.2 Clinical Implications**

As mentioned in Chapter 1, the advent of simultaneous PET/MRI systems has garnered significant interest in many clinical fields, including neurology *(1)* and oncology *(2)*. Chapter 7 elaborates on two pathologies where PET/MRI systems could be of tremendous use to clinicians. These applications in epilepsy and prostate cancer require accurate quantitation in PET data that the vendor-provided methods currently used cannot provide. The potential of the TESLA method developed in this work to improve clinical reads of neurological PET images has been demonstrated. Proof-of-concept studies in the pelvic region show that the TESLA method may be able to provide attenuation maps of similar quality for PET/MRI studies of prostate cancer as well.

**8.3 Future Work**

8.3.1 Sequence and Processing

The DUFA-UTE sequence used to acquire the TESLA method requires two back-to-back acquisitions in order to collect MR data at two flip angles. While the changing of one parameter between acquisitions is trivial, it would be more straightforward to design the sequence to acquire both measurements in one acquisition. Currently, the computation of the attenuation map is performed offline after the acquired images are transferred from the scanner. To render the TESLA method useful in the clinic, the processing protocol must be programmed into the vendor's image reconstruction platform. The successful achievement of both of these goals would allow for the acquisition of the images and the generation of attenuation maps with the click of a button in under 4 min. This acquisition time could be further reduced by exploring avenues such as a multi-shot acquisition, where multiple lines of k-space are

acquired within a single repetition, or an even greater reduction of the repetition time and the number of k-space lines collected.

8.3.3 Evaluation

The evaluation of the methods presented in dissertation focused primarily on normal subjects in an Alzheimer's dementia study and. While a decreased performance in the presence of pathology is not expected, it would be beneficial to quantitatively evaluate the TESLA method in other neurological conditions, such as brain tumors, where the anatomy in the patient's head is modified. Further work is also warranted in applying the proposed method in regions outside of the head and neck. Preliminary studies have shown that the TESLA segmentation may work well in the pelvic region, but more studies are required to determine if the proposed method will be valuable in PET/MRI studies of this region.

**8.4 Conclusion**

In conclusion, the work presented in this dissertation has resulted in the production of an MRI-based attenuation correction method for use in PET/MRI that is accurate when compared to the gold standard, enables the quick acquisition and processing of MR images to form attenuation maps, and contains a fully automated processing pipeline. The accuracy of the method is due to both the optimized UTE sequence utilized as well as a novel processing pipeline that contains an accurate segmentation of tissues of interest and an assignment of continuous-valued attenuation coefficients for most tissues in the head and neck. The use of this method would enable accurate quantification of PET data for use in any neurological application of simultaneous PET/MRI systems.

# REFERENCES

1. Catana C, Drzezga A, Heiss WD, Rosen BR. PET/MRI for neurologic applications. *J Nucl Med*. 2012;53:1916-1925.

2. Yankeelov TE, Peterson TE, Abramson RG, et al. Simultaneous PET-MRI in oncology: A solution looking for a problem? *Magn Reson Imaging*. 2012;30:1342-1356.